Age, origin and vertical deformation of a previously interpreted regional erosion surface: a multi-disciplinary analysis of the Wellington K Surface

Campbell David Sanders Watson

A thesis submitted to Victoria University of Wellington

In partial fulfilment of requirements for the degree of

Master of Science in Geology

School of Geography, Environment, and Earth Sciences

Thesis Advisors: Prof T.A. Stern and Dr K.P. Norton

May 2016

This thesis is dedicated in loving memory to my Grandma Iris

Abstract

Measuring and describing horizontal motion in plate boundary zones is relatively straightforward. Vertical movements are, on the other hand, more difficult to measure but they are important as they provide key insights to crustal and upper mantle dynamics.

This thesis is directed towards learning about the vertical movements of a previously interpreted regional erosion surface, termed the K Surface. Sir Charles Cotton (1912) was the first to draw attention to this physiographic feature that dominates the landscape of the western Wellington region from Makara in the south to Paraparaumu in the north. Little information is known about the age, origin and uplift history of this feature, due to a lack of overlying Neogene sediments in the region. A multidisciplinary approach is applied here, using a combination of geological, geophysical and topographic methods to document the age, origin and uplift history of the K Surface in a local and regional context.

A depth profile of cosmogenic ^{10}Be exposure ages from a 300 m high K Surface remnant suggest that the K Surface was last exposed $238.1^{+149.3}_{-141.7}$ ka (2σ), which correlates with marine isotope stage (MIS) 7. Erosion rates are $1.79\ ^{+0.59}_{-0.83}$ cm ka $^{-1}$, indicative of ~4 m of total erosion since exposure.

On a regional scale, timing, magnitude, and wavelength of K Surface uplift is consistent with a similar regional uplift in the Wairarapa, while at the same time subsidence is seen offshore, southwest and northwest of Wellington. This coeval uplift and subsidence on a ~ 70 – 80 km spatial scale is explicable within the context of a simple plate flexure model with a free edge. The flexure is proposed to have been enhanced in the last ~ 0.3 my when the freely subducting Pacific plate interacts with a barrier that produces a consequent bending moment, on the end of the plate. This barrier is proposed to be mantle lithosphere of the overriding Australian plate that rapidly thickened during the Pliocene. Combining the Isotopic and geologic evidence with geophysical modelling, suggests that the “K Surface” is not a singular regional erosion surface, as previously suggested (e.g. Cotton, 1953; Ota et al., 1981). Rather it is composed of time transgressive marine platforms differentially formed and uplifted by both flexure of the underlying Pacific Plate and smaller scale crustal fault movements.

Acknowledgements

Completing this thesis has really hit home to me how collaborative the geoscience field is. Hence, I have many people to acknowledge!

First, greatest thanks goes equally to my two advisors, Tim Stern and Kevin Norton. You have been great supervisors and I have enjoyed working with both of you. It is hard to believe this project all started with looking at sands on top of a hill!

Cheers to Euan G.C. Smith, for living up to his middle initials, and just being a general legend when it came to tedious discussion regarding terrain corrections any many other geophysical and geological issues.

Thanks to Adrian, Dez, Steve, Dom, Rachel, Aasha, Jurgen, Ben Hines, Simon Lamb and Ham for help with fieldwork. Thanks to Huw Horgan for help with my favourite program, GlobeClaritas. Thank you to John Simes of GNS and Tom Ayling for assistance with taking core plugs. Thanks to Murray Helm of CoreLabs for taking the helium porosity measurements. Thanks Stuart Bush for making my thin sections. Thank you Albert Zondervan for measuring my cosmo samples. Thanks also goes to Warren for help with using the point counter.

Thanks to Gavin Bruce and other farmers for letting me access your land. Thanks also to the locals of Makara Village for the use of your land for geophysical surveys.

Huge appreciation goes to the technical staff: Adrian Benson (fieldwork and data processing), Andy Rae (ArcGIS), Jane Chewings (lab procedures and general advice), Dez (fieldwork) and Sabrina Lange (sample preparation). Not much would have been possible without your help.

Thanks to Brent Alloway and Tim Little for providing me with opportunities to tutor field trips throughout my post-graduate study; they helped to reduce the financial burden and were also great fun!

Thank you to all the great friends I've made throughout my five and a bit years studying geology at Vic (apologies if I've forgotten your name, try harder next time): Sam, Chris, Viking (great COD nights), Dez, Matt, Condor, Naaaach, Tom Ayling, Steve Keys, Tom Wilson, Gabe, Anya, Olya, Bryn, Ben Higgs, Hammer Hines, Jurgen, Marcel, Jesse Kearse, Merijn, Julia, Juliet, Rich, Shaun, Jenni, Harry, Ian, Hamish, Johnny, Shane, Nisha, Libby, Rackley, Aidan, Dom, Rachel, Geophysics Sam, Konrad and Andy.

Thanks to my mum, dad, and two (inferior) brothers, Ham and Lachie; thanks for the perfect balance of love and verbal abuse. Finally, thanks to my girlfriend Amanda, for the constant love and support, you're a keeper.

Table of Contents

List of Figures

List of Tables

1 Introduction

1.1 Project motivation and objectives

The New Zealand subcontinent straddles the boundary of the Pacific and Australian tectonic plates (Figure 1.1). The oblique convergence of these two tectonic plates has given rise to opposite senses of subduction along their boundary (Sutherland et al., 2000). Oceanic lithosphere of the Pacific Plate subducts westward underneath continental lithosphere of the Australian Plate within the Hikurangi Margin, east of North Island. The relative plate convergence rate along the Hikurangi Margin decreases from 50 mm yr^{-1} to 42 mm yr^{-1} and displays a greater margin parallel component southward along the plate boundary (Figure 1.1) (Beavan et al., 2002; Nicol et al., 2007; Wallace et al., 2004). South of New Zealand, the Australian Plate subducts eastward underneath the Pacific plate along the Puysegur Trench and under the southwestern tip of South Island at an average convergence rate of 38 mm yr^{-1} (Beavan et al., 2002). Between the subduction zones to the north and south lies the ~600 km long Alpine Fault. The Alpine Fault spans almost the entire length of South Island, and represents a transpressive collision zone, which has resulted in dextral and reverse slip sense along its boundary.

The Alpine Fault accommodates approximately 70 % of current plate motion (Sutherland et al., 2000; Walcott, 1998). The northern end of South Island is characterised by the Marlborough Fault System (MFS), which represents the ~200 km long transition from transpressive collision along the Alpine Fault to oblique subduction at the Hikurangi Margin (Figure 1.4) (Wilson et al., 2004).

It is important to understand the mechanisms by which plate motion is accommodated, both vertically and horizontally at subduction zones, as it has implications for our comprehension of the dynamics of lithospheric deformation, seismic hazard and subduction zone processes. Vertical movements are especially difficult to document, but are extremely useful as they can provide insights into crustal and upper mantle dynamics.

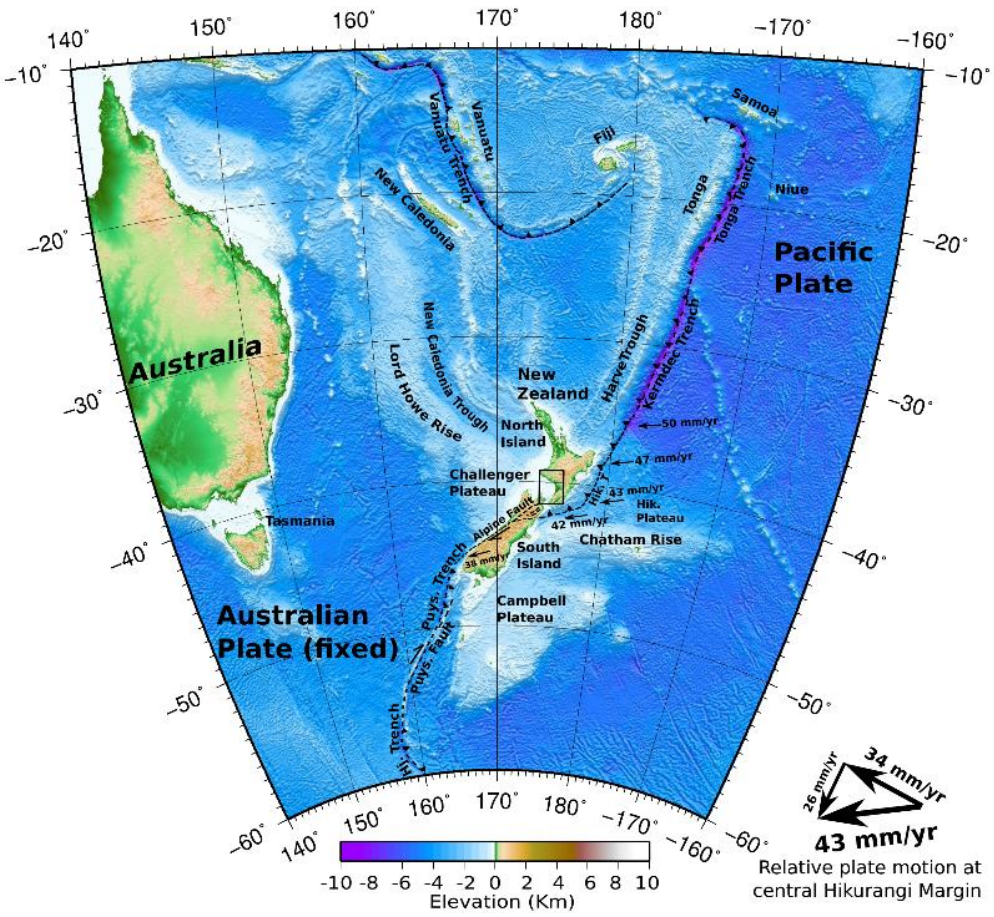

Figure 1.1 Regional elevation map of New Zealand and surrounding areas. To the west of New Zealand is the Australian Plate and to the east the Pacific plate. Black vectors indicate plate motion and are from (Beavan et al., 2002). (Tozer, 2013)

The Wellington area is located on the hanging wall of the southern part of the Hikurangi Margin, North Island, New Zealand. This hanging wall represents the overlying Australian Plate and the accretionary prism of the Hikurangi Margin subduction system.

The accretionary prism contains major fault structures. At Wellington, the subduction interface is shallowly dipping to the northwest at a depth of 25 – 30 km below the surface and the underlying oceanic crust (part of the Hikurangi Plateau) is approximately 12 – 13 km thick and 135 ± 15 million years old (Henrys et al., 2013; Tozer, 2013).

The Wellington region is dominated by Mesozoic Torlesse Complex basement rock of the Rakaia Terrane that is characterised by complexly folded, alternating beds of fine-medium grained greywacke and argillite (Kamp, 2000; Mortimer, 1994). Although the rocks are deformed, they generally strike NNE (Ota et al., 1981). Adjacent to Wellington, in the

Wairarapa Region, the Torlesse terrain changes from the Rakaia Terrane to the younger Pahau and Waioeka Terranes (Bradshaw et al., 1981; Mortimer, 1994). Major active dextral strike-slip faults cut through both regions sub-parallel to terrane boundary trends (Nicol et al., 2007). Because of this basement dominance and fault strike/terrane trend relationship, there is a lack of marker beds which therefore hampers the ability to quantify finite motions.

The uplift and exhumation of the Tararua and Rimutaka Ranges are, at least partially, due to continuous sediment underplating at the base of the Australian Plate since ~5 Ma (Henrys et al., 2013; Houseman and Molnar, 1997). Based on offsets measured on surface faults, Nicol et al. (2007) estimated > 12 km of upper plate shortening in the Wairarapa during the Miocene and Plio-Pleistocene epochs respectively. These shortening rates have increased over the past ~100 ka (Lamb and Vella, 1987). The western Wellington area however, remains potentially enigmatic. Some western Wellington uplift can be attributed to upper plate shortening by the active dextral strike-slip faults that cut through the region. These faults have horizontal slip rates ranging 1 – 10 mm yr^{-1} (e.g. Heron, 1998; Langridge et al., 2005). Vertical slip rates are approximately one tenth of horizontal slip rates, sometimes less.

In the western Wellington area, the top surfaces of many of the hills are flat and sometimes slightly dipping; this is in stark contrast to the steep, narrow gullies and sharp ridges that characterise the terrain of the Rimutaka and Aorangi ranges to the east and the Tararua Range to the north (Begg and Johnston, 2000). The flat tops have previously been interpreted to be remnants of a former extensive erosional surface, termed the K Surface, due to it being “key” to the original form of the landscape (Cotton, 1912b). This physiographic feature was first described by Sir Charles Cotton (Cotton, 1912b), and dominates the western Wellington area from Makara in the south, to Paraparaumu in the north. This surface has subsequently been gently tilted, truncated and displaced by tectonic processes. The K Surface remnants we can see in Wellington today therefore, vary in altitude. For example, Mount Kaukau has an altitude of 442 m whereas other areas are as low as 200 m such as Emerald Hill and Trentham Memorial Park (Begg et al., 2008; Cotton, 1957). Some K Surface remnants have their long axes trending NE (Ota et al., 1981). Ota et

al. (1981) suggests that the K Surface is folded with a northward trending axis; Grant-Taylor (1967) proposed the same sense of folding for areas east of the Wellington Fault. Ota et al. (1981) further postulates an E-W shortening direction, and attributes the NE trending K Surface remnants to Quaternary movements on the NE striking faults that cut through the area.

In 1912 (Cotton, 1912b), Cotton postulated the K Surface was a peneplain, formed via the third and final stage of William Morris Davis' geomorphic cycle of landform evolution, or "Davisian Cycle" (now largely superseded) (Chorley et al., 1973). Davis' idea was that, over the course of geological time, fluvial erosion would lower the land until there was such a small gradient that no erosion could occur (Chorley et al., 1973). In a later paper, Cotton (1957) attributed K Surface height differences to later deformation in between the NNE trending faults. Today, the peneplain concept is not without debate, due to an absence of present-day examples, and controversy over relict examples (Grapes, 2008). In his 1957 paper, Cotton revisited the K Surface, stating:

"Whether the surface was produced originally by peneplanation (downwearing of the land), by pediplanation (backwearing of scarps), or even by some other process such as marine erosion scarcely matters for the present purpose, which is to make use of it as a key … to the original tectonic form of the landscape" (Cotton, 1957, p. 776)

The characteristic flatness of the surface, in conjunction with the abundant marine platforms around Wellington as well as documentation of possible cliff lines suggest that K Surface formation may have been due to marine erosion (Grant-Taylor, 1965; Ota et al., 1981).

However, the age of the K Surface is poorly constrained because the Wellington area is dominated by Mesozoic basement (i.e. there are no dateable marker beds). A relatively young age (0.4 – 4 Ma) is suggested due to its overall good preservation (Ota et al., 1981), evidence for local subsidence preceding uplift during the Pliocene (Grant-Taylor and Hornibrook, 1964), and the local presence of the c. 0.4 – 1.2 Ma "Kaitoke Gravel" cover (Te Punga, 1984a, Begg and Mazengarb, 1996).

Nevertheless, the important question relating to K Surface age is whether it formed; (1) during the uplift events following the deposition of Pliocene marine sediments, today preserved in a marine outlier near Makara, or (2) during the uplift events of the Late Miocene. A significant aspect to note is that if the K Surface was initiated in the Late Miocene (or earlier), then it probably would have been further eroded and altered during Pliocene – Pleistocene uplift.

From the information above, we can see that there is a knowledge gap regarding a definite origin, age, and uplift mechanism(s) for the Wellington K Surface. Hence, due to the nature of this problem (geological and geophysical), satisfying these knowledge gaps requires a multi-disciplinary approach. Moreover, unlike previous authors (e.g. Cotton, 1912a, 1953; Cotton, 1912b; Cotton, 1957; Ota et al., 1981; Stevens et al., 1974), we now have the ability to view K Surface uplift in a regional context. When we do this, we see that since the Pliocene, the area to the west and the northwest of the K Surface (i.e. Whanganui Basin, through to the Marlborough Sounds) has been undergoing subsidence (Anderton, 1981; Hayward et al., 2010; Stern et al., 1992), whereas the Wairarapa plains to the east have been uplifting (Ghani, 1978; Lamb and Vella, 1987). A solution for the origin of the K Surface should therefore consider these differential vertical movements.

The key goal of this thesis is the collection of new data that documents the extent, shape, and timing of uplift for the K Surface in order to better understand the evolution of deformation in the capital region. We also test a geodynamic model to explain the K Surface uplift.

1.2 Background

This section provides background information on the study area for this thesis in terms of tectonics and geology, at both a local and regional scale.

1.2.1 New Zealand plate boundary history

Figure 1.2 explains the key phases in the tectonic evolution of the New Zealand sub-continent over the past 40 Ma. The Australian-Pacific plate boundary initiated at ~43 Ma represented by commencement of sea floor spreading in the Emerald Basin (south of

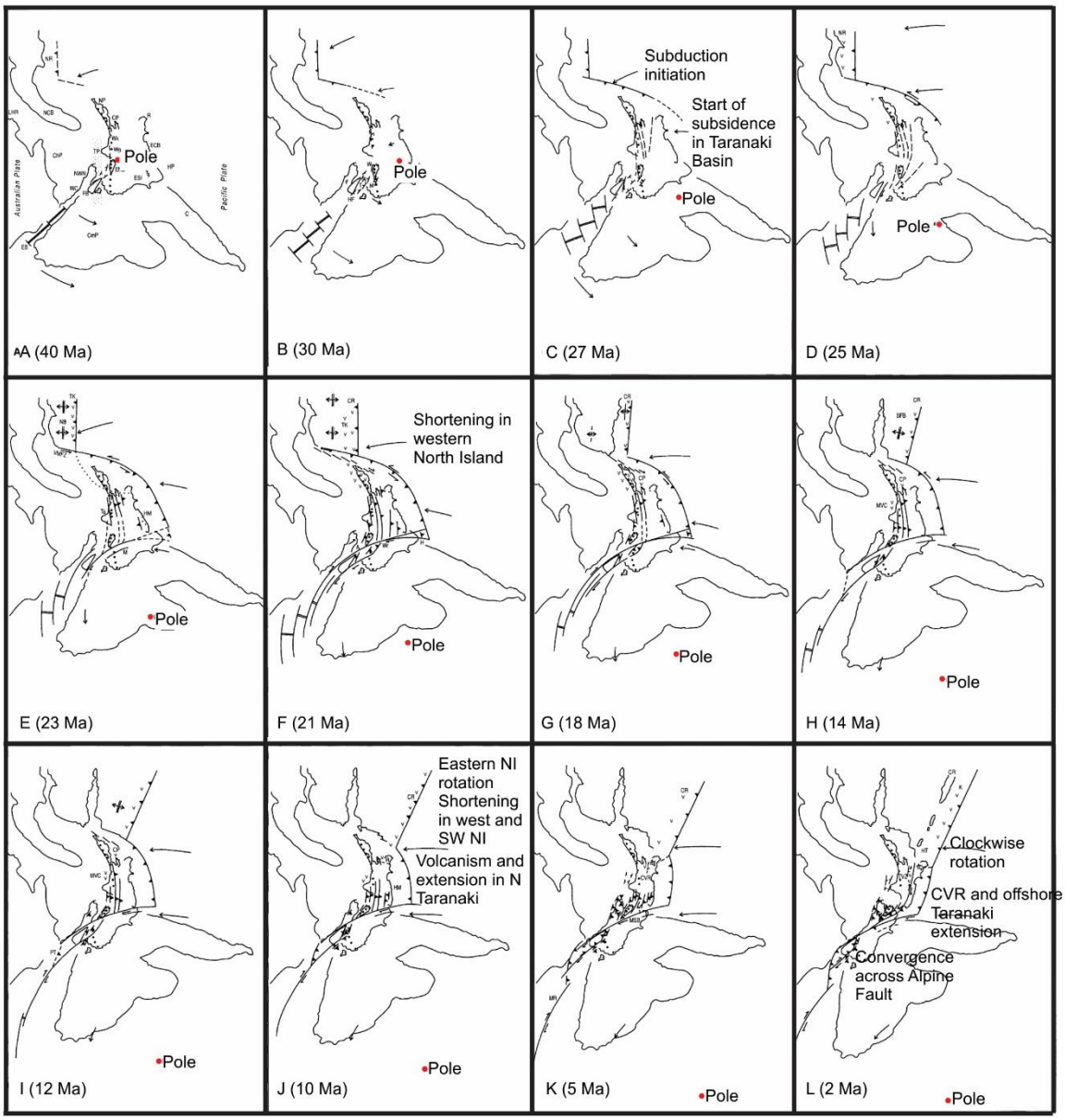

Figure 1.2 Schematic diagram depicting tectonic plate reconstructions of the Pacific – Australian Plate boundary zone over the past ~40 Myr as discussed in text. Figure adapted from King (2000), Stern et al. (2006).

present day South Island), and the occurrence of subduction north of New Zealand near Norfolk Ridge (Cande and Stock, 2004; King, 2000; Sutherland, 1995; Weissel et al., 1977). Structural and stratigraphic data suggest that Hikurangi Margin subduction began at a westward trend from the south of the margin between 25 and 20 Ma, as evidenced by the development of folding and thrusting, thus altering the style of sedimentation off the east coast of North Island during this time (Lamb, 2011; Lamb and Bibby, 1989; Rait et al., 1991). This coincided with a change in relative plate motion from transcurrent to obliquely convergent represented by southward movement of the Australian/Pacific finite pole over

this same time period (King, 2000; Smith, 1981; Stock and Molnar, 1982). By approximately 21 – 20 Ma, the majority of the key elements comprising the modern plate boundary zone had been established (King, 2000). The time amid initiation of the Hikurangi Margin and its present day location requires 70 – 90 ° of clockwise rotation of the margin as shown from finite plate reconstructions using paleomagnetic data (Lamb, 2011). This suggests an average clockwise rotation rate of 4 – 4.5 ° Myr^{-1} over the past ~20 Ma (Lamb, 2011). Rates of exhumation increase south-westward along the strike of the Axial Ranges, which agrees with these inferred clockwise vertical axis rotations (Jiao, 2015). As a consequence of these rotations, the southern part of the Hikurangi Margin has been rotated from a westward trend north of North Island to the present day north-east trend, proximal to Kaikoura (Lamb, 2011; Lamb and Bibby, 1989; Stern et al., 2006; Tozer, 2013). Results from finite pole rotations (Schellart et al., 2006) and 3D seismic imaging of the subducting slab (Reyners et al., 2011), suggest that the western part of the Hikurangi Plateau began subducting at approximately 10 Ma (Reyners, 2013). The Hikurangi margin's southward propagation may have been stopped by the Chatham Rise crustal block (King, 2000).

Pliocene – Pleistocene time saw the opening of the Havre Trough via 80 – 100 km of back-arc extension (Stern, 1985; Wright, 1993; Wright, 1994). This back-arc spreading ceases onshore near the Central Volcanic Region (CVR) and gives way to the North Island Dextral Fault Belt (NIDFB), a large system of dextral strike-slip faults (Beanland, 1995; Lamb, 2011; Stern, 1985). Stern (1985) found that the CVR is a zone of crustal thinning and extremely high effective heat flow (700 mW m^{-2}), twelve times higher than that of regular continental crust and thus proposed that the CVR represents a zone of active back-arc spreading within continental lithosphere. In central North Island, near Mt Ruapehu, the TVZ ends abruptly, and transitions into the Whanganui Basin. This represents a change from back-arc extension to compression, or a reversal from "Mariana" style subduction to "Chilean" style subduction (Nicol et al., 2007; Stern et al., 2006; Walcott, 1987).

1.2.2 Regional tectonics and uplift mechanisms of central and southern North Island

Analysis of porosity measurements in mudstone suggest that there has been approximately 2.5 km of rock uplift with a wavelength of ~400 km in the central North Island since 5 Ma (Figure 1.3) (Pulford and Stern, 2004), even though the area is thought of as a zone of back-arc extension (Stern, 1985; Wright, 1993; Wright, 1994). The timing of this uplift is peculiar, considering it predates the formation of the TVZ by approximately 3 Myr; an important observation considering that uplift in back-arc settings generally follows volcanism initiation (Stern et al., 2010; Tozer, 2013). Indeed, using seismic attenuation and *Pn* velocities, Pulford and Stern (2004) proposed a thermal anomaly in the upper mantle as the mechanism for rock uplift.

In Whanganui Basin, there has been approximately 4 km of subsidence since ~4 Ma even though it was subjected to mild thrusting and shortening during that time (Hunt, 1980; Lamarche et al., 2005; Proust et al., 2005). Stern et al. (1992) provide an explanation to this paradox by suggesting, through three dimensional flexural modelling, that the Whanganui Basin formed due to a "slab pull" force generated by frictional shear at the subduction interface.

Hayward et al. (2010) inferred a Holocene subsidence rate of 0.7 – 0.8 m ka^{-1} for the Marlborough Sounds using evidence from sediment cores. Interestingly, this subsidence rate is consistent with the average subsidence rate for the adjacent Whanganui Basin over the last 5 Ma (Hayward et al., 2010). Based on inferred timing for the onset of subsidence in the Marlborough Sounds (Craw and Waters, 2007), the gradual nature of subsidence (i.e. it did not occur in large, episodic steps, as would be expected in major earthquakes), Hayward et al. (2010) postulated that subsidence has migrated south from the Whanganui Basin to encroach on the Marlborough Sounds over the last 100 – 200 ka (Hayward et al., 2010).

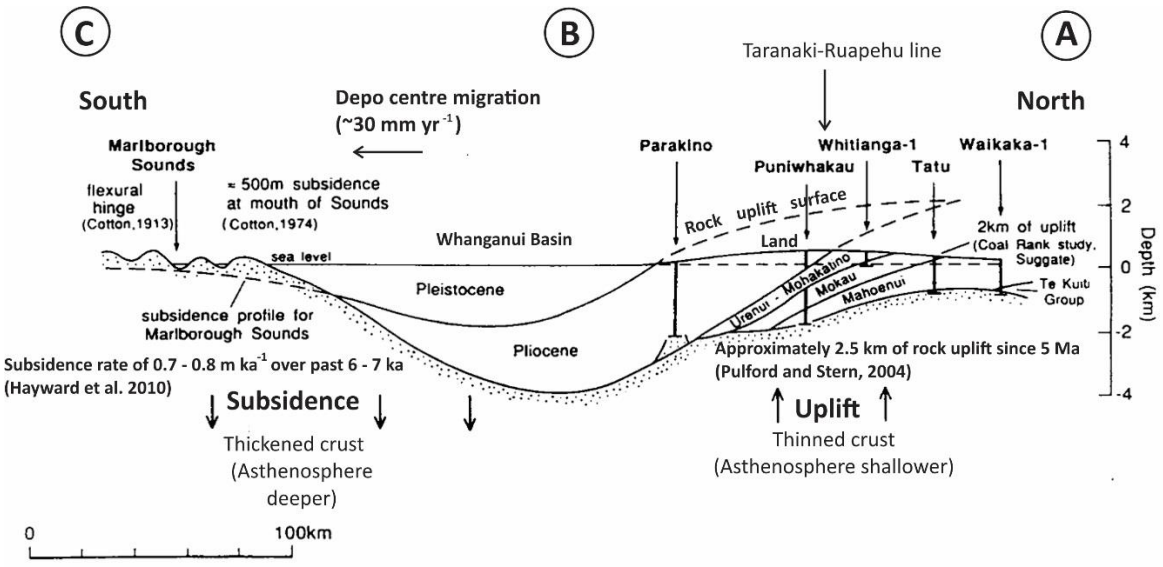

Figure 1.3 Schematic cross-section through the North Island and the upper most South Island of New Zealand illustrating vertical movement variations related to the instability of a lithospheric step (today, defined by the Taranaki-Ruapehu line (TRL)), based on Stern et al. (2013). The crust north of the TRL is thinned and uplifting, whereas south of the TRL, crust is thickened and subsiding. Letters A, B and C pertain to the cross-section location (Figure 1.4). Figure adapted from (Stern et al., 1992)

These contrasting vertical movements of North Island are recorded in the sediments throughout time and represent the southward migration of subsidence (basin depocentres) over time (Figure 1.4) (Stern et al., 1992; Anderton, 1981). Indeed, western North Island has been described as a "geological standing wave", which is characterised at the southern end of the cross-section (Figure 1.3) by the drowned topography of the Marlborough Sounds (Stern et al., 1992; Stern et al., 2006). This standing wave has a wavelength of ~250 km, an amplitude of ~± 1 km, and is thought to be migrating south at 30 mm yr^{-1} (Stern et al., 2013).

Using numerical experiments, Stern et al. (2013) investigated these vertical movements, and attributed them to progressive removal of mantle lithosphere, driven by a gravitational instability. This gravitational instability is inferred to have formed on the north-east margin of western North Island by the Late Miocene due to lithospheric structures of different thicknesses being juxtaposed (King, 2000; Stern et al., 2013). This juxtaposition formed a lithospheric step that has since migrated south-east to its current location at the geophysically defined Taranaki-Ruapehu line (Figure 1.3 Figure 1.4) (Salmon et al., 2011; Stern et al., 2013; Stern et al., 2006). As mantle lithosphere is removed, it results in the progressive thickening, then thinning of the overlying crust, thus explaining a mechanism

for the "geological standing wave", and its southward migration. It is important to note that Wellington uplift must be driven by a different mechanism as it is adjacent to the subsidence/crustal thickening zone of the lithospheric step instability.

To the east, the Wairarapa region has been progressively uplifting since the Middle Pliocene (Lee et al., 2002). Based on correlation between marine bench heights, Ghani (1978) documented growing synclines and anticlines on the Wairarapa coast and postulated low rates of uplift from 1.3 – 0.2 Ma and high rates of uplift from 0.2 Ma – present day. Using geological, geodetic and simple geometric modelling methods, Lamb and Vella (1987) inferred initiation of thrust faulting on the Huangarua Fault (Figure 1.7) in the Wairarapa at 1 Ma, and describe a regional uplift rate of approximately 1.5 mm yr^{-1} since 200 ka (i.e. 300 m net uplift). Due to lack of evidence for large fault offset, and a negative correlation between uplift pattern and inferred geodetic and crustal shortening rates, Lamb and Vella (1987) ascribe this late uplift to the back-tilting of large semi-rigid blocks sitting on a flexurally strong subducted slab. Miocene – Pleistocene sedimentary basins in the region have maximum gravity modelled depths of 2.2, 1.2, and 2.7 km adjacent to the Wairarapa, Martinborough, and Huangarua Faults, respectively (Hicks and Woodward, 1978; Tozer, 2013).

Kamp (2000) obtained and modelled zircon and fission track data via a transect through the Torlesse complex in the Wellington area of southern North Island from Cape Terawhiti to Cape Palliser. Kamp (2000) determined that > 4 km of exhumation occurred in the Wellington area during the Late Miocene (Figure 1.7B).

Walcott (1987) proposed that plate convergence at the Hikurangi Margin over the last 5 Ma has caused underplating of sediments which has then subsequently driven uplift of the Tararua and Rimutaka Ranges. Henrys et al. (2013) confirmed this idea by recognising low velocity zones at the plate interface. Occurrence of 4 km exhumation in the Tararua and Rimutaka Ranges over the same time period is identified by Jiao et al. (2015), which supports Henrys et al. (2013)'s above statement. However, Jiao et al. (2015) suggest that total rock uplift in the Tararua and Rimutaka Ranges may only partially be a result of sediment underplating, due to the large amounts of exhumation recorded.

Nicol et al. (2007) infers margin-normal shortening due to reverse faulting and folding in the upper plate during the development of the Hikurangi Margin, where the shortening rate has increased towards the south in southern North Island since the Late Oligocene. The Wellington/Wairarapa region exhibits the highest shortening rates 3 – 8 mm yr^{-1}. Results from fission track analysis by Jiao et al. (2015) correlate with this, estimating that basement exhumation rates of the Axial Ranges (parallel to the Hikurangi Margin) have increased south-westward since the Late Oligocene (Figure 1.5). According to Jiao et al. (2015), the largest amount of exhumation since the Oligocene occurred in southern North Island, at a similar latitude where the highest magnitude of crustal shortening (via thrusting) has been noted in fore-arc basins (Nicol et al., 2007). These high values of shortening and exhumation are interpreted to be due to the locking of plate convergence next to the area where the Chatham Rise collides with the Australian Plate (Jiao et al., 2015). The information above leads Jiao et al. (2015) to propose that the crustal shortening within the fore-arc of the Hikurangi Margin (e.g. Lamb and Vella, 1987; Nicol et al., 2007) is a main driver in regional uplift in eastern North Island (Figure 1.5).

An important question to note is, where does Wellington fit in here? Shortening is unable to be calculated due to a lack of Neogene sediments (i.e. marker beds) as the region is dominated by basement. Strong plate coupling underneath Wellington (Henrys et al., 2013) and a southward increasing shortening rate (Nicol et al., 2007) would suggest Wellington would be subject to high shortening also. However, the morphology of the hills in the Rimutaka, Tararua and Aorangi Ranges are different compared to Wellington. A possible explanation is that the shortening gets concentrated into a few faults, which pass under these mountainous zones (e.g. Wairarapa Fault).

1.2.3 Structure of the southern Hikurangi Margin

Most of Hikurangi Margin parallel plate accommodation is taken up by dextral strike-slip along the NIDFB (Beanland, 1995; Nicol et al., 2007; Van Dissen and Berryman, 1996; Wallace et al., 2004) and by clockwise vertical axis rotations (Lamb, 2011; Nicol et al., 2007; Walcott, 1984b). Convergent plate motion on the other hand, predominantly occurs (> 80

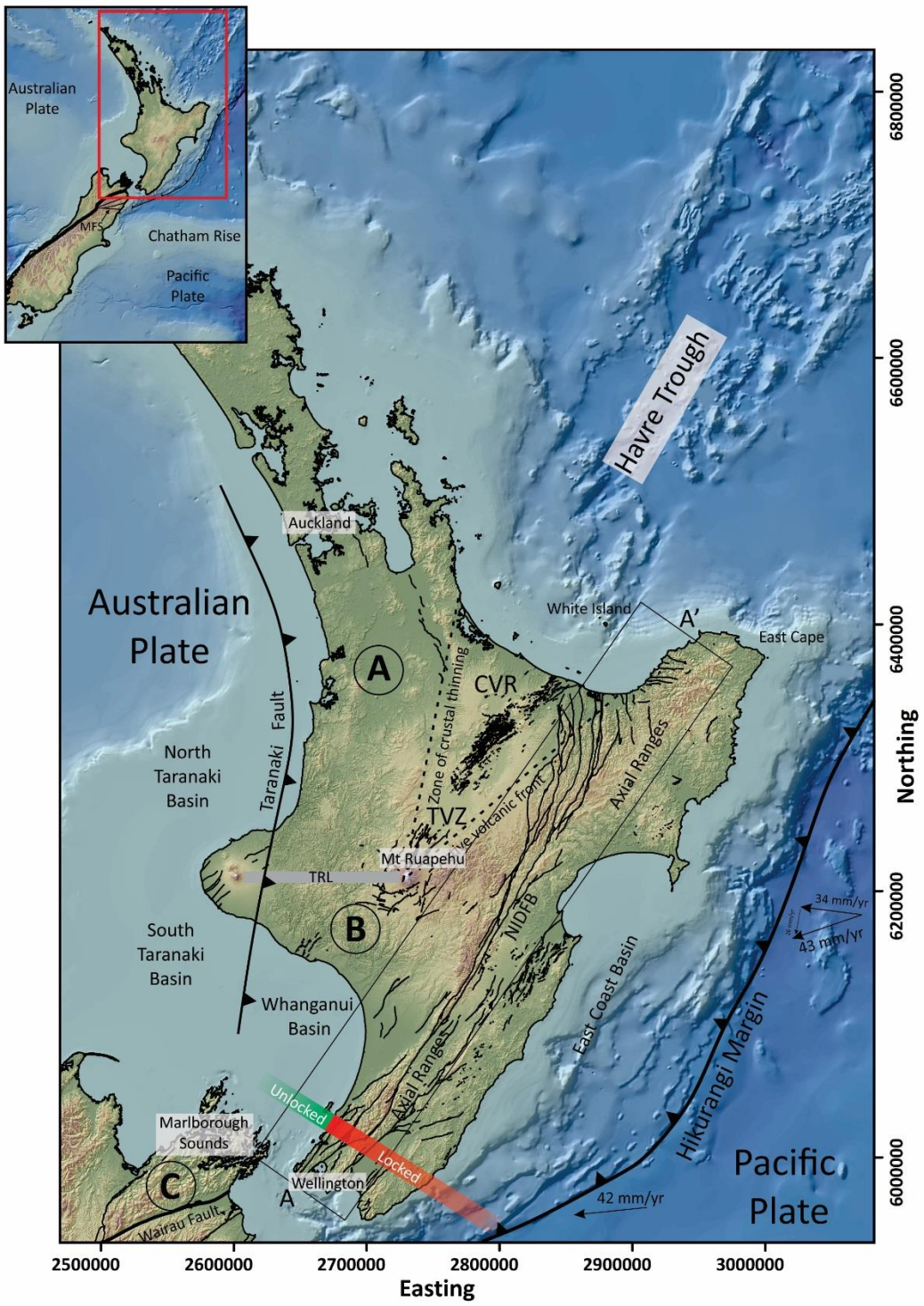

Figure 1.4 Present day tectonic setting for North Island, New Zealand. Letters A, B, and C pertain to the cross-section in Figure 1.3. Cross-section line A – A' pertains to Figure 1.5. Red and green lines represent areas where the plate interface is locked and where there is slow-slip (Henrys et al., 2013). Black vectors represent plate motion of the Pacific Plate relative to the Australian Plate (Beavan et al., 2002; Tozer, 2013).TRL = Taranaki-Ruapehu Line, MFS = Marlborough Fault System, TVZ = Taupo Volcanic Zone, CVR = Central Volcanic Region, NIDFB = North Island Dextral Fault Belt. Bathymetry data from NIWA, DEM from Victoria University, Faults from the active fault database by GNS.

%) on the subduction interface (Nicol et al., 2007). The remaining < 20 % is accommodated in the overlying Australian Plate via folding and thrusting in the fore-arc (Nicol et al., 2007).

In the fore-arc of the Hikurangi Margin, in the Wairarapa, there are documented ongoing, reverse, or oblique reverse displacements (e.g. Lamb and Vella, 1987; Little et al., 2009; Schermer et al., 2009) attributed to horizontal compression in the upper plate. Interestingly however, the major active faults that cut through Wellington (i.e. the Wellington and Ohariu Faults) generally have components of normal dip-slip. For example, a presumed normal component of dip-slip has caused the formation of Wellington Harbour, as well as the Lower Hutt and Upper Hutt Basins (Langridge et al., 2005). This normal component varies along fault strike, but it thought to be up to 1 km (down-thrown to the SE) in some places (Begg et al., 2003).

Across the Wellington region, this change from reverse faulting, on faults such as the Wairarapa Fault (e.g. Little et al., 2009) and the Wharekauhau Thrust (Schermer et al., 2009) to mainly dextral faulting (e.g. Wellington and Ohariu faults) with some vertical movement, potentially suggests that the western Wellington area is not subject to much shortening compared to the Wairarapa. Indeed, Lamb and Vella (1987) suggest a “swing” in the direction of maximum shortening from oblique to the margin trend in Wellington, to perpendicular to the margin trend in the Wairarapa (Walcott, 1978, 1984a).

Plate interface coupling distributions vary both along and perpendicular to the strike of the Hikurangi Margin. In southern North Island, Henrys et al. (2013) proposed that the plate interface changes from being “locked” to “unlocked” perpendicular to plate interface strike defined by an increase in dip to angles greater than 8 °. Plate interface coupling distributions (Wallace et al., 2004) also correlate spatially to basin exhumation magnitude in the Axial Ranges (Jiao et al., 2015) and long-term deformation (Nicol et al., 2007). For example, the plate interface is weakly coupled in the central Axial Ranges, and has had < 1 km of exhumation in the area since the Late Miocene, whereas it is strongly coupled down to approximately 40 km beneath the Wellington region and has had > 4 km exhumation since the Late Miocene (Jiao et al., 2015; Kamp, 2000; Wallace et al., 2004). Walcott (1978)

showed that the plate interface locking behaviour also varies with time as evidenced by altering patterns of strain pre and post the 1931 Napier earthquake (Walcott, 1984a).

The above information indicates that lithospheric deformation of the overriding plate at the Hikurangi Margin is influenced by multiple mechanisms, some of which are not fully understood yet. What we can say, however, is that these mechanisms are a result of subduction development and deformation over the past few million years.

1.2.1 Wellington geological background

Because this thesis focusses on analysing remnants of a former regional erosion surface that is poorly dated (4 – 0.4 Ma), the geological and uplift history of Wellington over the past few million years must be explored. Figure 1.6 displays a stratigraphic column illustrating past geological events relevant to K Surface formation. During Late Eocene to Oligocene time, New Zealand developed into a low lying extensive erosional surface (Begg and Johnston, 2000; Landis et al., 2008). In Wellington, the only onshore sediments exposed from this time period are represented by the Otaihanga outlier (South of Waikanae River) (Begg and Mazengarb, 1996) and two small inliers within the Picton Fault Zone near Picton (Nicol and Campbell, 1990) (Figure 1.7). Stevens et al. (1974) postulated that the K Surface was planated during this time. During the Late Miocene there was uplift and passage through the wave zone as shown by > 4 km of exhumation in Wellington (Kamp, 2000), which could have cut the K Surface.

Six km west of Wellington City, there is a sequence of Early Pliocene marine rocks at Makara (Figure 1.7) preserved in a marine outlier that unconformably overlies Torlesse basement (Begg and Mazengarb, 1996; Grant-Taylor and Hornibrook, 1964). It is located between two inferred splays of the Ohariu Fault, and has been suggested to represent a miniature basin (Grant-Taylor and Hornibrook, 1964; Reay et al., 1988). The deposit, once much more widespread, represents the only known onshore sediments of the South Whanganui Basin (Begg and Mazengarb, 1996). It is weakly indurated and approximately 170 m thick (Begg and Mazengarb, 1996). Figure 1.8 displays a stratigraphic column of the marine outlier, obtained from data from a core drilled in 1988 by the Geophysics Division, Department of Scientific and Industrial Research (DSIR).

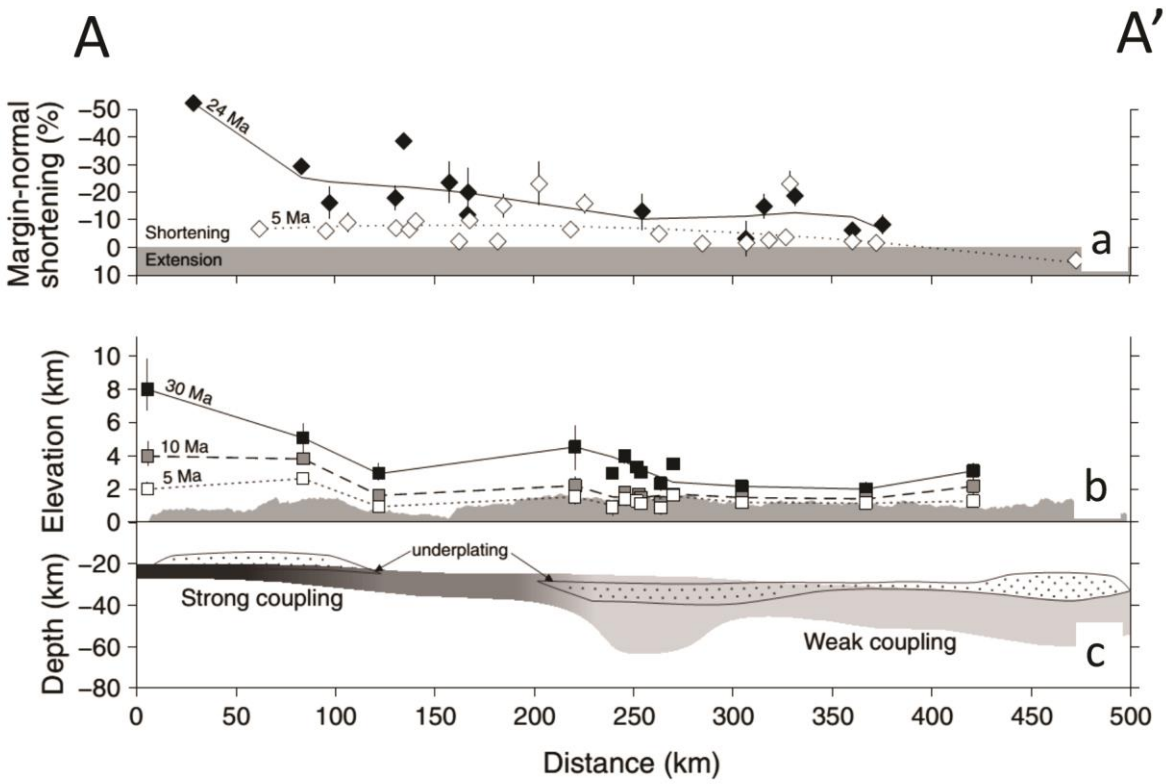

Figure 1.5 Transect along the strike of the Axial Ranges and the strike of the Hikurangi Margin. Cross-section location on Figure 1.4. (a) Margin-normal horizontal shortening strain in the Hikurangi fore-arc for the Miocene (black diamonds) and the Pliocene (White diamonds) (Nicol et al., 2007). (b) Estimated paleo-surfaces for the Axial ranges at 30 (black), 10 (grey), and 5 (white) Ma based on thermal history models by Jiao et al., (2015). Grey region represents present topography of the Axial Ranges. (c) Schematic of the modern subduction interface; the shaded area is subduction interface depth and degree of shading represents degree of coupling (dark = strong coupling, light = weak coupling) between the Pacific and Australian Plates (Wallace et al., 2012). Figure adapted from Jiao et al. (2015).

The deposit exhibits sparse bedding characterised by dips of 5 – 25 ° and generally grades upwards from sandstone into calcareous mudstone. The bedding dips are deemed unusual by Reay et al. (1988) due to the sequences tectonic setting, a sliver between two branches of the Ohariu Fault. The lower part of the deposit is defined by disconformities in the form of conglomerate and grit horizons; there are also shellbeds present (Begg and Mazengarb, 1996). The upper part of the deposit is generally finer grained with more sparsely distributed shells compared to the lower part, and there are concretions scattered throughout (Begg and Johnston, 2000). The formations' weak induration and putty soft" nature lead Reay et al. (1988) to suggest that no sediment of significant thickness (i.e. < 500 m) has overlain the sequence since deposition.

The age of these marine sediments is not well constrained near the base of the sequence. Biostratigraphic ages suggest an upper age limit of Early Opoitian; however, the lower limit could be anywhere between the Kapitean to Late Opoitian (Reay et al., 1988).

This marine outlier indicates that the period of emergence ended in the Middle Pliocene, and was followed by subsidence (Begg and Johnston, 2000; Grant-Taylor and Hornibrook, 1964). This is shown by: 1) Coarse gravels near the bottom of the drill-core that eventually give way to finer grained sediment (Figure 1.8), and 2) a stratigraphically upward increasing pyrite to ilmenite ratio (R. Grapes, personal communication, May 2015). These two lines of evidence suggest a deepening of the marine depositional environment from inner to outer shelf (Begg and Mazengarb, 1996). Therefore, there was submergence in the region during the Opoitian. Post-Opoitian uplift and erosion has removed most of what must have been a substantial cover of the Wellington region, leaving a tiny remnant at Makara (Ota et al., 1981). During this uplift and passage through the wave zone, the K Surface may have been cut. A possible explanation for the preservation of the Makara outlier is that it was downfaulted by the Ohariu Fault (Begg and Mazengarb, 1996).

Locally, there are patches of sediments that rest on the K Surface, or are preserved in miniature basins adjacent to the K Surface. On a farm-track exposure east of Horokiwi stream in Transmission Gulley (R26/736148), Mildenhall and Alloway (2008) record a 1.09 ± 0.12 Ma TVZ silicic tephra, dated using isothermal plateau fission-track (ITPFT) of glass shards. The tephra occurs at c. 8.8 m below the surface as a 20 cm thick bed (Mildenhall and Alloway, 2008). The Rangitawa Tephra (345 ± 12 ka), dated using the weighted mean of nine reliable fission-track age determinations (Pillans et al., 1996) is correlated to sections in Tawa, Whitby, Judgeford and Mangaroa (Te Punga, 1984b). Te Punga (1984b) also reports the tephra in Newtown, Wilton, Johnsonville and Thorndon, although this is not confirmed geochemically.

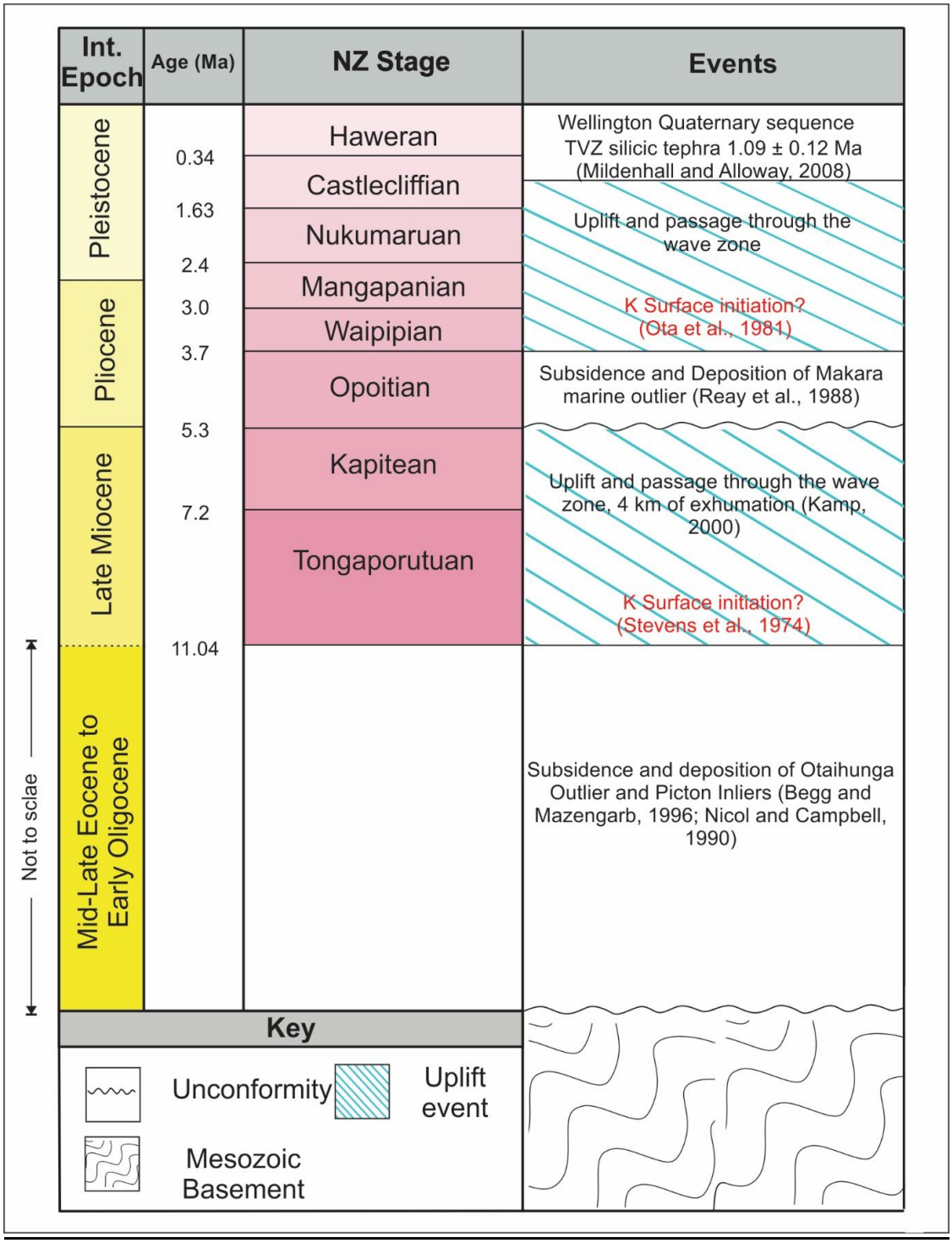

Figure 1.6 Stratigraphic column of geological events relating to K Surface formation.

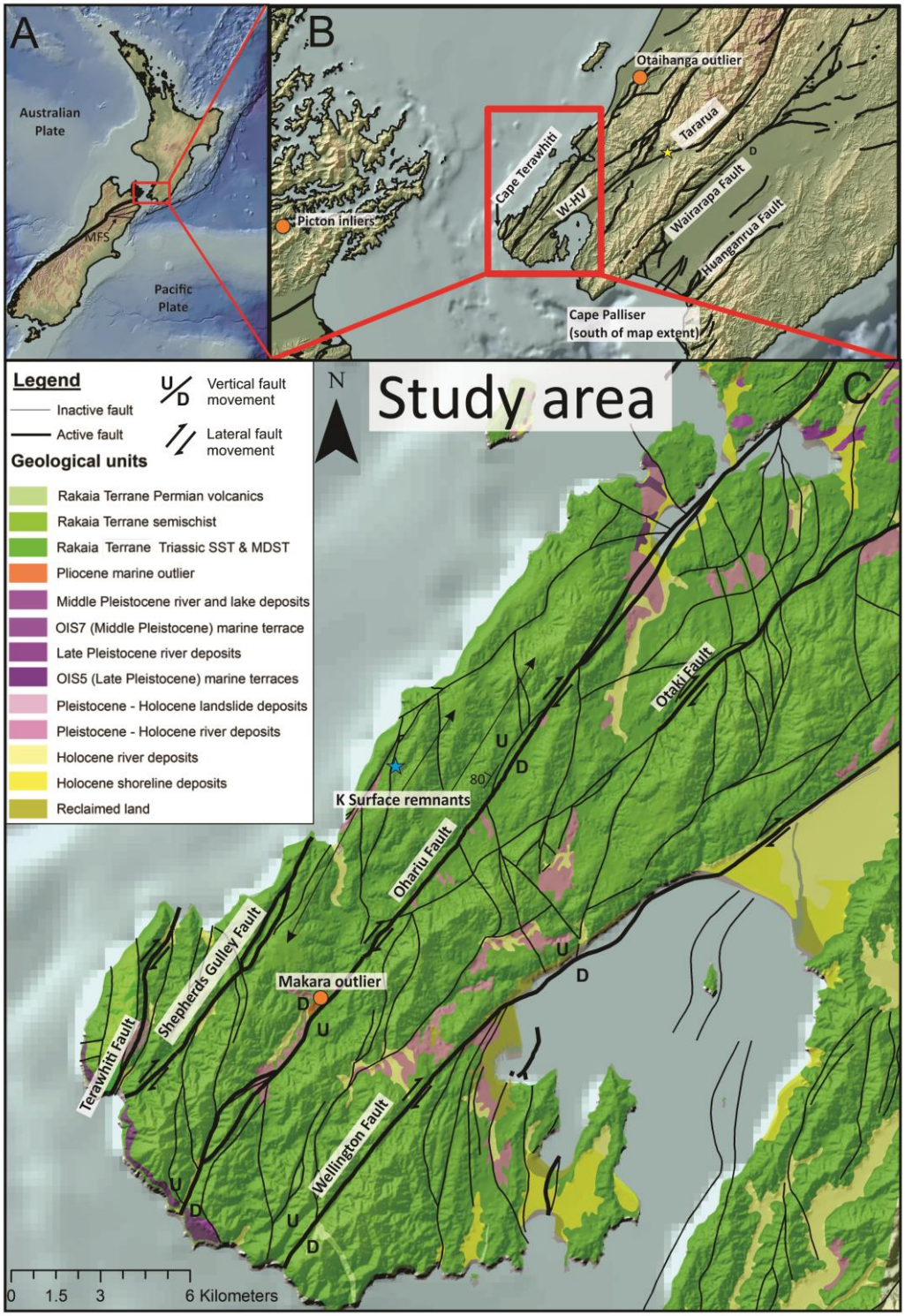

Figure 1.7 (A) Regional figure of the New Zealand subcontinent. (B) Lower North Island and upper South Island, note locations of Oligocene outlier/inliers. (C) Zoomed in view of western Wellington showing active and inactive faults, the Makara marine outlier, and some of the most prominent K Surface remnants. Yellow star in B shows approximate location of Figure 1.9. Blue star in A shows location of Figure 1.10. MFS = Marlborough Fault System, W-HV = Wellington/Hutt Valley segment of the Wellington Fault, Tararua = Tararua segment of the Wellington Fault. Bathymetry data from NIWA, DEM and geology from Victoria University, Faults from the Active Fault Database by GNS.

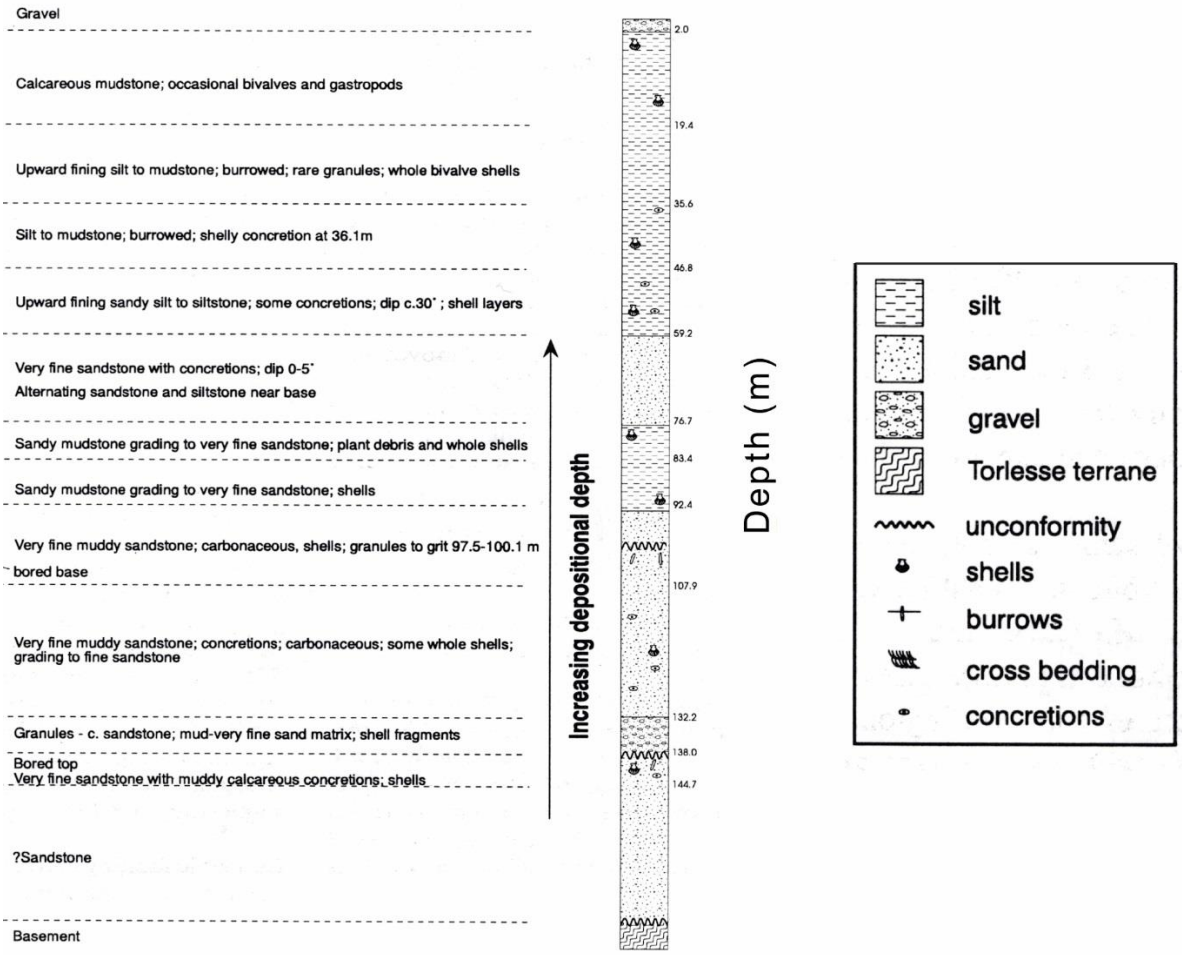

Figure 1.8 Stratigraphic column for the Printers Flat core, drilled near the first hole of the Makara Public Golf Course in 1988. Figure adapted from Begg and Mazengarb (1996).

Since the Quaternary, there has been an onset of dextral strike-slip faulting. Active faults within the Wellington area predominantly strike approximately NE-SW; inactive faults strike both NE and NW, and as a result appear to chop the K Surface into blocks (Figure 1.7). The main active faults in the area of interest are the Ohariu, Shepherds Gully and Wellington faults, which are all right-lateral strike-slip and exhibit slip rates ranging from 1 – 10 mm yr^{-1} (Heron et al., 1998; Langridge et al., 2005; Litchfield et al., 2010; Van Dissen and Berryman, 1996). Slip rates are variable along different parts of each fault (Langridge et al., 2005). For example, on the Wellington Fault, Holocene horizontal slip rates vary along fault strike with values of 5.1 – 6.2 mm yr^{-1}, 6 – 7.6 mm yr^{-1}, and ≥ 4.5 ±

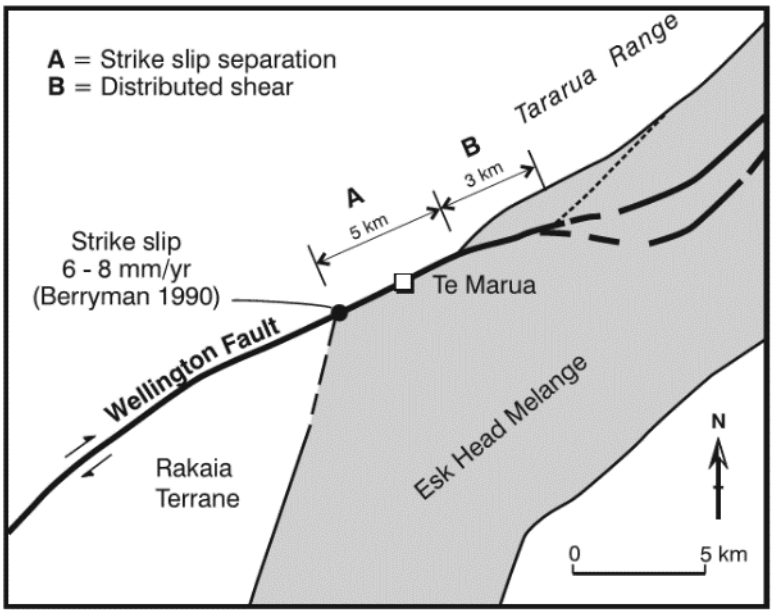

Figure 1.9 The Wellington Fault at Te Marua illustrating a potential total strike separation of up to 8 km and a possible distributed shear along the fault. Figure location displayed as yellow star on Figure 1.7B. Data from Begg and Mazengarb (1996). Figure from Nicol et al. (2007).

0.4 mm yr^{-1} for segments in the Tararua Range, Wellington/Hutt Valley and Te Marua areas, respectively (Langridge et al., 2005; Little et al., 2010). The Wellington Fault vertical to horizontal slip rate ratio commonly exceeds 10:1 in favour of horizontal slip (Langridge et al., 2005). The Ohariu Fault has a Holocene horizontal slip rate of 1 – 2 mm yr^{-1} (obtained from nine sites) and a Holocene vertical slip rate of > 0.06 mm yr^{-1} (obtained from two sites) (Heron et al., 1998).

There are limited data available on the geometry of the active faults, specifically in terms of accurate dips. Nevertheless, through ground-penetrating radar (GPR) techniques, Gross et al. (2004) deduced that at two field sites in the Hutt Valley, the Wellington fault's dip and dip direction is approximately 55 – 75 °SE and 72 – 84 °SE. Furthermore, it was found through trenching on Ohariu Valley Road that the Ohariu Fault dips steeply to the northwest (~80 °) and exhibits apparent reverse displacement (Figure 1.7) (Litchfield et al., 2010).

In Te Marua, near Upper Hutt (Figure 1.9), the Wellington Fault displays an apparent 5 km dextral offset of the Mesozoic aged Esk Head Mélange (Begg and Mazengarb, 1996; Nicol

et al., 2007). There is potentially an additional 3 km of lateral displacement of the Mélange north of the fault, producing a total strike-slip of approximately 5 – 8 km (Begg and Mazengarb, 1996). The total strike-slip amount mentioned above is comparable to the 7 +/- 1 km of dextral displacement concluded from the deflection of rivers that cross the Wellington Fault (Berryman et al., 2002). These offsets are consistent with the insignificant offset of exhumation across the Wellington and Ohariu Faults since the Late Miocene. Indeed, based on the information above, it can be inferred that the Wellington Fault has been active for ~1 Ma.

There are Marine terraces that correlate with Marine Isotope Stages (MIS) 5a, 5e and 7 (80, 120 and 243 ka) that are cut into Greywacke basement on Wellington's south coast between Tongue Point and Cape Terawhiti (Figure 1.7) (Begg and Johnston, 2000). These terraces can be used to infer Quaternary uplift rates for the region. For example, Ota et al. (1981) deduced that the Ohariu Fault has vertically displaced the MIS 5e terrace at Tongue Point (Figure 1.7) 39 m; this corresponds to a vertical uplift rate of 0.31 mm yr^{-1}. Furthermore, Ota et al. (1981) found that the Terawhiti Fault also displaces a (different) MIS 5e terrace 19 m, corresponding to a 0.15 mm yr^{-1} uplift rate.

On the top of the K Surface, at approximately 41°14'S, 174°40'E (Figure 1.7), the stratigraphy consists of Torlesse greywacke, overlain by a discontinuous muddy/pebbly layer, which is then overlain by well sorted, quartz-bearing sands up to ~8 m thick (Figure 1.10). The Torlesse greywacke at this location is oxidised, heavily weathered and deformed. The contact between the Torlesse greywacke and the overlying pebbly muds is hard to pinpoint, due to the highly weathered nature of the outcrop. The ~1.5 m thick muds are oxidised in the lower part of the unit and reduced in the upper part. On initial observation, the sediments seem extremely fine-grained and exhibit organic matter throughout. Upon further inspection however, there are abundant sand to pebble sized fragments (mainly greywacke) imbedded within the muddy matrix. This is potentially suggestive of a colluvium deposit. The well sorted sands stratigraphically above the muds are unevenly draped over the landscape, and have been determined to be 10 – 12 ka through optically stimulated luminescence dating done at Victoria University of Wellington (unpublished). The sands have subsequently been deduced as being windblown (Watson and Norton, 2015) as

evidenced by: 1) large scale cross bedding observed in the strata; 2) well sorted with positive graded bedding (possibly due to sand streams at high wind); 3) spherical grains under the microscope (Figure 1.10B), and 4) lack of pebbles and gravels present (therefore, not fluvial) (S. Lamb, personal communication, April, 2014).

In summary, since the Miocene, Wellington has gone through at least two major uplift events, one of which probably exposed rock to erosional processes which, in turn, cut the K Surface. A range of different processes occurring on different timescales have resulted in the Wellington area we see today.

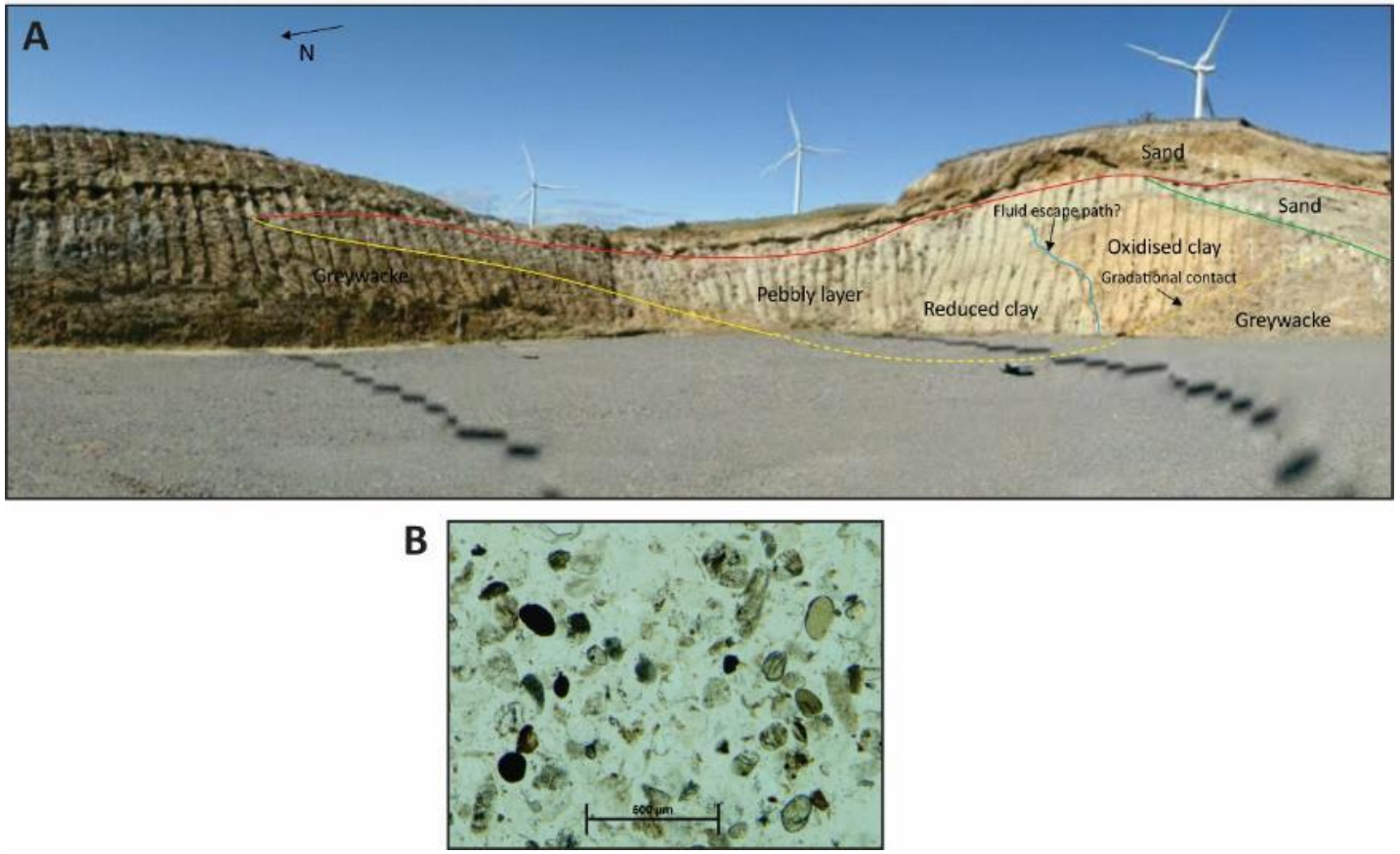

Figure 1.10 A) The stratigraphy on top of the K Surface at Mill Creek Wind Farm, western Wellington (Location: 41°12'S 174°44'E Elevation: ~215 m, B) Thin section of sand dune sand collected from the upper sand layer approximately 20 m west of photo location. Note the roundness of the grains. Figure from (Watson and Norton, 2015).

1.3 Thesis outline

This thesis is structured as follows:

- **Chapter 1** (this chapter) outlines the motivation and objectives of this research project and provides background information on the study area
- **Chapter 2** describes the theory behind gravity surveying and presents results from a gravity survey of Makara Village, Wellington.
- **Chapter 3** covers the theory behind seismic waves and the seismic refraction method, and presents results from a seismic refraction survey done at Makara Village, Wellington.
- **Chapter 4** defines cosmic rays and cosmogenic nuclides, focussing particularly on *in situ* ^{10}Be exposure dating in quartz. This chapter also presents results from a cosmogenic nuclide study done in western Wellington.
- **Chapter 5** presents results from topographic analysis of the K Surface using a 1 m resolution DEM, which include an interpolated map of the K Surface and a map of K Surface remnants.
- **Chapter 6** uses mudstone porosity as a proxy for exhumation to infer the amount of rock uplift that has occurred in western Wellington since the Pliocene.
- **Chapter 7** discusses the results found in Chapters 2 – 6 and their implications for the age, origin and uplift mechanisms of the K Surface.

2 Gravity and Gravity Study of Makara Village

This chapter describes the theory behind gravity studies and presents results from a gravity survey of Makara Village, Wellington. Working for gravity reductions and regional gradient removal are presented in Appendix 1.

2.1 Gravity theory

Newton's law of gravitation forms the basis of the gravity survey method, and states that the force of attraction F between two masses m_1 and m_2 is given by the equation:

$$F = G\,\frac{m_1 m_2}{r^2} \tag{2.1}$$

$$G = 6.67 \times 10^{-11}\ Nm^2/kg^2 \tag{2.2}$$

Where G is the universal gravitational constant and r is the distance between the two masses (Kearey et al., 2002).

If we consider the simple scenario of Earth as a uniform sphere with a mass M and a radius R, the force F acting on a mass m at the Earth's surface can be expressed by the equation (Kearey et al., 2002):

$$F = G\frac{mM}{R^2} \tag{2.3}$$

Newton's second law of motion states that the acceleration a of an object is dependent upon the mass m of the object and the net force F of the object:

$$F = ma \tag{2.4}$$

Substituting equation (2.3) into equation (2.4) yields the equation that describes the acceleration due to gravity, g:

$$g = \frac{GM}{R^2} \tag{2.5}$$

On an Earth such as the one described above, the acceleration due to gravity would be constant on all locations of the Earth's surface (Kearey et al., 2002). Of course, in reality, the Earth is not a homogenous, uniform sphere; it has an ellipsoidal shape, irregular surface

relief, and a heterogeneous density distribution (Davy, 2012; Kearey et al., 2002). Therefore, the potential gravity field varies across the Earth's surface. In geophysics, the unit of gravity is the *milligal* (1 mGal = 0.001 Gal) (Kearey et al., 2002).

2.2 Earth's Gravity

Telford (1990) states that the magnitude of gravity at any point on the Earth's surface is dependent on five factors: (1) latitude, (2) elevation, (3) surrounding topography, (4) tide and instrument drift, and (5) density variations within the Earth. Gravity exploration is primarily concerned with anomalies caused by the last factor (5) and is used to deduce local and regional subsurface structure, depending on the scale of observation (Telford et al., 1990). Through the use of a portable gravity meter, one can observe small changes in rock density and thus, rock mass, at the Earth's surface (Telford et al., 1990). In order to isolate the gravitational effect of differing subsurface structures, and hence, densities, one must reduce gravity readings to a datum (Kearey et al., 2002; Telford et al., 1990).

The following subsections describe how the factors listed above affect this study, and how they are corrected for.

2.2.1 Gravity change with Earth tides

Field gravimeters are accurate enough to measure variations in gravity due to the movements of the Moon and Sun (Telford et al., 1990). Such variations have a range of approximately 0.3 mGal (Telford et al., 1990). We correct for tidal and instrumental drift by using a looping method where we take base station gravity measurements at the beginning and the end of each survey. We then plot the decimal time of each reading taken vs. the gravity reading (mGal) and fit a linear trendline through the data, thus creating a simple drift curve. The gradient of this trendline allows us to correct for the drift of each reading taken in the field.

2.2.2 Absolute gravity

Absolute gravity can be defined as the total acceleration due to gravity at any specific point on Earth, at a particular point in time (Telford et al., 1990). In this study, gravity measurements are made using a La Coste - Romberg 519 gravity meter, which measures relative changes in gravity between observation points, and thus, not the absolute magnitude of gravity at each observation point. Therefore, a site where absolute gravity is

known must be measured during the survey. Then the relative gravity measurements gathered can be used in conjunction with the absolute gravity reference to produce absolute gravity readings for each observation site $g(absolute\ site)$ (Kearey et al., 2002):

$$g(absolute\ site) = g(site) - g(drift\ curve) + g(absolute\ reference) \quad (2.6)$$

Where $g(site)$ is a gravity meter reading measured in the field, converted to mGal, $g(drift\ curve)$ is the gravity meter reading at the absolute gravity reference, corrected for tidal and instrumental drift, and $g(absolute\ reference)$ is the absolute gravity value at this reference point.

In order to attain absolute gravity values for the relative gravity values gathered in the field during this study, relative observations were tied to the absolute gravity station at Victoria University of Wellington (VUW) (Table 2.1).

Table 2.1 Elevation, location and absolute gravity for VUW absolute gravity station. Latitude and longitude were estimated using a base map, and are in the WGS84 datum. Elevation was estimated using a high resolution, 1 m DEM.

VUW absolute gravity station	
Elevation:	107 m
Latitude:	41°17'24"S
Longitude:	174°46'06"E
$g(absolute\ reference)$:	980270.91 mGal

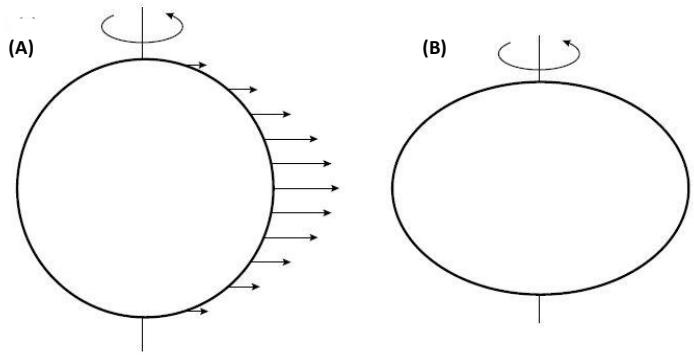

Figure 2.1 (A) Schematic figure showing the variation in centrifugal force with latitude as symbolised by vectors whose lengths are proportional to centrifugal force. (B) An exaggerated visual representation of the Earth. (Kearey et al., 2002)

For this study, absolute gravity values were calculated using *G-solve*, a computer program that reduces relative gravity measurements to absolute gravity values (McCubbine et al., 2014). *G-solve* calculates the mean absolute gravity value at each measurement station corrected for the effects of gravity meter drift (equation 2.6), tidal effects and a calibration scaling factor (McCubbine et al., 2014). *G-solve* also produces a standard error for gravity measurements in mGal. The program also allows to process multiple loops of survey data, thus the drift and meter base line can be measured daily (McCubbine et al., 2014).

2.2.3 Gravity change with latitude

Gravity differs with latitude due to the increase of centrifugal force at a point on the Earth, from zero at the poles to a maximum at the equator (Figure 2.1A) and because of Earth's non-spherical shape (Kearey et al., 2002; Telford et al., 1990). The centrifugal force, caused by the Earth's rotation, has the opposite effect to gravity, and thus causes gravity to increase from the equator to the poles (Kearey et al., 2002). Moreover, the true shape of the earth is an oblate ellipsoid (Figure 2.1B); hence, points on Earth close to the equator are further away from the centre of mass of the earth than those near the poles, which also results in an increase in gravity from the equator to the poles (Kearey et al., 2002).

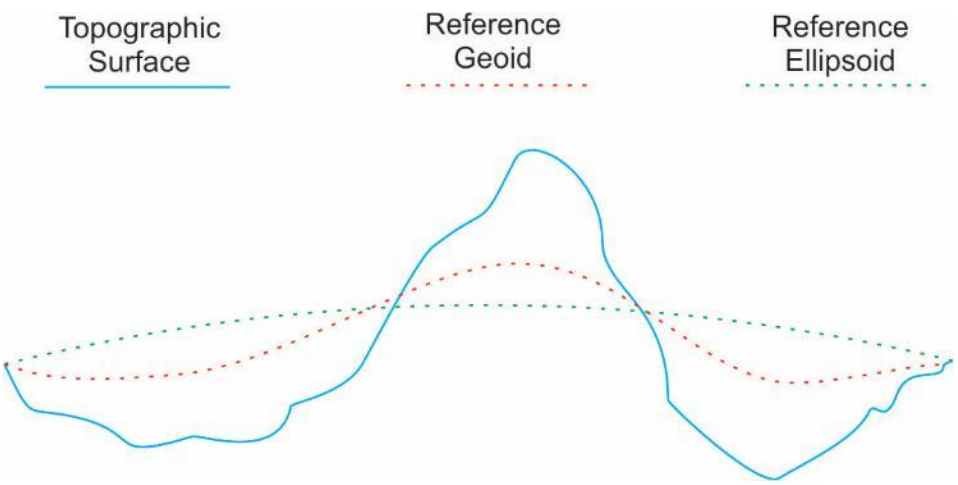

Figure 2.2 The shape of the Earth: Comparison between topographic surface, reference geoid, and reference ellipsoid

The reference geoid is the shape the Earth would be if we only consider the Earth's shape, internal structure and its centrifugal effects (Figure 2.2) (Telford et al., 1990). The reference ellipsoid is an oblate spheroid that approximates the geoid (Figure 2.2) (Telford et al., 1990). Although the ellipsoid differs compared to the geoid, it can still be used to infer a first order measurement of gravity at latitude θ (Telford et al., 1990). In 1930, the International Union of Geodesy and Geophysics created a formula for the approximate value of gravity at a given latitude (g_θ) (Nettleton, 1976). This has since been superseded by the Geodetic Reference System (GRS80) (Hinze et al., 2005; Moritz, 1980). However, we use the 1930 formula as the absolute gravity station used in this study (VUW) was created using the 1930 formula.

$$g_\theta = 978049.00 * (1 + 0.0052884 sin^2\theta - 0.0000059 sin^2 2\theta)\ mGal \qquad (2.7)$$

Where θ is latitude.

For this study, corrections for latitude are done relative to the global reference ellipsoid, WGS84, which is henceforth referred to as the reference ellipsoid.

2.2.4 Gravity change with elevation

Elevation corrections for gravity measurements are made in three parts: a) Free-air correction, b) Bouguer correction, and c) Terrain correction (Figure 2.3). Corrections for elevation change are done relative to the New Zealand Vertical Datum (NZVD), which is henceforth referred to as the reference geoid.

a) Free-air correction

Newton's law (equation 2.1) states that the force of gravity varies inversely with the square of distance (Telford et al., 1990). The free-air correction (FAC) amends this and reduces field measurements to the reference geoid (Figure 2.3a).

$$FAC = -0.3086h\ mGal \qquad (2.8)$$

Where h is height in metres above or below the reference geoid surface. The free-air correction does not account for material between the station and the reference geoid surface (Telford et al., 1990).

b) Bouguer correction

The Bouguer correction (BC) accounts for the material between the field measurement points and the reference geoid surface that is ignored in the FAC (Figure 2.3b). The Bouguer correction assumes an infinite slab with uniform density and thickness and is given by (Kearey et al., 2002):

$$BC = 2\pi G\rho h = 0.04191\rho h\ mGal \qquad (2.9)$$

Where G is the gravitational constant, ρ is the density of the material, and h is the elevation difference between the reference geoid and the field measurement point. In this study ρ is 2.67 g m^{-3}, which is the average density of the continents that are crystalline and of granitic composition (Hinze, 2003).

c) Terrain correction

The key problem with the Bouguer correction, is that it represents topography above the reference geoid as an infinite slab (Telford et al., 1990). The terrain correction corrects for surface irregularities in the surrounding area of a field measurement point.

Figure 2.3c, Area B displays rock material excluded by the Bouguer correction, representing a mass excess. Comparatively, Area A forms part of the Bouguer correction, but does not compose of rock, thus, it represents a mass deficit (Gerkens, 1989; Kearey et al., 2002; Telford et al., 1990). Areas of mass excess and mass deficit both act to reduce gravity at the field

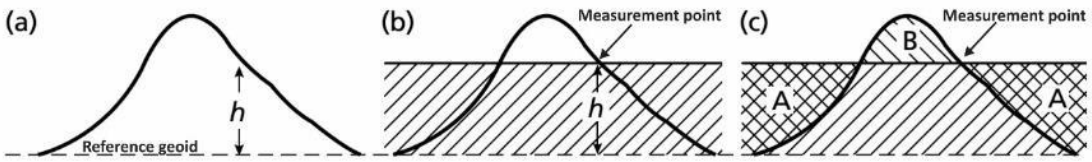

Figure 2.3 (a) Free-air correction, (b) Bouguer correction (c) Terrain correction. Figure adapted from (Kearey et al., 2002)

measurement point (Gerkens, 1989). Hence, the terrain correction is always added to the field measurement (Telford et al., 1990).

The traditional way to estimate terrain corrections is to apply a circular graticule, known as a Hammer chart, which divides the surrounding topography into a series of compartments in the form of circular rings and radial lines (Figure 2.4). Each circular ring represents a Zone. Zone A has a radius of 0 – 2 m, Zone B has a radius of 2 – 17 m, and so on until Zone J which extends to 21.9 km. The graticule is laid on a topographic map and the elevation relative to a survey point is estimated for each compartment (Kearey et al., 2002).

In this study, Zones B to D (2 – 170 m) were estimated both in the field by eye, and through the use of LiDAR data with Zone A (0 – 2m) assumed to be flat. There was a systematic error between the measurements made by eye, and those calculated with the LiDAR. Since the terrain is dominated by steep hillslopes, the manual measurements were discarded in favour of the LiDAR measurements. These field observations were converted to mGal, yielding the inner terrain corrections (T_{inner}). Zones E to J (170 m – 21.5 km) were calculated using a digital terrain model, forming the outer terrain corrections (T_{outer}). The total terrain correction for each measurement point is calculated by:

$$T_{total} = T_{inner} + T_{outer} \qquad (2.10)$$

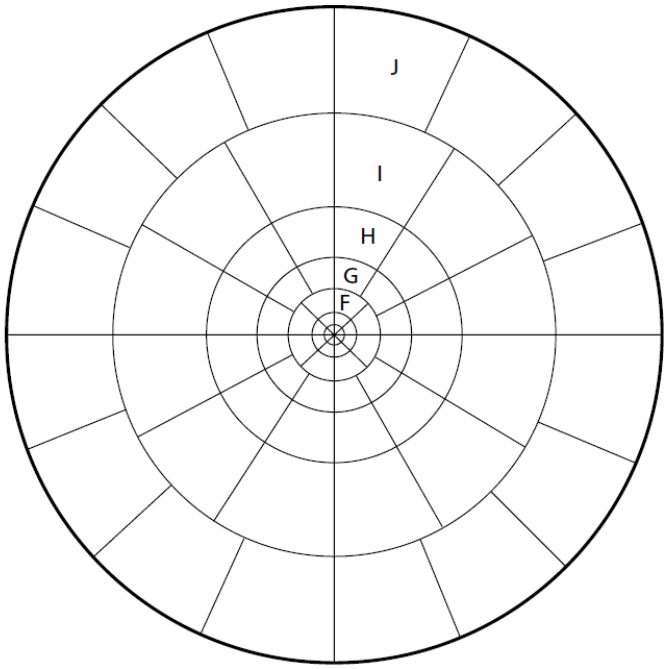

Figure 2.4 A Hammer chart used in the calculation of terrain corrections. Graticules have zones that increase in radii from 2 m to 22 km. (Kearey et al., 2002)

2.2.5 The Bouguer anomaly

The Bouguer gravity anomaly (BA) is the difference between the observed gravity (g_{obs}) and the expected gravity (g_{exp}) at a specific measurement location, where:

$$BA = g_{obs} - g_{exp} \tag{2.11}$$

g_{exp} is sometimes referred to as the Bouguer model, and is calculated by:

$$g_{exp} = g_{\theta} + BC + FAC - T_{total} \tag{2.12}$$

Where g_{θ} is the expected gravity at latitude θ, FAC is the free-air correction, BC is the Bouguer correction, and T_{total} is the terrain correction. By substituting equation (2.12) into equation (2.11), we get:

$$BA = g_{obs} - g_{\theta} - FAC - BC + T_{total} \tag{2.13}$$

Bouguer anomalies are the result of lateral density variations and can be used to interpret and model the Earth's subsurface structure.

2.2.6 Regional gradient and residual anomalies

In this study, the regional model was taken as a linear trend connecting the Bouguer gravity anomaly at the end of each profile line. The regional gradient Rg is calculated by:

$$Rg = \frac{BA\ at\ SE\ end\ ref\ site - BA\ at\ NW\ end\ ref\ site}{distance\ along\ profile\ of\ SE\ ref\ site} \quad (2.14)$$

The regional gravity $g(regional)$ for each observation point is then calculated:

$$g(regional) = BA\ at\ NW\ end\ ref\ site + (Rg) * distance\ of\ site\ along\ the\ profile \quad (2.15)$$

The regionally corrected anomalies $g(residual)$ are then calculated by:

$$g(residual) = BA(site) - g(regional) \quad (2.16)$$

2.3 Gravity observations

The following sub-section describes the reduction and error estimates for gravity measurements acquired during this study.

2.3.1 Instruments used

Gravity meter:

Gravity measurements were made using a Lacoste and Romberg Gravity Meter #G-519 which measures relative gravity units unique to the meter to an accuracy of approximately 0.01 mGal.

GPS:

The location and elevation for each gravity station was measured using a Trimble R8 RTK differential GPS. Each location was calculated relative to New Zealand Transverse Mercator (NZTM) (eastings and northings), then converted to the World Geodetic Service 1984 ellipsoid (WGS84) (latitude and longitude). Each elevation was calculated relative to NZGD2000.

Each gravity station location was taken using the Real Time Kinematic (RTK) module on the GPS where possible. This is where a local base station is set up on a tripod in an area of

high elevation in the field area, and readings for each gravity station are made with a rover that are relative to the local base station. These data are then post-processed relative to permanent GPS stations in the surrounding area at least 24 hours after ending the GPS survey. Fast-static points were measured at gravity stations where the local base station was not visible, and at some stations where RTK measurements were taken as a data quality check. Fast static points differ to RTK measurements, as they do not measure positioning relative to a local base station; rather they communicate directly with the satellites and determine a position.

2.3.2 Field method

The field method used to gather gravity data is not included in this thesis, but follows that of Milsom (2000).

2.3.3 Data reduction

In order to model and interpret the gravity data, field measurements were reduced to Bouguer anomalies using the process described above in section 2.2 and are summarised below:

1. Relative gravity readings were converted to absolute readings and corrected for drift using *G-solve*.
2. The expected gravity at latitude g_θ was calculated using equation 2.7.
3. Free-air corrections, FAC, were calculated using equation 2.8.
4. Bouguer corrections, BC, were calculated using equation 2.9 and a rock density (ρ) of 2.67 kg m^{-3}.
5. Terrain corrections, T_{total}, were calculated as explained in section 2.2.4c above.
6. Bouguer anomalies, BA, were calculated using equation 2.13:

$$BA = g_{obs} - g_\theta - FAC - BC + T_{total}$$

2.4 Gravity survey location

Gravity observations were obtained along two profiles across Makara Village approximately perpendicular to the strike of the Ohariu Fault in order to determine the underlying geology (Figure 2.5). Results are discussed and compared with seismic refraction data obtained in the same location in Chapter 7.

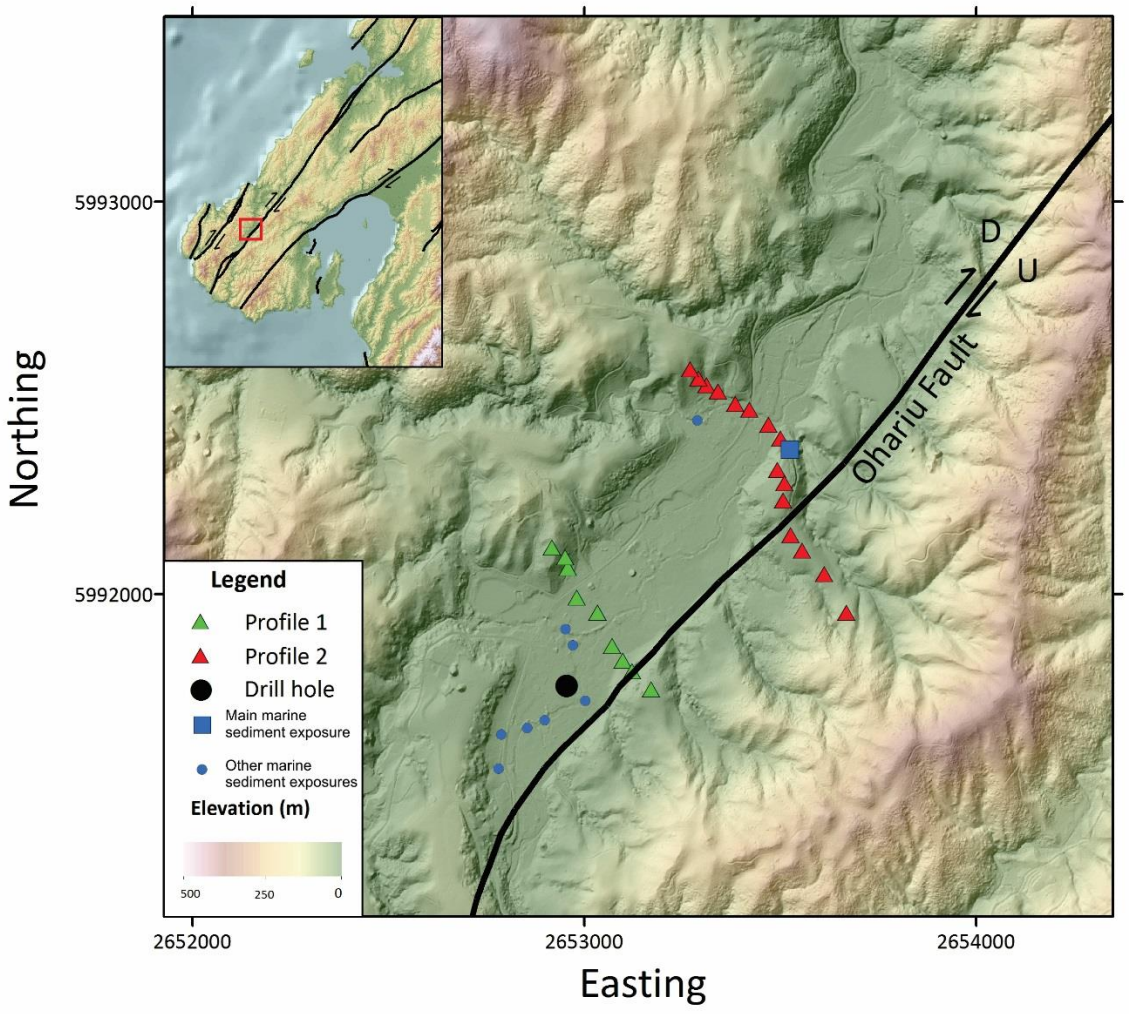

Figure 2.5 Figure of locations for gravity observations for Profiles 1 and 2. The small blue dots represent locations of marine sediment exposures reported by McKay (1877) and Grant-Taylor and Hornibrook (1964).

2.5 Results

2.5.1 Modelling

The gravity data were modelled in *Grav2D* on a Mackintosh laptop.

Regional gradient

The regional gradient was removed from each profile using the method described in section 2.2.6. The calculated regional gradients and azimuths for Profiles 1 and 2 are within 0.00001 mGal m^{-1} and 3° respectively of each other, which indicates that they are insignificantly different (Table 2.2).

Table 2.2 Calculated regional gradients for Profiles 1 and 2

	Profile 1	*Profile 2*
Regional gradient	0.001316 mGal m^{-1}	0.001329 mGal m^{-1}
Azimuth	144°	147°

Model constraints

The information below provides us with constraints for modelling:

- Reay et al. (1988) cored the marine sediment underlying Makara Village, and hit greywacke bedrock at 169 m measured depth (MD) and 163 m true vertical depth (TVD). The majority of the section is Pliocene aged, however the lower bounds are uncertain, and may be as old as middle Miocene (Reay et al., 1988). See Figure 1.6 for drill log. Profiles 1 and 2 were obtained approximately NE of the drilling location (Figure 2.5).
- The overburden is approximately 1.5 m thick, and is ignored in the modelling procedure (Reay et al., 1988).
- Litchfield et al. (2010) through trenching proposed that the Ohariu Fault steeply dips (~80°) to the NW.

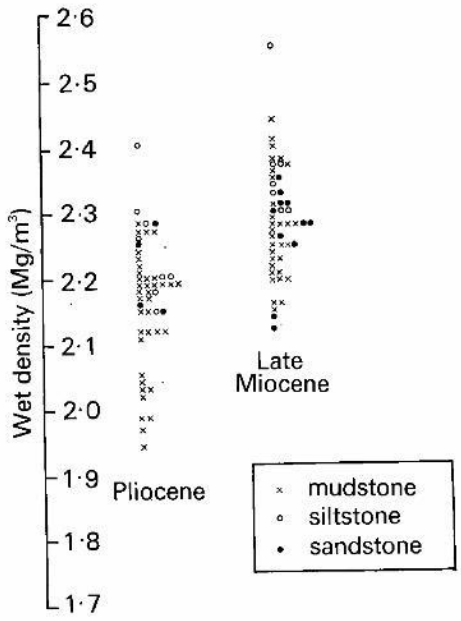

Figure 2.6 Measured porosities for Pliocene and Late Miocene sediments from the Whanganui Basin. Figure adapted from Hunt (1980)

- Grant-Taylor and Hornibrook (1964) describe the only known sizable exposure of the Makara Pliocene marine sediment, which is located on the scarp of the Ohariu Fault (Figure 2.5).
- McKay (1877), Grant-Taylor and Hornibrook (1964) and Begg and Mazengarb (1996) note other smaller exposures in stream channels and road cuttings (Figure 2.5).
- Hatherton and Leopard (1964) determined that Jurassic – Permian greywackes have a density of 2670 ± 30 kg m^{-3} (1 standard deviation).
- Hunt (1969) determined that Pliocene marine mudstone and siltstone from the lower Awatere district have a density of 2200 ± 130 kg m^{-3}.
- Hunt (1980) determined that Pliocene and Late Miocene sediments from the Whanganui Basin have densities of 2200 kg m^{-3} and 2400 kg m^{-3} respectively.
- However, these values are averages; Figure 2.6 displays the range of densities for Pliocene and Late Miocene sediments in the Whanganui Basin.
- Stagpoole (1997) determined an average density of 2150 kg m^{-3} for mudstone and sandstone sediments from the Taranaki Basin buried between 500 – 3000 m.
- A theoretical approach, from Allen and Allen (2013) was used to calculate the bulk density of the marine sediment:

$$\rho_b = \phi\rho_f + (1-\phi)\rho_{ma} \quad (2.20)$$

Where ϕ is the porosity of the rock, ρ_f is the average density of the fluid occupying the pore space, and ρ_{ma} is the average density of the rock matrix. Substituting the average porosity obtained via core plugs during this study (24.8 %) and a grain density of 2530 kg m^{-3} (Hatherton and Leopard, 1964) into equation (2.20) yields a density of 2150 kg m^{-3}.

- We use 2670 kg m^{-3} as the density for the greywacke basement.
- We model both 2150 kg m^{-3} and 2350 kg m^{-3} as the densities for the marine sediment and compare the results. 2150 kg m^{-3} agrees with our theoretical calculation and Stagpoole (1997), and also compares well with measurements from Hunt (1969) and Hunt (1980) for Pliocene sediments. 2350 kg m^{-3} is used because the lower age of the marine sediment is not well defined (potentially could be as old as the middle Miocene), therefore we would expect a higher density near the base of the sequence.

2D models

Figure 2.5 displays the locations for Profiles 1 and 2 and can be referred to when looking at the figures below. Each gravity model displays the inferred location and geometry of the Ohariu Fault, shown by the red dashed line (Litchfield et al., 2010). The "plus" and "minus" symbols represent fault movement into and out of the page respectively. Gravity models for Profile 1 are displayed in Figure 2.7 and Figure 2.8. Figure 2.7 models the Pliocene marine sediment as a wide, shallow body, where (A) has a density of 2150 kg m^{-3} and (B) has a density of 2350 kg m^{-3}. Both models agree with the measured observations and suggest a basin depth of approximately 20 m for (A) and 35 m for (B). These thicknesses are probably too shallow if we consider that depth to basement at the drilling location is 163 m, which is located approximately 130 m SW of Profile 1 (Figure 2.5). Figure 2.8 displays the Pliocene marine sediment as an uneven layer, thickening SE, towards the Ohariu Fault, where (A) has a density of 2150 kg m^{-3} and (B) has a density of 2350 kg m^{-3}. Both models agree with the measured gravity and suggest basement depths of approximately 35 m for (A) and approximately 130 m for (B). Thirty-five metres is probably still too shallow to correlate with the drillhole data; however, 130 m seems a reasonable depth to correlate back to the drillhole. Figure 2.9 and Figure 2.10 display gravity models for Profile 2. Figure 2.9A has a Pliocene marine sediment density of 2150 kg m^{-3}, and (B)

has a density of 2350 kg m^{-3}. Both models agree with the measured points within error, with (A) producing a slightly thinner body. Both models also indicate that the marine sediment is not present in the valley, and that it eventually thickens on the SE side of the Ohariu Fault. This is concerning, considering the marine sediment was observed in the NW of the valley by McKay (1877) (Figure 2.5). However, we are able to model the marine sediment under the valley within error using a density of 2350 kg m^{-3} (Figure 2.10). Thus, based on geological constraints, Figure 2.10 is the most reasonable model for Profile 2.

The initial results of this gravity survey suggest that the Pliocene marine sediment thins towards the NE, and pinches out either prior to, or just after the location of Profile 2. These results are discussed and compared with seismic and geological data obtained in the same area, in Chapter 7.

2.5.2 Uncertainties

Uncertainties discussed and quantified arise from: error in GPS elevations of station heights, terrain correction error, reader error and instrumental drift error.

The horizontal uncertainty in GPS measurements was, on average 1.1 cm. Since an uncertainty of $\pm$ 1 m in latitude results in a Bouguer anomaly error of $\pm$0.00078 mGal, latitude error is considered negligible in this study.

Elevation error for GPS measurements:

Elevation error is critical to consider in a gravity survey, as an elevation uncertainty of ±1 m results in a 0.3 mGal error for the free air anomaly. The vertical positioning error for gravity sites was, on average, 2.5 cm. The vertical positioning error for each gravity site was converted to mGal using the equation:

$$U_{GPSh} = \Delta h(-0.3086 + 0.04191 * 2.67) = 0.19 \Delta h \qquad (2.17)$$

Where U_{GPSh} is the uncertainty in the Bouguer gravity anomaly for GPS readings in mGal, and Δh is the uncertainty in the GPS measurement for a particular gravity station in metres. This yields an average error of 0.00063 mGal.

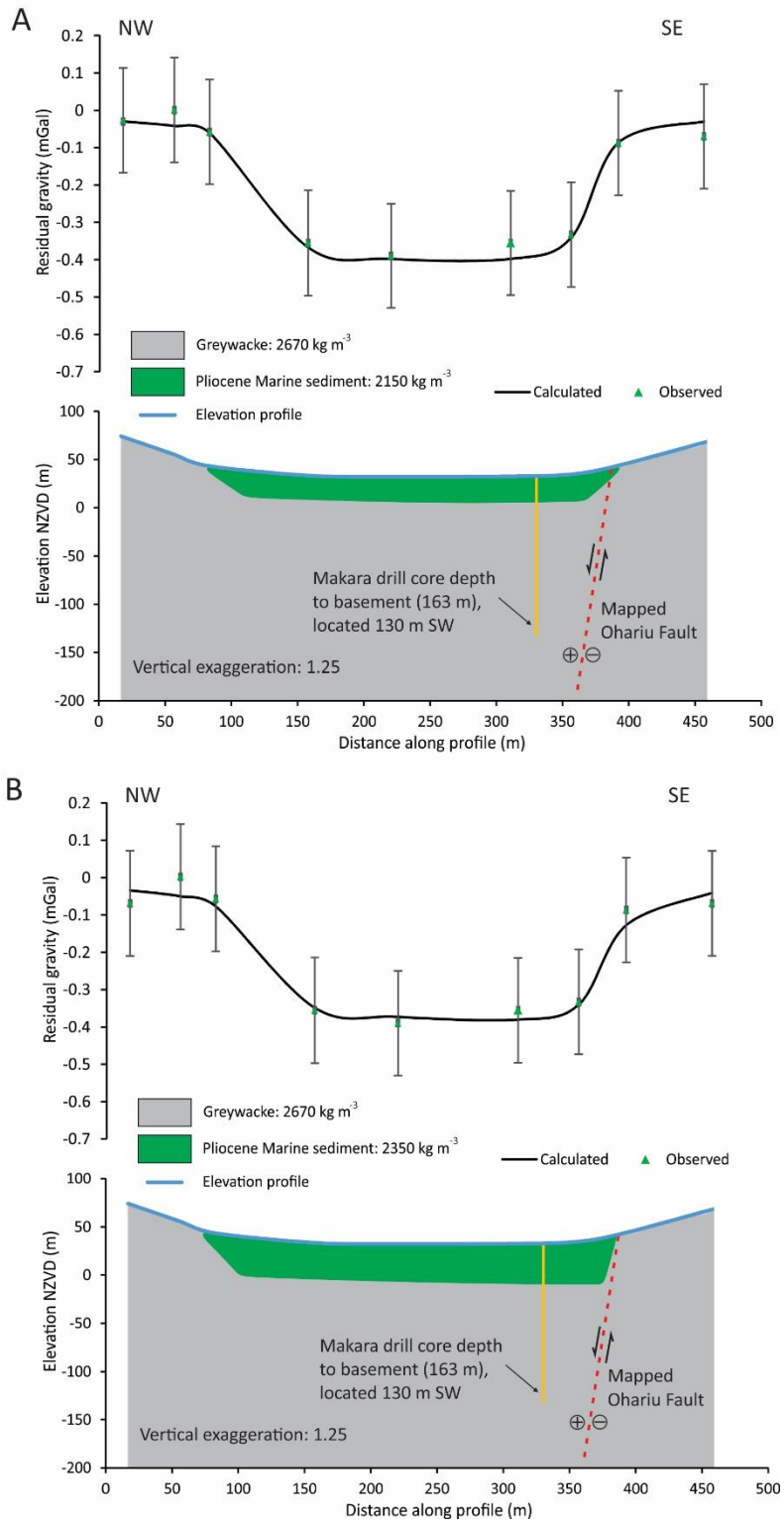

Figure 2.7 Gravity models for Profile 1. The Pliocene marine sediment is modelled as 2150 kg m^{-3} (A) and 2350 kg m^{-3} (B). Green triangles represent the observed gravity data, the black line represents the modelled anomaly, and the grey error bars are the total likely uncertainty for each observation point.

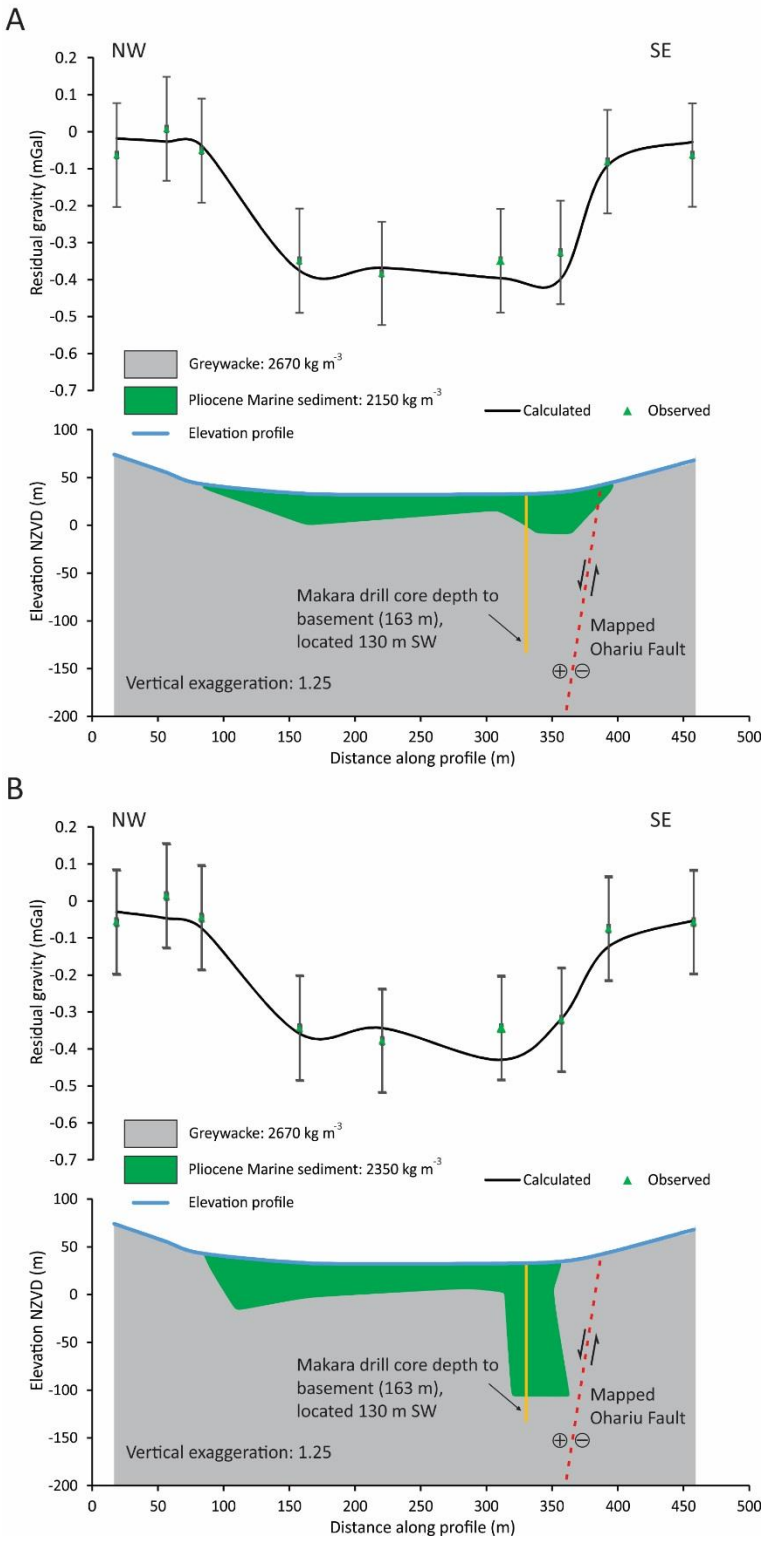

Figure 2.8 Gravity models for Profile 1. The Pliocene marine sediment is modelled as 2150 kg m^{-3} (A) and 2350 kg m^{-3} (B). Green triangles represent the observed gravity data, the black line represents the modelled anomaly, and the grey error bars are the total likely uncertainty for each observation point.

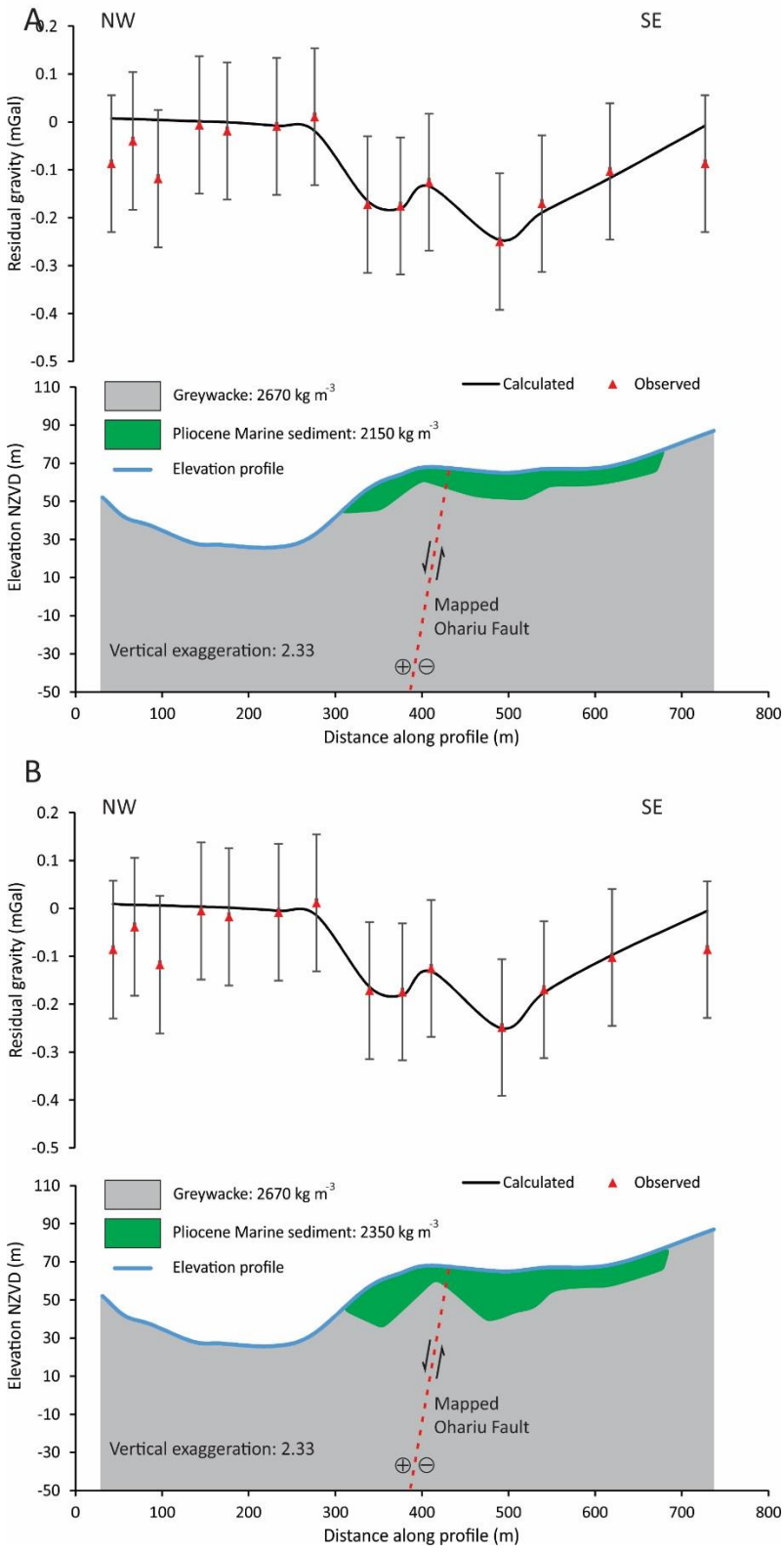

Figure 2.9 Gravity models for Profile 2. The Pliocene marine sediment is modelled as 2150 kg m^{-3} (A) and 2350 kg m^{-3} (B). Red triangles represent the observed gravity data, the black line represents the modelled anomaly, and the grey error bars are the total likely uncertainty for each observation point.

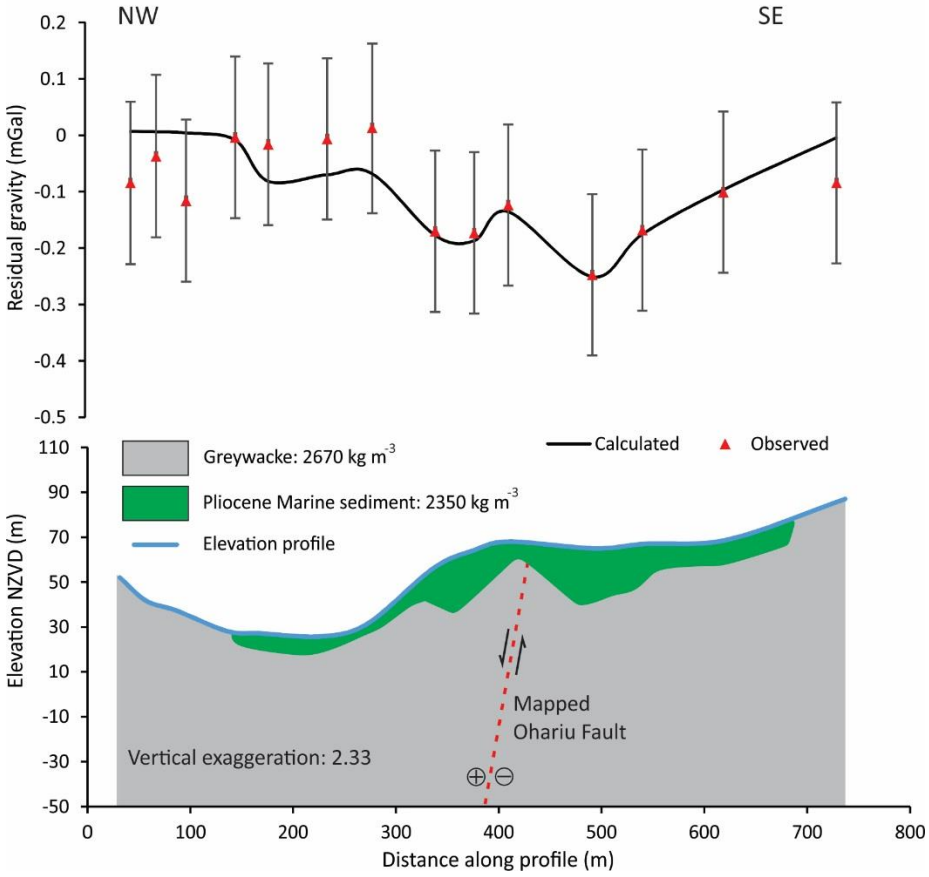

Figure 2.10 Gravity models for Profile 2. The Pliocene marine sediment is modelled as 2350 kg m $^{-3}$. Red triangles represent the observed gravity data, the black line represents the modelled anomaly, and the grey error bars are the likely uncertainty for each observation point.

Terrain correction error:

The terrain correction error is dependent on the quality of the Digital Elevation Model (DEM) used in the calculations. In this study, we calculated inner terrain corrections both in the field by eye and with a 1 m resolution Light Detection and Ranging (LiDAR) dataset. It is impossible to formally calculate inner terrain correction uncertainty as the true error comes from the difference in topographic change in slope between the actual topography, and the LiDAR. The only way to accurately do this would be to measure hillslope profiles in the field, and on the LiDAR, then compare the results. This method would be incredibly time consuming and therefore is not realistic.

Figure 2.11 and Figure 2.12 illustrate the inner terrain correction values calculated in the field by eye (blue) and with the LiDAR (yellow) for Profiles 1 and 2 respectively. We can see that overall the field terrain corrections are smaller than that of the LiDAR. In the case of Profile 2 (Figure 2.12), the trend is similar for both the field and LiDAR corrections. In the case of Profile 1 (Figure 2.11) however, the trends between the LiDAR and by eye calculations are inconsistent. This is not surprising as the LiDAR is 1 m resolution and thus picks up topographical change much more accurately than one can estimate by eye, which is prone to human error. Hence, we discard the field inner terrain correction measurements in favour of the LiDAR measurements. It is important to note that there are systematic differences between the LiDAR elevations at the field sites and the site GPS elevations. The mean difference (GPS – LiDAR) is -0.42 m with a standard deviation of 0.15 m. Consequently, site LiDAR elevations were used for terrain corrections calculated using the LiDAR data.

The rugged terrain of the field area (Figure 2.5) and the occurrence of gravity stations on steep slopes presents a challenge to accurately calculate inner terrain corrections. This is demonstrated by the presence of up to ~ 0.1 mGal of noise when comparing northward and eastward trending Hammer chart for the inner terrain correction (Table 2.3). Moreover, this value could be larger, depending on other, differing orientations of the Hammer chart. For these reasons stated above, we conservatively estimate an inner terrain correction uncertainty of ± 0.15 mGal for each gravity station.

In some cases, gravity station elevations for outer terrain corrections are taken from the DEM. However, DEM site elevations carry error dependent on the resolution of the DEM, resulting in an unnecessary uncertainty in the outer terrain correction.

Therefore, outer terrain corrections for this study were calculated with an 8 m resolution DEM and are relative to the gravity station elevations obtained via the GPS. As GPS elevation error is very small (0.00063 mGal), and considering that the outer terrain correction covers a radial distance of 170 m to 22 km for each gravity station, uncertainties in the outer terrain correction values are considered negligible.

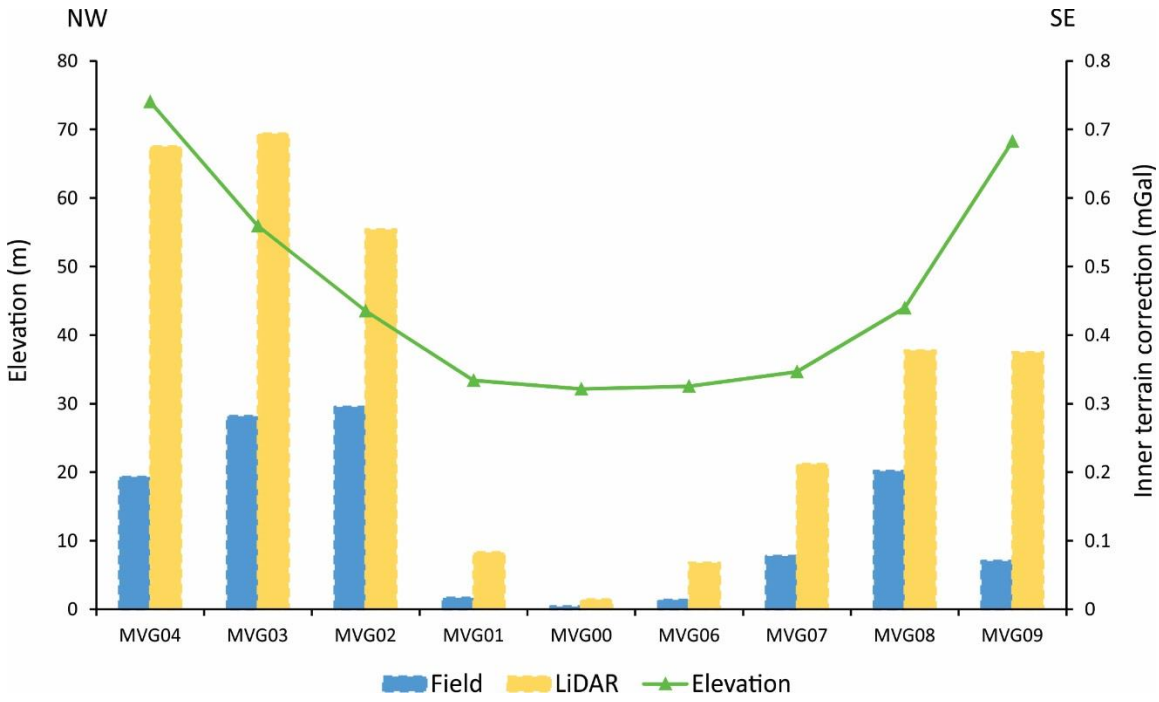

Figure 2.11 Gravity station inner terrain correction values for Profile 1. The blue bars represent field corrections done by eye and the yellow bars represent corrections done with the 1 m resolution LiDAR dataset. The green line represents elevation of the profile. Refer to Figure 2.5 for profile location.

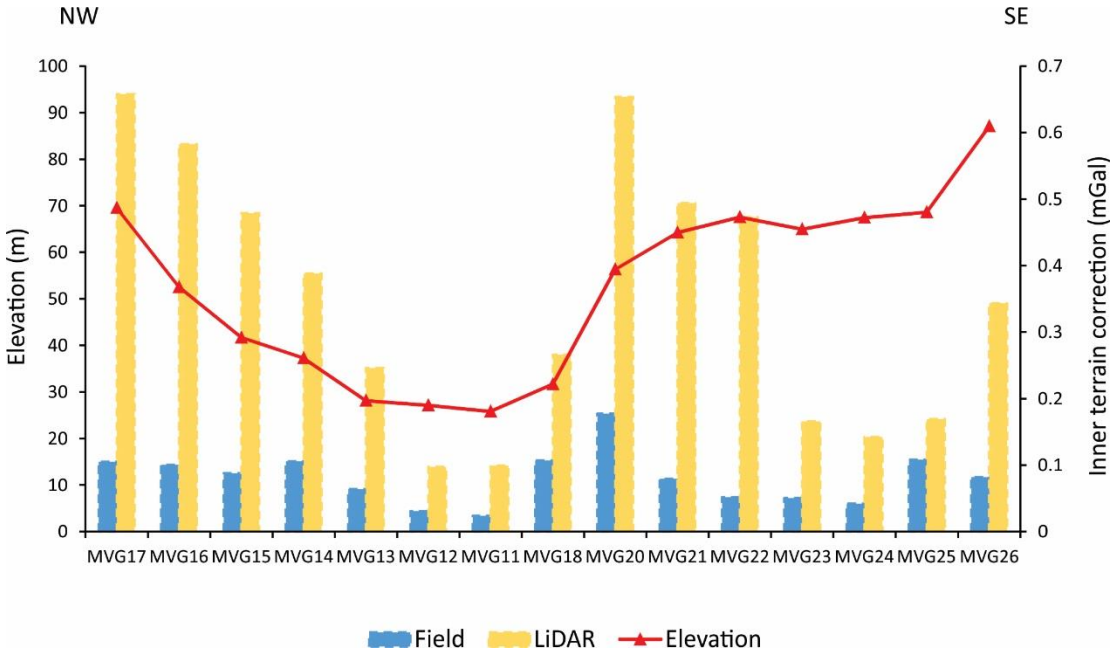

Figure 2.12 Gravity station inner terrain correction values for Profile 2. The blue bars represent field corrections done by eye and the yellow bars represent corrections done with the 1 m resolution LiDAR dataset. The green line represents elevation of the profile. Refer to Figure 2.5 for profile location.

Table 2.3 Inner terrain correction differences (mGal) between north and east trending hammer charts for surveyed gravity stations

Station name	Inner terrain correction difference between north and east trending hammer chart (mGal)
MVG00	-0.0009
MVG01	0.0128
MVG02	-0.0741
MVG03	-0.0796
MVG04	-0.0228
MVG06	0.0054
MVG07	-0.0008
MVG08	-0.0251
MVG09	-0.0072
MVG11	0.0054
MVG12	0.0171
MVG13	-0.0053
MVG14	-0.0565
MVG15	-0.0449
MVG16	-0.0895
MVG17	-0.0350
MVG18	-0.0582
MVG20	-0.0524
MVG21	-0.0277
MVG22	-0.0023
MVG23	-0.0084
MVG24	-0.0198
MVG25	-0.0392
MVG26	-0.0413

Reader error and instrumental drift error:

Reader error and drift error are taken into account through *Gsolve*, which produces a standard error for each calculated absolute gravity value in mGal.

Gsolve data quality check

A residual value is the difference between the measured value of a reading and the value obtained by a model. *Gsolve* produces a residual value for each gravity observation. Figure 2.13 displays a cumulative distribution function (CDF) plot of the residuals, where the orange line represents normal frequency, or modelled data, and the blue line represents actual frequency, or measured data. The mean is 0.00, and the standard deviation is 0.008. We can see from the CDF plot that 68% of the residuals are within one standard deviation of the mean, and 95% within two standard deviations of the mean.

Total likely uncertainty:

The total likely uncertainty for the Bouguer anomaly U_{likely} at each gravity station is given by:

$$U_{likely} = \sqrt{U_{GPS}^2 + U_{Gsolve}^2 + U_{Inner\ TC}^2} \tag{2.18}$$

Where U_{GPS} is the elevation uncertainty, U_{Gsolve} is the uncertainty calculated by *Gsolve* and $U_{Inner\ TC}^2$ is the inner terrain correction uncertainty.

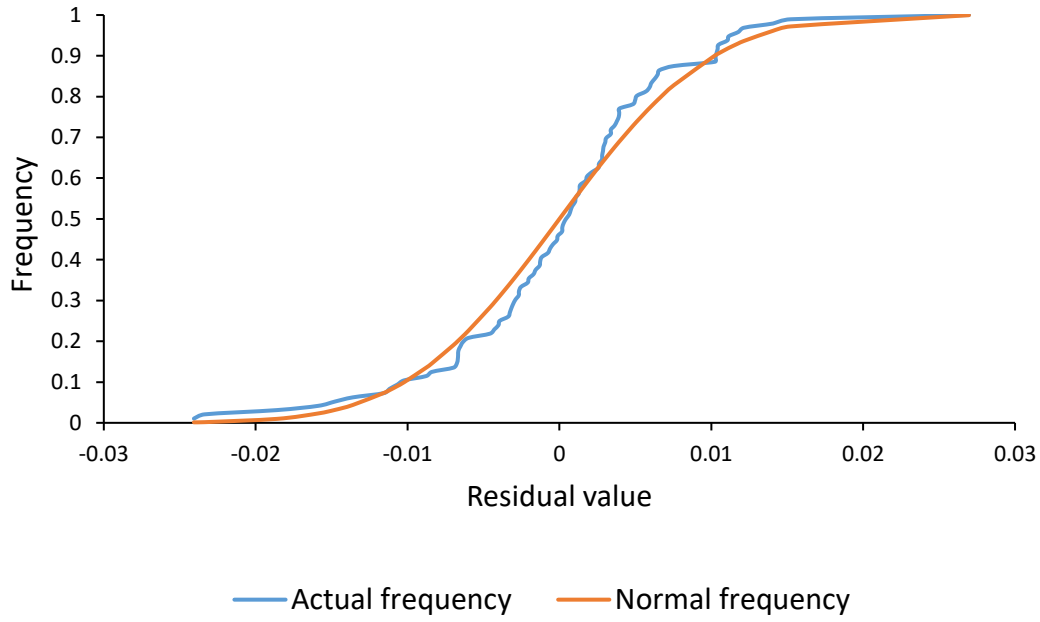

Figure 2.13 A cumulative distribution function (CDF) for all loops, mean = 0.00, standard deviation = 0.008. The blue line represents the residual values for measured data and the orange line represents modelled values.

3 Seismic Theory and Seismic Refraction Survey of Makara Village

This chapter describes the theory behind seismic waves, the seismic refraction method, and presents results from a seismic refraction survey done in January 2015 at Makara Village, Wellington.

3.1 Seismic wave theory

Seismic waves are packages of elastic strain energy that spread outwards radially from a seismic source, such as an earthquake, an explosion, or the strike of a hammer on a metal plate. The strains associated with a seismic pulse travelling through rock are assumed elastic except within the immediate vicinity of the source (Kearey et al., 2002). Under this assumption, the velocites of seismic waves are determined by the elastic moduli and the density of the rock through which the wave is travelling. The source generates a pulse with a wide range of frequencies and travels at a velocity determined by the physical properties of the surrounding rocks (Kearey et al., 2002). In the case of a homogeneous rock, the wavefront, defined as the position where all points of the pulse have reached at a particular time, will appear spherical (Figure 3.1) (Kearey et al., 2002).

Seismic waves can be divided into two groups; body waves and surface waves. Body waves are able to travel through the interior of an elastic solid and are split into two types; P-waves and S-waves. P-waves are compressional waves that travel via compressional and dilatational uniaxial strains in the direction of wave propagation (Figure 3.2a) (Bolt, 1982). S-waves are shear waves that travel via a pure shear strain that is perpendicular to the direction of wave propagation (Figure 3.2b) (Bolt, 1982).

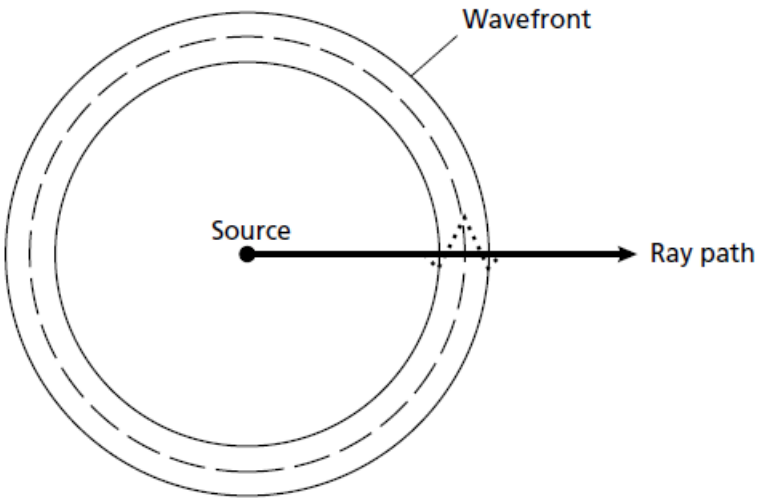

Figure 3.1 The relationship between a raypath and an associated wavefront. (Kearey et al., 2002)

The velocity of a body wave through a homogenous, isotropic material is calculated by:

$$v = (elastic\ modulus\ of\ material)/\rho)^{1/2} \qquad (3.1)$$

Where ρ is the density of the material.

Therefore, the velocity of a P-wave v_p where the appropriate elastic modulus is the axial modulus, is calculated by:

$$v_p = \left(\frac{\Psi}{\rho}\right)^{1/2} \qquad (3.2)$$

The velocity of an S-wave v_s where the appropriate elastic modulus is the shear modulus, is calculated by:

$$v_s = \left(\frac{\mu}{\rho}\right)^{1/2} \qquad (3.3)$$

Because $\Psi = K + \frac{4}{3}\mu$, v_p is also equal to:

$$v_p = \left(\frac{K + \frac{4}{3}\mu}{\rho}\right)^{1/2} \qquad (3.4)$$

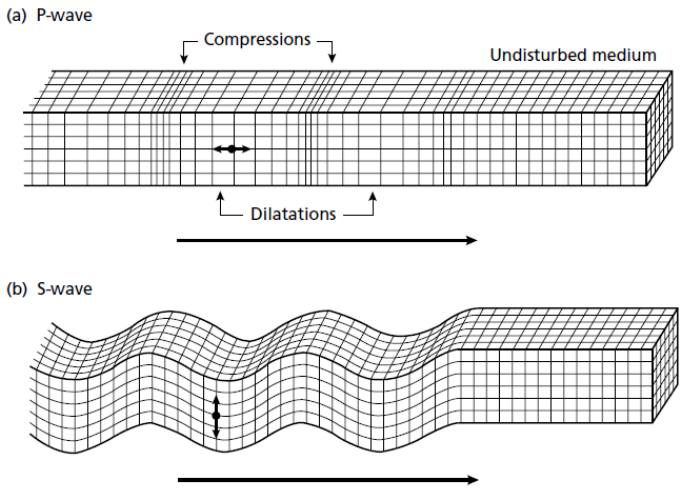

Figure 3.2 Particle motions for body waves (a) P-wave, (b) S-wave. (Bolt, 1982)

From the above equations we can see that compressional waves will always travel faster than shear waves through the same material.

The ratio of P-wave velocity/S-wave velocity (V_p/V_s) can be used to derive Poisson's ratio σ:

$$\frac{V_p}{V_s} = \left(\frac{2(1-\sigma)}{1-2\sigma}\right)^{1/2} \tag{3.5}$$

Poisson's ratio is independent of density, thus it is a good indicator for lithology and is used in this study (Kearey et al., 2002).

3.1.1 Seismic ray theory

Seismic rays are lines normal to the wavefront (in isotropic media) that propagate outwards from the source (Figure 3.1). It is accepted that seismic wave propagation can be estimated using raypaths instead of wave fronts, as raypaths are much easier to analyse when using travel time data, and also provide a sensible approximation of seismic wave behaviour (Telford et al., 1990).

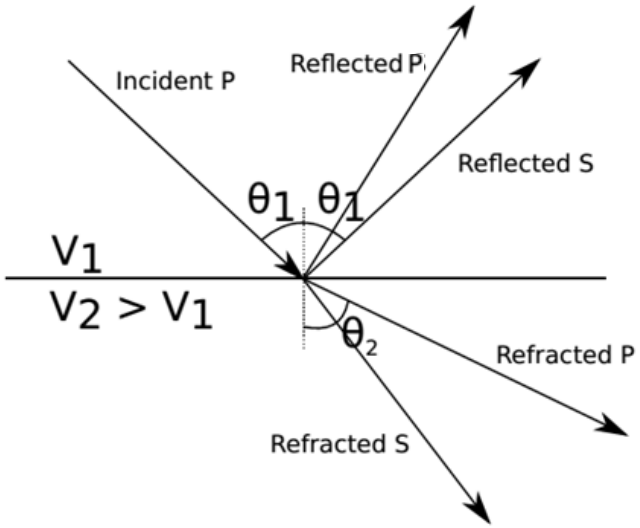

Figure 3.3 A schematic displaying Snell's Law of an incident P-wave partitioning at an interface of acoustic impedance contrast into reflected and refracted P and S-waves. Θ_1 = angle of incidence/reflection, Θ_2 = angle of refraction, v_1 = velocity in layer one, and v_2 = velocity in layer two. Figure adapted from Tozer (2013).

3.1.2 Reflections and refractions of seismic waves

As a P-wave incident ray obliquely approaches an interface, over which, there is an abrupt change in elastic properties, it splits into both reflected and refracted P and S-waves of which, the total energy is the same as the incident ray (Figure 3.3) (Kearey et al., 2002).

Snell's Law determines the geometry and velocities of these rays:

$$p = \sin i/v \qquad (3.6)$$

Where p is the ray parameter, assumed to be constant, and v is the velocity of a ray that is travelling at an angle of inclination i. Therefore, for the refracted P-wave displayed in Figure 3.3, we can state:

$$\frac{sin\theta_1}{v_1} = \frac{sin\theta_2}{v_2} = p \qquad (3.7)$$

Note that when $v_2 > v_1$, then $\theta_2 > \theta_1$, that is, the wave is refracted towards the interface and away from the normal. The reflection angle also follows Snell's Law whereby the angle of reflection is equal to the angle of incidence (Figure 3.3) (Kearey et al., 2002).

Where $v_2 > v_1$, as the angle of incidence is increased, the refracted ray will eventually travel along the interface at velocity v_2 (Kearey et al., 2002). This angle is the critical angle

(θ_c). When the critical angle is exceeded, total internal reflection of the incident ray occurs (Kearey et al., 2002).

$$\frac{sin\theta_c}{v_1} = \frac{sin90°}{v_2} \tag{3.8}$$

Thus,

$$\theta_c = sin^{-1}\left(\frac{v_1}{v_2}\right) \tag{3.9}$$

3.2 The seismic refraction method

Seismic refraction surveying involves recording the first arrivals of seismic energy, which are in the form of either a direct ray or a refracted ray, then, using travel-time data, interpret information relating to refractor depth and morphology (Telford et al., 1990).

With travel-time data, one must make the decision whether to fit connected straight-line segments representing equal velocity layers (Figure 3.4A), or to fit a continuous smooth curve to the data implying a subsurface model that increases continuously with depth (Figure 3.4B). Both methods rely on there being an increase in velocity with depth, where the presence of low velocity layers will result inaccurate depth estimates. The most common situation is that the velocity does increase with depth, usually due to compaction effects (Kearey et al., 2002).

Figure 3.4A is an example of fitting straight-line segments to a travel-time data to resolve for a horizontal, planer interface. Although this specific method is not used on the data gathered in this project, as the subsurface structure is more complex, it is useful to illustrate the different ways to interpret travel-time data at a basic level. We do, however employ the plus-minus method of Hagedoorn (1959) which allows one to interpret irregular interfaces from the geometry of refracted raypaths, and is described in more detail below.

3.2.1 The plus-minus method

The plus-minus method of Hagedoorn (1959) is useful for determining the morphology of non-planar interfaces, which appear on travel time plots as irregular straight-line segments (Figure 3.5). The plus-minus method allows one to derive individual delay times for the

calculation of depths to an irregular reflector for a forward and reverse shot along a single profile line where reciprocal times match (Figure 3.5) (Kearey et al., 2002). Hence, to understand the plus-minus method, one must understand the concept of delay time.

Consider a two layer case where $v_1 < v_2$. The travel time t of the headwave at offset distance x is given by:

$$t = \frac{x}{v_2} + t_i \tag{3.10}$$

Where the time intercept t_i is composed of two delay times from the top layer at each end of the raypath:

$$t_i = \delta_{ts} + \delta_{tg} \tag{3.11}$$

Where δ_{ts} is the delay time at the shot point end and δ_{tg} is the delay time at the geophone point end. The delay time is the time difference between path AB through v_1 and the time required for the ray to travel along BC at velocity v_2 (Figure 3.6). Equation (3.10) explains how the total travel time is the time taken to travel along the offset distance x at velocity v_2 plus t_i, the time taken for the wave to travel down to the refractor at velocity v_1 at the shot point and the geophone.

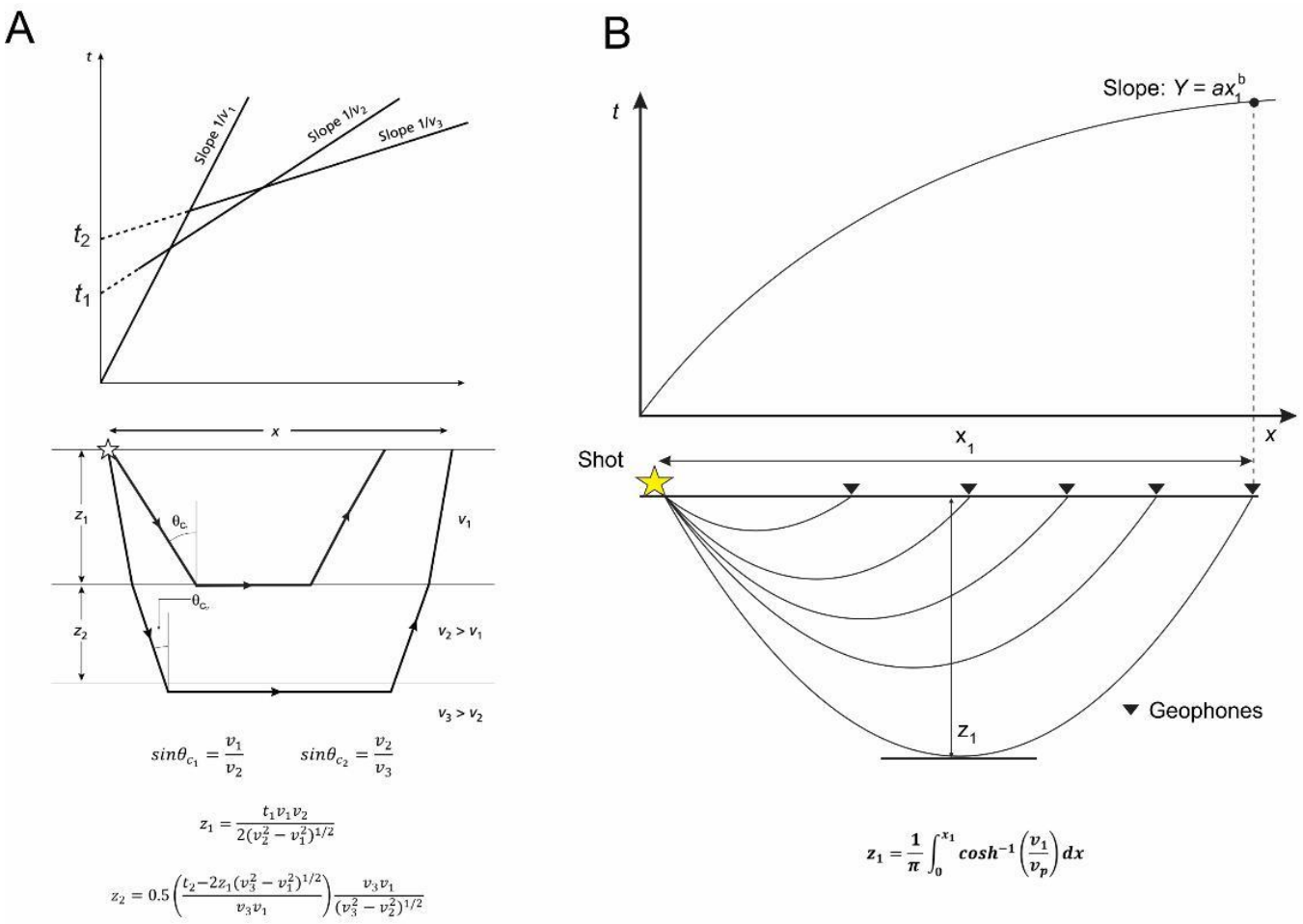

Figure 3.4 Examples of different styles of interpretation for seismic refraction data. A) The planar non-dipping layer using the time intercept method. Adapted from Kearey et al. (2002). B) The continuous velocity model with depth, created using the WHB integral (Grant and West, 1965).

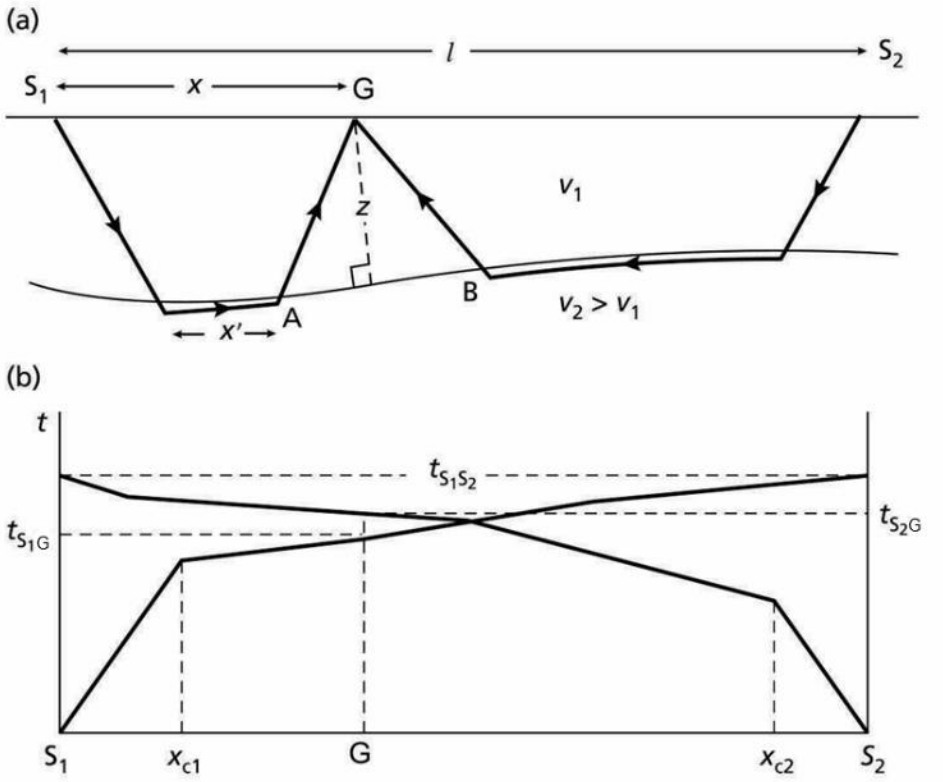

Figure 3.5 An example of the plus-minus interpretation method for seismic refraction (Hagedoorn, 1959). (a) A 2D model of refracted raypaths from each end of a seismic profile to a detector position, (b) travel time curves in the forward and reverse directions for shot 1 (S1) and shot 2 (S2). Figure adapted from (Kearey et al., 2002)

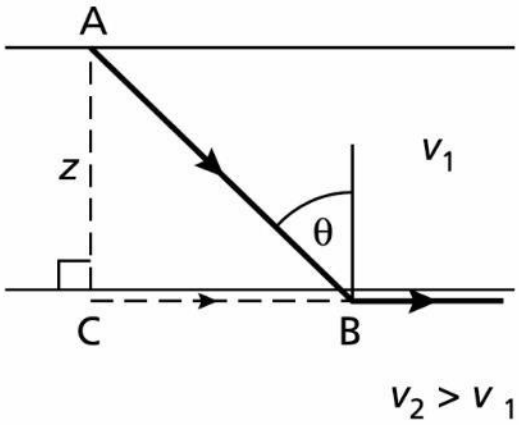

Figure 3.6 The concept of delay time (Kearey et al., 2002)

Figure 3.5 illustrates a two layer model with an undulating refractor surface where $v_1 < v_2$. Raypaths shown are related to a reversed refraction profile line with a length l, between two shot points, S_1 and S_2. The travel-time for a refracted ray propagating from one end of the line to the other is given by:

$$ts_1s_2 = \frac{l}{v_2} + \delta_{ts_1} + \delta_{ts_2} \tag{3.12}$$

Where δ_{ts_1} and δ_{ts_2} are the delay times for the shot points, and ts_1s_2 is the total travel time (reciprocal time) (Figure 3.5). The travel times for rays pertaining to S_1 and S_2, travelling to the geophone G are calculated by:

For shot point S_1:

$$t_{s_1G} = \frac{x}{v_2} + \delta_{ts_1} + \delta_{tG} \tag{3.13}$$

For the reverse ray, from shot point S_2:

$$t_{s_2G} = \frac{(l-x)}{v_2} + \delta_{ts_2} + \delta_{tG} \tag{3.14}$$

Where δ_{tD} is the delay time at the geophone.

v_2 cannot be directly calculated from the undulating travel-time curve; rather it is estimated by taking the difference between the travel times at an intersection (geophone location) of the forward and reverse shot headwaves (Figure 3.5). This is called the "minus" term of the plus-minus method (Hagedoorn, 1959):

$$t_{s_1G} - t_{s_2G} = \frac{2x}{v_2} - \frac{l}{v_2} + \delta_{ts_1} - \delta_{ts_2} \tag{3.15}$$

$$= \frac{(2x-l)}{v_2} + \delta_{ts_1} - \delta_{ts_2} \tag{3.16}$$

As this deduction removes the variable delay time δ_{tG} from the equation, and since the terms δ_{ts_1} and δ_{ts_2} are constant for a profile line, plotting the minus term ($\delta_{ts_1} - \delta_{ts_2}$) vs. distance ($2x - l$) yields, for each geophone, a straight line with a gradient of $\frac{1}{v_2}$, and thus can be used as an estimate of v_2 (Figure 3.5).

Arrival times that are not from the same refractor, or lateral velocity variations within a layer will cause the plot to curve away from a straight line (Lay and Wallace, 1995). Therefore, the minus term also acts as a quality control check for the plus-minus method and allows one to determine the cross-over distances and thus the usable range of geophones (Kearey et al., 2002; Telford et al., 1990).

Once the minus terms for each geophone within the two crossover distances for the forward and reverse shots are obtained, the delay times can then be calculated; this is called the "plus" term

$$t_{s_1D}+t_{s_2D} = \frac{l}{v_2} + \delta_{ts_1} + \delta_{ts_2} + 2\delta_{tD} \tag{3.17}$$

Substituting equation (3.12) into the above equation produces

$$t_{s_1D}+t_{s_2D} = t_{s_1s_2} + 2\delta_{tD} \tag{3.18}$$

Therefore:

$$\delta_{tD} = \frac{1}{2}(t_{s_1D}+t_{s_2D} - t_{s_1s_2}) \tag{3.19}$$

This delay time is used to calculate the depth z to the underlying refractor for each geophone (Figure 3.5) using the equation:

$$z = \delta_t v_1 v_2/(v_2^2 - v_1^2)^{1/2} \tag{3.20}$$

<u>Assumptions and approximations:</u>

- The plus-minus method is only appropriate where there are shallow refractor dips < 10° because with increasing refractor dip, the difference between x and x' increases (Figure 3.5a).
- The refractor is assumed to be planar between the headwave emergence points for the forward and reverse shots at each geophone (Figure 3.5a) (Kearey et al., 2002).

3.2.2 The Wiechert-Herglotz-Bateman integral

The Wiechert-Herglotz-Bateman (WHB) integral uses seismic travel-time data to calculate the distribution of velocity with depth (Lay and Wallace, 1995; Nowack, 1990):

$$z_1 = \frac{1}{\pi}\int_0^{x_1} cosh^{-1}\left(\frac{v_1}{v_{pa}}\right)dx \qquad (3.21)$$

The WHB integral assumes a continuous increase in velocity with depth and a laterally homogeneous medium (Lay and Wallace, 1995; Stratford and Stern, 2006). A continuous velocity model with depth cannot be attained if there is a low velocity layer below a higher velocity layer within the structure (Lay and Wallace, 1995). Indeed, the characteristics of the travel-time data are commonly far from the assumption of the WHB method (Málek et al., 2004). This limitation can be overcome by interpolating between data points (Lay and Wallace, 1995).

We apply equation (3.21) to our data using the following steps:

1) We first smooth the data by applying a best-fit polynomial to the travel-time data as has been done in previous studies (e.g. Novotný et al., 2004; Stratford and Stern, 2006) using the numerical function:

$$Y = ax^b \qquad (3.22)$$

   Where Y is the calculated travel time for refracted arrivals, x is offset, and ^{b} is the order of the polynomial (Figure 3.4B).

2) Depth z_1 is the maximum depth or turning point of a ray which arrives at a geophone at point x_1 (Figure 3.4B). At this depth, the velocity is v_1 which is calculated using the slope of the time-distance plot (equation 3.22). We differentiate equation (3.22) and input offset distance x_1 to attain the ray parameter (v_{pa}) for each geophone between the shot point and x_1 (Figure 3.4B).
3) Because we have determined v_{pa}, we can now numerically calculate z_1 through the integration of equation (3.21) (Figure 3.4B).
4) We obtain the turning point of rays which arrive at other geophones by changing the offset distance value (x) and repeating the above steps.

3.3 Seismic survey location and line geometry

A seismic refraction survey was conducted at Makara Village, Wellington in January 2015 in order to measure P-wave velocity variation with depth, and to determine the shallow subsurface structure of Makara Village. Two lines were shot, one NW – SE line, approximately perpendicular to the strike of the Ohariu Fault, and one SW – NE line, approximately parallel to the strike of the Ohariu Fault (Figure 3.7). Survey geometry is displayed in Table 3.1. A sledge hammer and a thumper were used as seismic sources.

Table 3.1 Survey geometry for seismic survey

	Line length (m)	**Line spacing (m)**	**Total record length (s)**	**Sampling rate (s)**
Line 1	70.5	1.5	Variable, see Appendix 2	Variable, see Appendix 2
Line 2	141	3	1	0.001

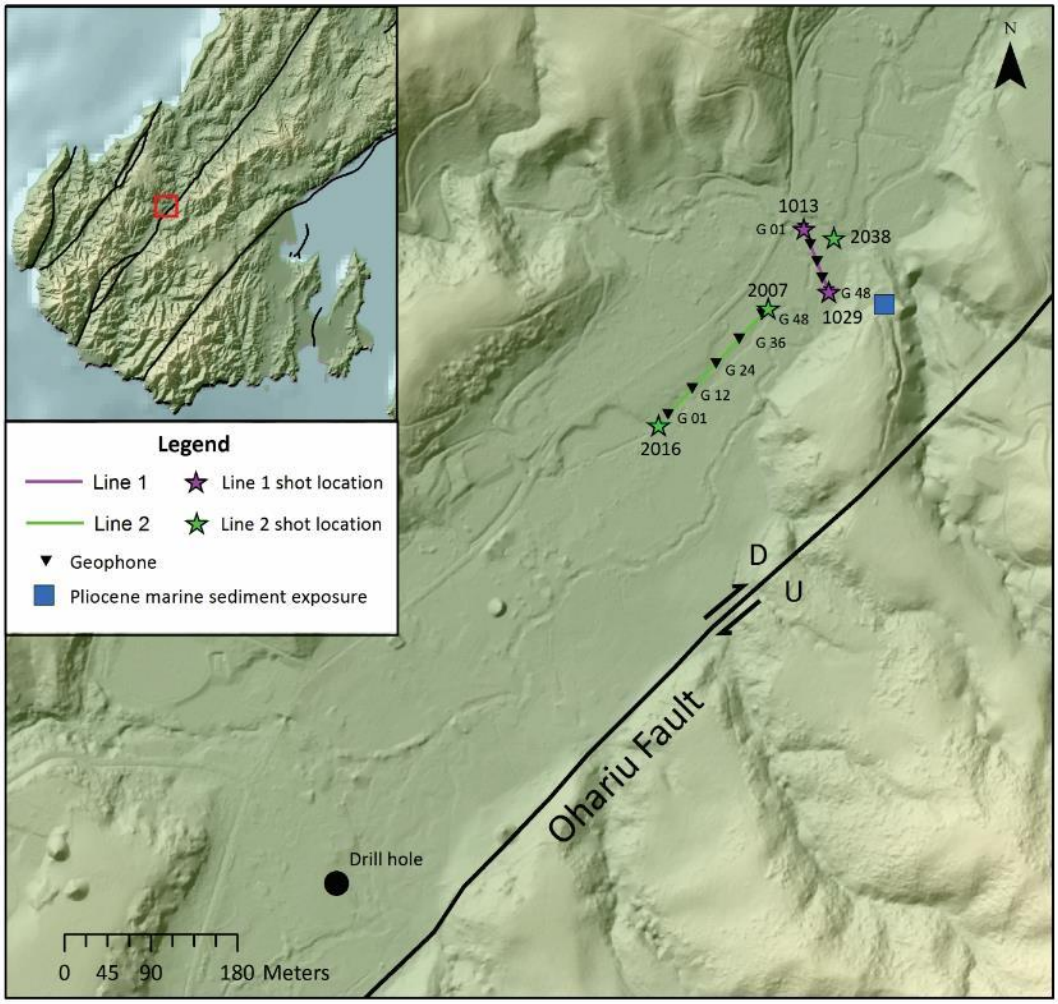

Figure 3.7 Location map for the seismic survey. Black inverted triangles represent geophone locations. Numbers next to the triangles represent line number and channel number. Stars represent shot locations. DEM from Landcare Research, faults from GNS Active Fault Database.

3.4 Data processing

Data were processed with GLOBE *Claritas* on a Linux machine. Survey geometry was defined within the program in order to account for shots that were taken at distances away from the geophones, both parallel and perpendicular to the array. An Automatic Gain Control (AGC) with a window of 250 msec and a bandpass frequency filter with corner frequencies of 5, 10, 80 and 110 Hz were applied when picking first breaks. Trace 38 was nulled prior to picking as it was noisy and interfered with the data. Figure 3.8 andFigure 3.10 display examples of shot gathers with picked P and S waves.

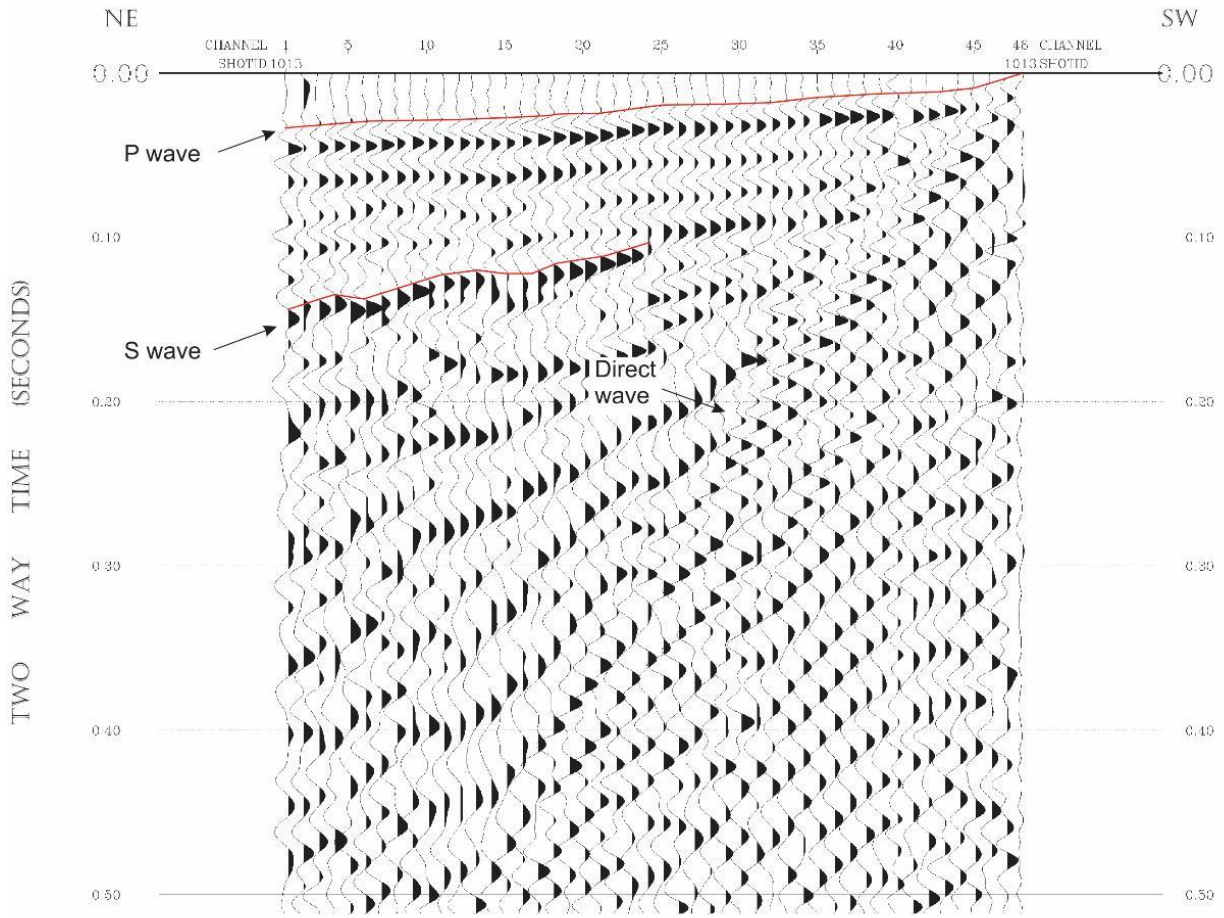

Figure 3.8 Shot gather for shot 1013. P, S and Direct arrivals are labelled. Shot location displayed on Figure 3.18. Figure exported from GLOBE Claritas.

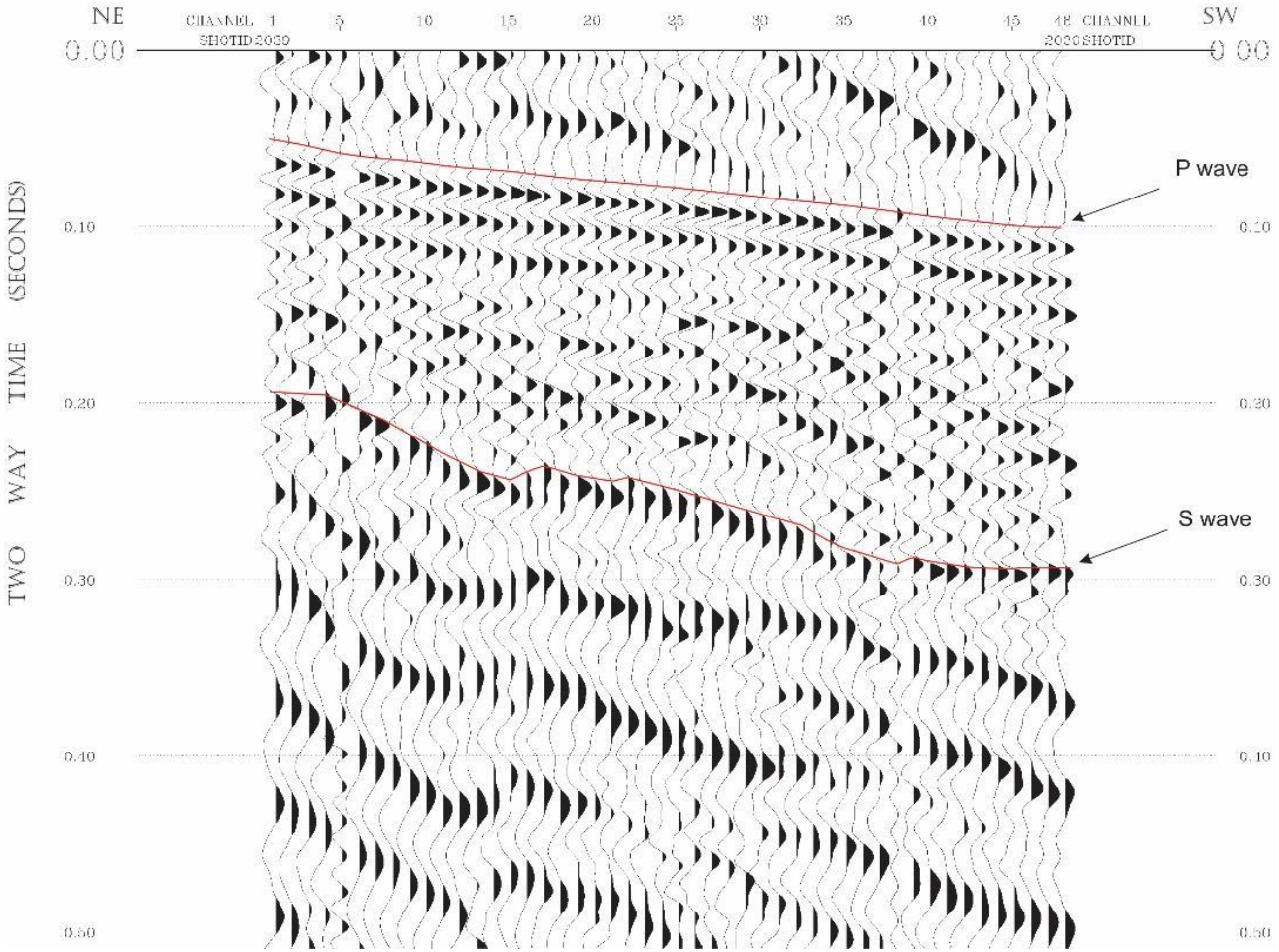

Figure 3.9 Shot gather for long offset shot 2039. P and S arrivals are labelled. Shot location displayed on Figure 3.18. Figure exported from GLOBE Claritas.

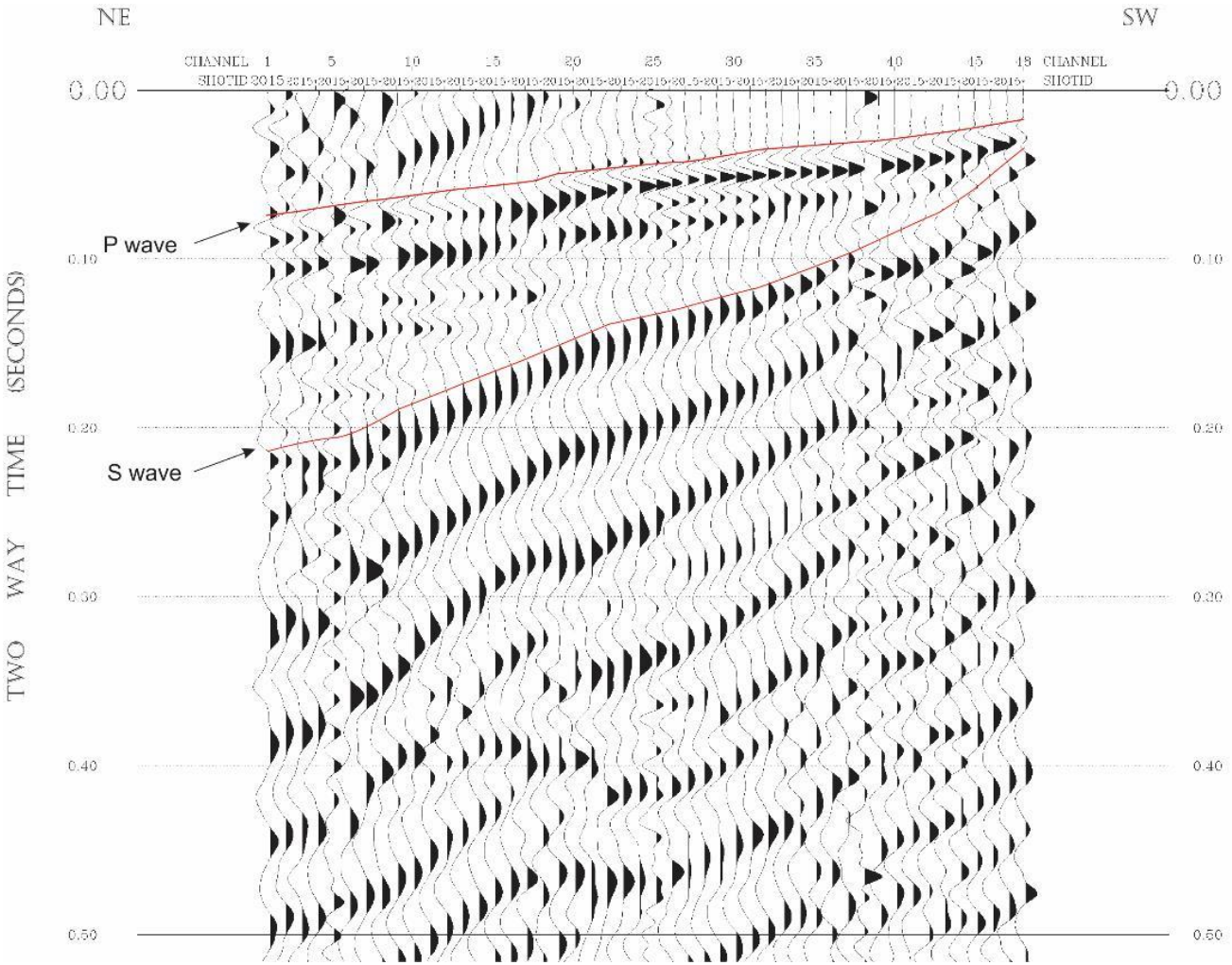

Figure 3.10 Shot gather for long offset shot 2015. P and S arrivals are labelled. Shot location displayed on Figure 3.18. Figure exported from GLOBE Claritas.

3.5 Results

This section presents the results of the seismic survey carried out at Makara during January 2015.

3.5.1 Plus-minus method

We exploit the plus-minus method using shots 1013 and 1029 on Profile 1 and shots 2006 and 2016 on Profile 2 (Figure 3.7). Figure 3.11 displays the time-distance plots for both profiles. The reciprocal times match within 10 % total travel time for both Profiles 1 and 2. This indicates that the plus-minus method is applicable for both profiles.

Line 1: shots 1013 and 1029

Figure 3.12 displays distance vs. minus times (equation 3.15) for shots 1013 and 1029, calculated using the methodology described in section 3.2.1. The data plot as a straight line, which suggests, as explained in section 3.2.1, that there is no lateral velocity variation in layer V_2 and that both shots are sampling the same refractor. Using the gradient of the line in Figure 3.12 we calculate V_2 to be 2.6 ± 0.02 km s^{-1}. Figure 3.13 exhibits the morphology of the V_1/V_2 refractor, calculated for each geophone using equation (3.24).

V_1 is variable along the line (0.5 km s^{-1} – ~0.7 km s^{-1}), which suggests that V_1 represents some sort of overburden or fill material, possibly fluvial as a stream is present in the current landscape, proximal to the location of Profile 1 (Figure 3.7). The V_1/V_2 refractor exhibits two distinct dips, the deeper one located proximal to the scarp of the Ohariu Fault. These undulations may be representative of: 1) A paleo-stream channel(s), 2) faulting effects of the proximal Ohariu Fault, or 3) a combination of 1) and 2).

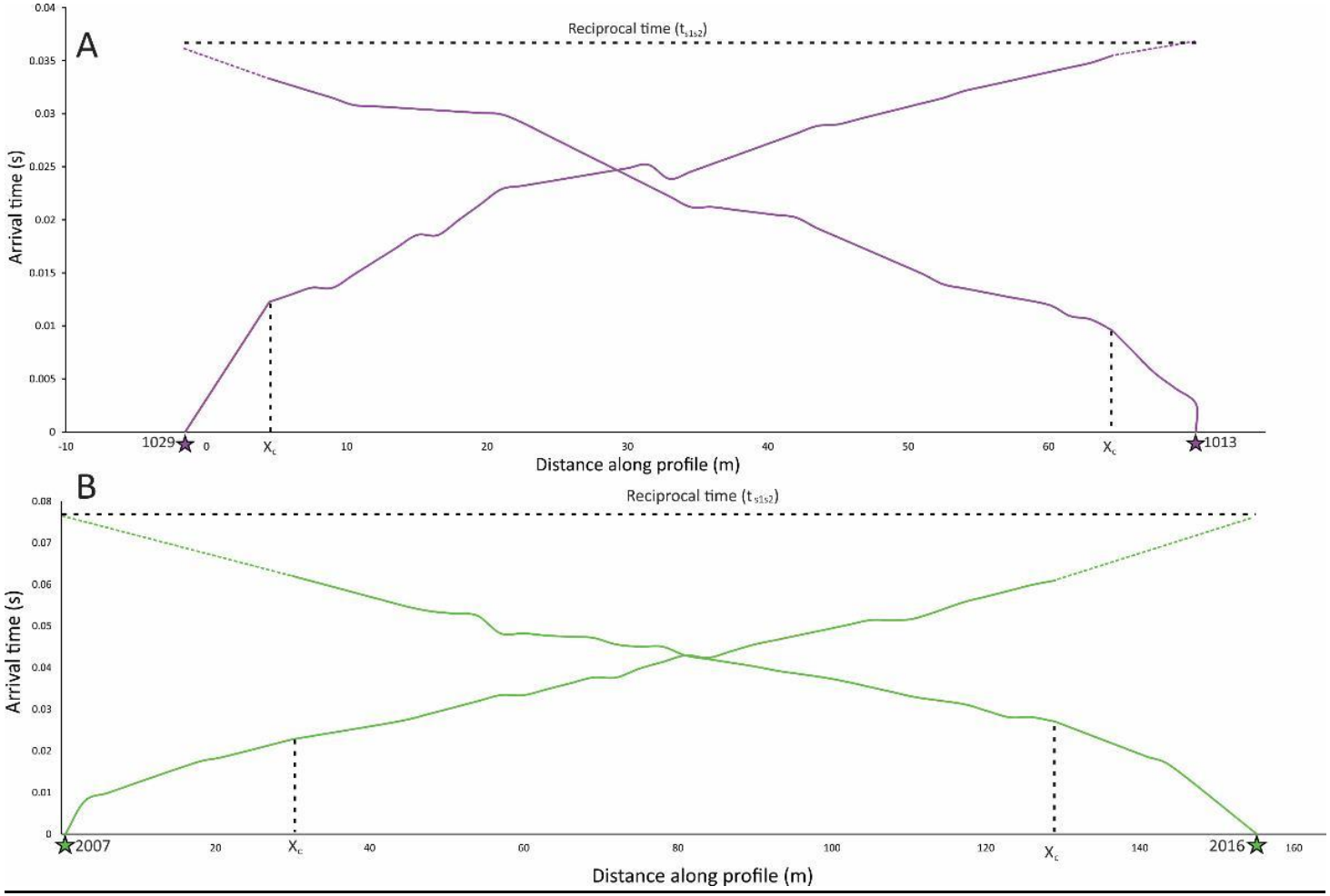

Figure 3.11 Time distance plot for Profile 1 (A) and Profile 2 (B). X_c marks the cross-over distances for each shot. Stars represent shot location.

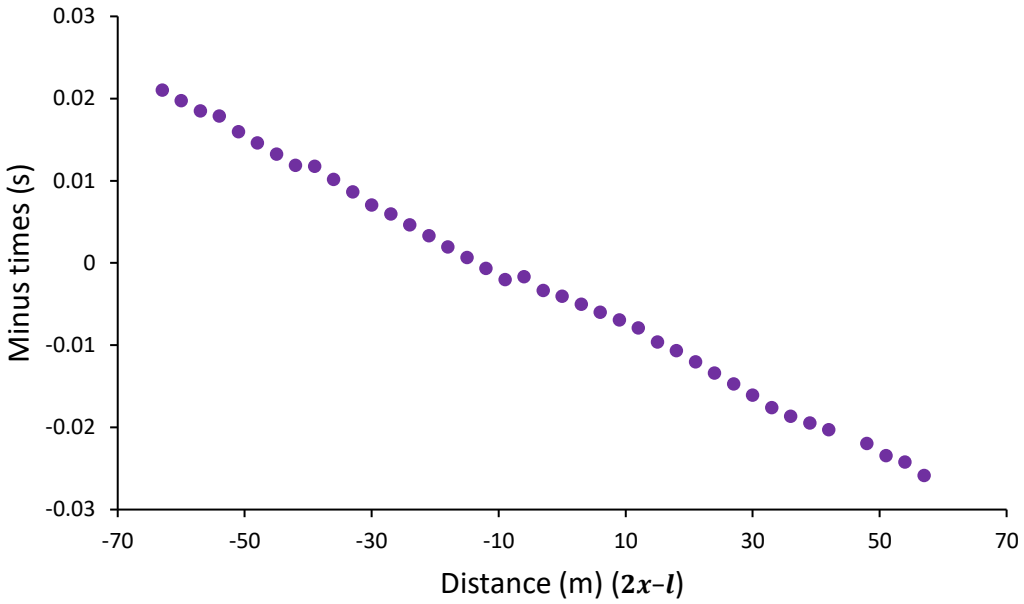

Figure 3.12 Distance vs. Minus times for Profile 1

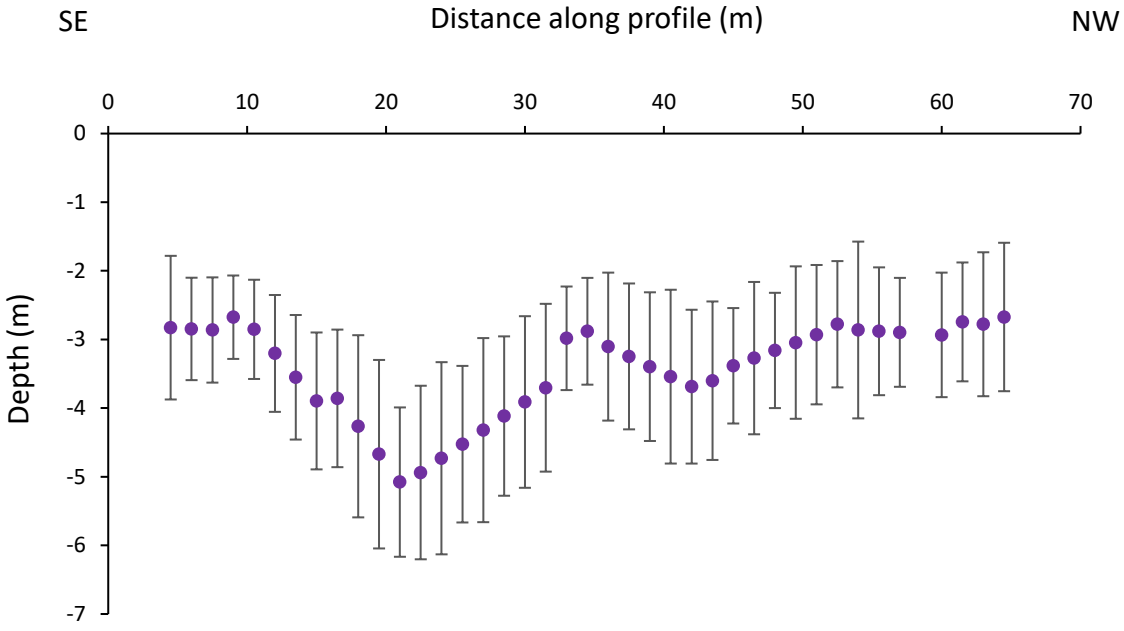

Figure 3.13 Morphology of V_1/V_2 refractor for Profile 1 using the plus-minus method

Line 2: shots 2007 and 2016

Figure 3.14 displays distance vs. minus times. As was the case for Profile 1, the data plot as a straight line, which indicates that the plus-minus method is valid. We calculate V_2 to be 2.8 ± 0.1 km s^{-1}, which is comparable to the 2.6 ± 0.1 km s^{-1} calculated for line 1, since Profile 2 is imaging deeper (due to larger geophone offset). Figure 3.15 displays the morphology of the V_1/V_2 refractor.

As with Profile 1, V_1 is variable, but in this case, it exhibits a slightly higher velocity range (1 – 1.2 km s^{-1}). This is expected as Profile 2 is imaging deeper, and defining the cut-off between V_1 and V_2 was more difficult. As with Profile 1 this is most likely sediment, potentially fluvial, that has minor lateral density variations. The V_1/V_2 refractor is undulating over 1 – 2 m with a slight decrease in depth towards the NE, and is located at a greater depth than the V_1/V_2 refractor for Profile 1, due to greater penetration depth (Figure 3.15). This refractor morphology may be due to faulting activity on the nearby Ohariu Fault.

Uncertainty:

Uncertainty in reciprocal time was estimated as 10 % of the total travel-time for each profile. Uncertainty in V_2 was calculated using the *linest* function on excel. This yielded a standard error value for V_2. Uncertainty in first break picks were estimated through a repeatability exercise. First breaks were re-picked, and the error was defined as the difference in travel-time between the original picks and the repeated picks at each geophone. The main source of uncertainty arises from the assumption that V_1 has uniform velocity, meaning that all undulations in the plus times are due to refractor geometry. However, we can see from the above information that V_1 is variable along both profiles. The standard error for each V_1 value was calculated using the *linest* function on *excel*. This yields approximately a 20 % uncertainty in V_1 for each profile. This uncertainty is, however systematic, meaning that it will affect total refractor depth, but not refractor morphology.

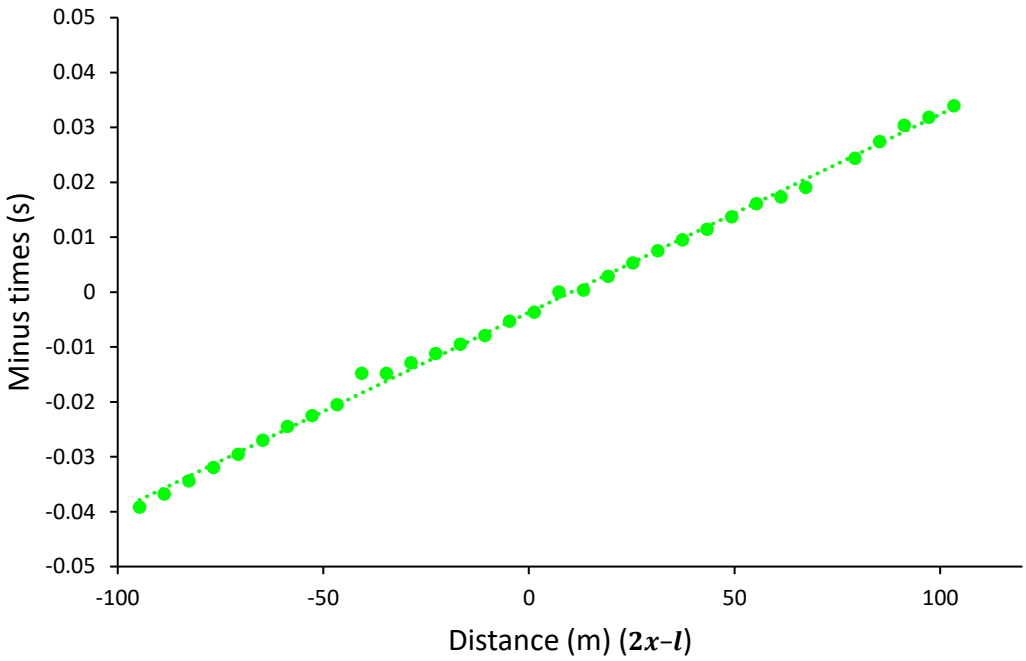

Figure 3.14 Distance vs. Minus times for Profile 2

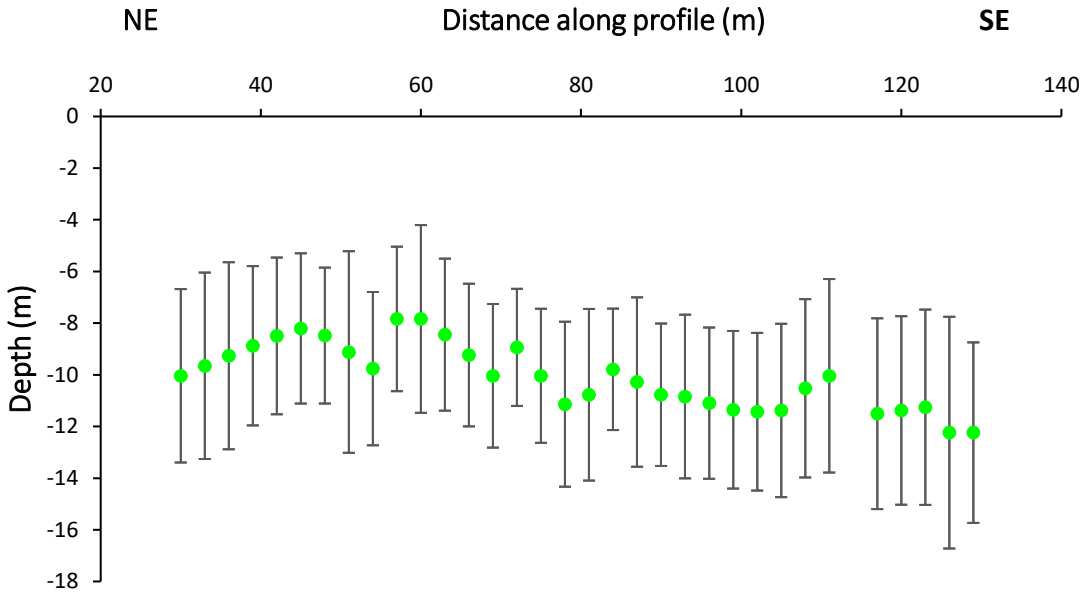

Figure 3.15 Morphology of V_1/V_2 refractor for Profile 2 using the plus-minus method

3.5.2 WHB integral

The refraction analysis from the previous section assumes iso-velocity layers. In reality, the velocity of sedimentary rocks increase with depth of burial. In this section we use a long offset shot (shot 2038) to invert for a velocity with depth function.

Figure 3.16 displays a time-distance plot for shot 2038, a far offset shot from Profile 2 located 108 m NE off the end of the array (Figure 3.7). Four points were considered outliers and were not used in the analysis. A best-fit polynomial trend-line was fit through the data; the resulting R^2 value is high (0.996), indicating that the trendline fits the data well.

The distribution of velocity with depth from the V_1/V_2 refractor for shot 2038 was calculated using the WHB integral (equation 3.21). The WHB integral was numerically solved for every fourth geophone along the array using the method described in section 3.2.2 (Appendix 3). Results suggest that the sediment underlying Makara Village at the survey location has a maximum P-wave velocity of approximately 3.2 km s^{-1} at 18 m depth below the V_1/V_2 refractor (Figure 3.17).

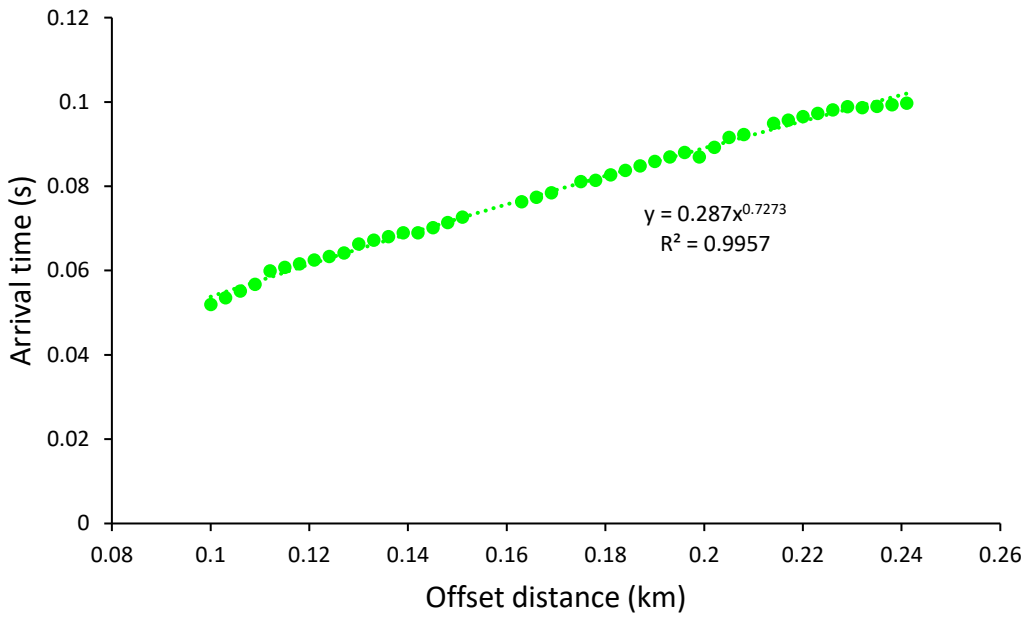

Figure 3.16 time-distance plot for shot 2038 illustrating layer V_2. A power law trendline is fit to the data, note the high R^2 value

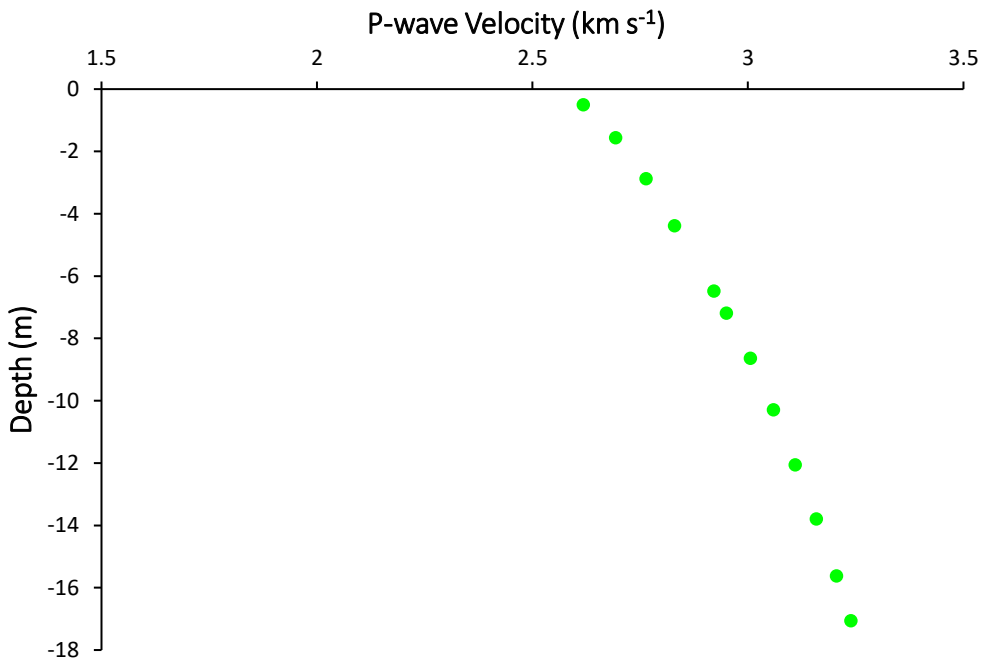

Figure 3.17 WHB integral velocity model for maximum velocity with depth. Depth is from the V_1/V_2 refractor.

3.5.3 V_p / V_s ratios

In section 3.1 we discussed how V_p/V_s ratios can be used to calculate Poisson's ratio (σ) (equation 3.5):

$$\frac{V_p}{V_s} = \left(\frac{2(1-\sigma)}{1-2\sigma}\right)^{1/2} \qquad (3.5)$$

Which in turn can be used as an indicator for lithology (Kearey et al., 2002).

V_p/V_s ratios, were calculated for a range of shots from Profiles 1 and 2 (Figure 3.18). Shot gathers analysed are displayed in Appendix 4. Using the V_p/V_s ratios, Poisson's ratio was also calculated using equation (3.5) above. This analysis yields an average V_p / V_s velocity of 3.52 km s^{-1} and an average Poisson's ratio of 0.46. These results and their implications are discussed in Chapter 7.

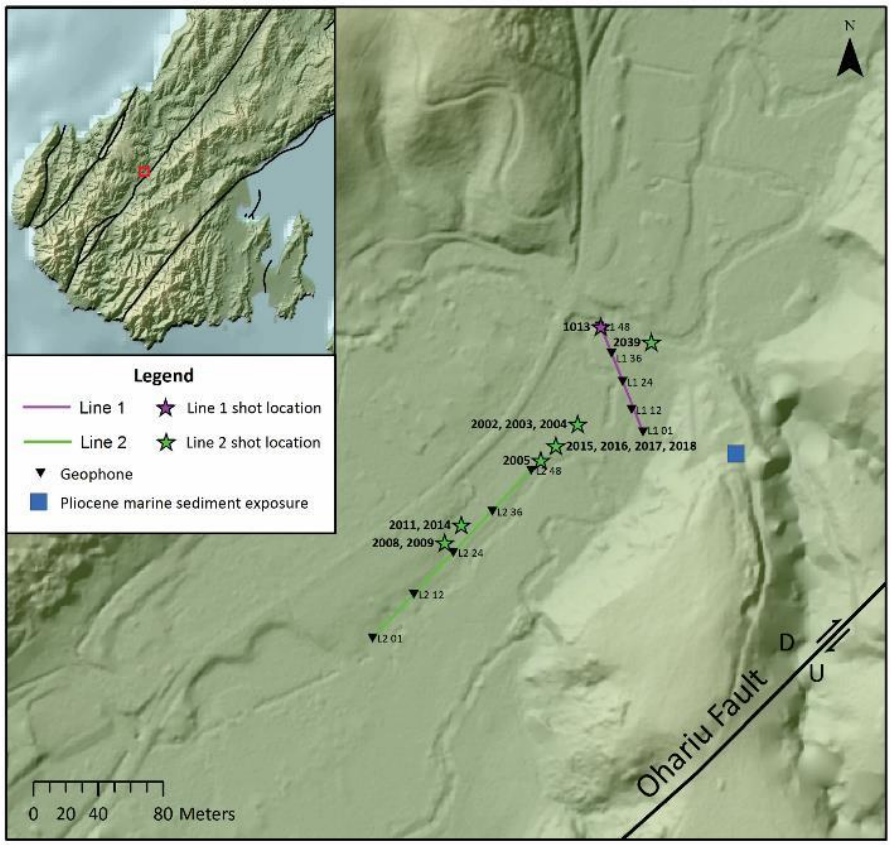

Figure 3.18 Map illustrating shot locations for V_p/V_s measurements. DEM from Landcare Research. Faults from GNS Active Faults Database

Table 3.2 V_p / V_s ratios and Poisson's ratios for selected shots. Shot locations displayed in Figure 3.18. Velocities are in km s^{-1}

Shot	**2002**	**2003**	**2004**	**2005**	**2008**	**2009**	**2011**
V_p	2.58	2.42	2.21	2.34	2.56	2.54	2.69
V_s	0.66	0.66	0.89	0.81	0.73	0.73	0.50
V_p / V_s	3.94	3.66	2.48	2.88	3.49	3.46	5.40
Poisson's ratio	0.47	0.46	0.40	0.43	0.46	0.45	0.48
Shot	**2014**	**2015**	**2016**	**2017**	**2018**	**2039**	**1013**
V_p	2.27	1.78	1.70	2.13	2.52	3.25	2.32
V_s	0.47	0.81	0.60	0.72	0.78	0.73	0.44
V_p / V_s	4.80	2.20	2.85	2.97	3.23	4.43	5.31
Poisson's ratio	0.48	0.37	0.43	0.44	0.45	0.47	0.48

4 Cosmogenic nuclide study

This chapter describes cosmic rays and cosmogenic nuclides, focussing particularly on *in situ* ^{10}Be exposure dating in quartz. This chapter also presents results from a cosmogenic nuclide study done in western Wellington.

4.1 Cosmic rays

4.1.1 Nature and origin of cosmic rays

Cosmic rays can form inside our solar system (solar cosmic rays), or outside our solar system (galactic cosmic rays). Solar cosmic rays have considerably lower energies (< 1 GeV; 1-100 MeV) compared to galactic cosmic rays (up to ~10^{20} eV), and thus, will not be considered in this study (Dunai, 2010). However, because galactic cosmic rays have much higher energies, they are able to penetrate the Earth's atmosphere and thus contribute significantly to cosmogenic nuclide production at the Earth's surface (Dunai, 2010; Gosse and Phillips, 2001; Masarik and Reedy, 1995). Galactic cosmic rays obtain their energy from supernova explosions, and mainly occur within the Milky Way Galaxy (Gosse and Phillips, 2001).

At the top of the atmosphere, cosmic rays are composed of protons (90 %), helium nuclei (~9 %), and electrons (~1 %) (Dunai, 2010). As primary cosmic rays enter the Earth's atmosphere, reactions take place with atoms in the atmosphere that produce secondary cascades through spallation reactions; these are neutron-dominated rather than proton-dominated and continue on the same trajectory as the original incoming ray. Secondary cascades make up 98 % of total nucleonic cosmic ray flux at the Earth's surface (Dunai, 2010; Masarik and Beer, 1999).

4.1.2 Cosmic ray interaction with Earth's geomagnetic field

The geomagnetic field controls primary cosmic-ray impingement on the Earth. Specifically, galactic cosmic ray particles must exceed a cut-off rigidity (momentum per unit charge) > 10 GV at the equator and > 0.6 GV at the poles in order to encroach the Earth (Dunai, 2010; Michel et al., 1996). These differing cut-off rigidity thresholds exist because cosmic rays approaching the geomagnetic equator travel perpendicular to the

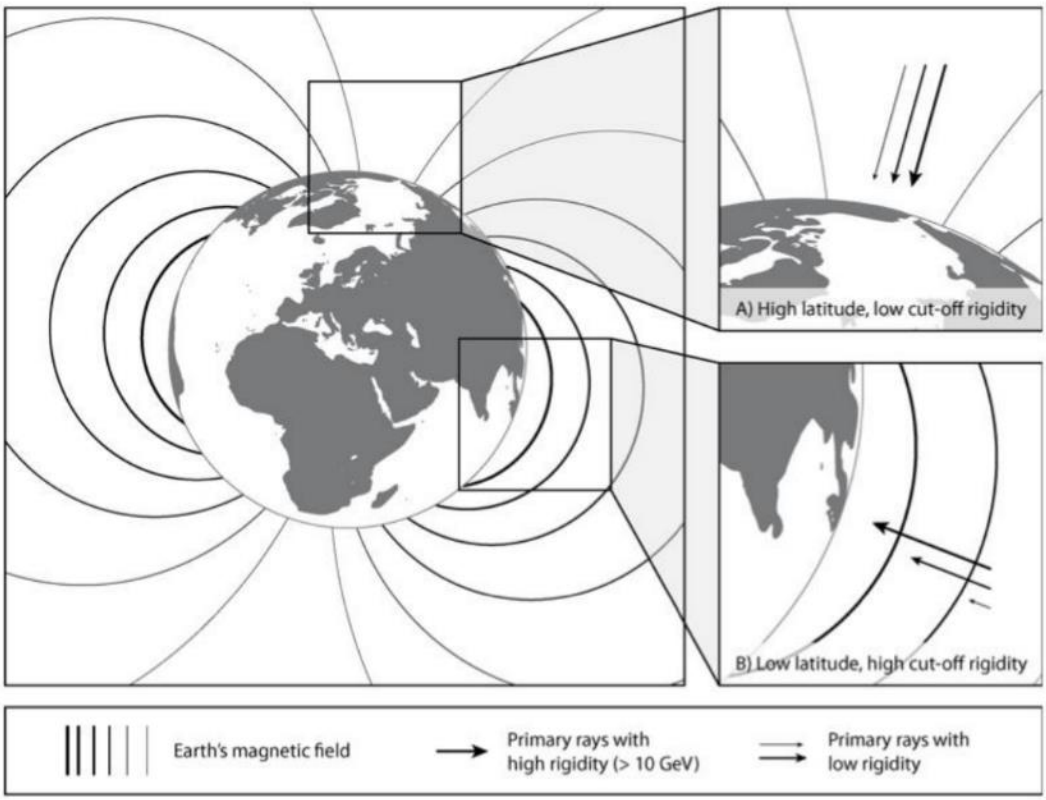

Figure 4.1 A diagram displaying Earth's magnetic field and its effect on incoming primary cosmic rays. A) shows how cosmic rays are parallel to magnetic field lines at the poles, and thus require lower cut off rigidities to impinge on the atmosphere than compared to B) where primary cosmic rays are perpendicular to magnetic field lines and thus require higher cut-off rigidities to impinge on the Earth's atmosphere. (Darvill, 2013)

geomagnetic field lines, whereas cosmic rays approaching the geomagnetic poles travel parallel to the geomagnetic field lines (Dunai, 2010) (Figure 4.1). In other words, geomagnetic field orientation and strength is higher at the equator than it is at the poles. Thus, the poles receive substantially higher cosmic ray fluxes, and therefore have higher production rates of cosmogenic nuclides compared to the equator (Figure 4.2).

4.1.3 Cosmic ray interaction with the atmosphere and solid Earth

Air pressure from the atmosphere results in cosmogenic nuclide production rate variations with altitude (Stone, 2000). Secondary cosmic rays attenuate and lose energy as they travel through the atmosphere towards the Earth's surface due to increasing air pressure (Stone, 2000). Thus, the largest cosmic ray flux occurs high up in the atmosphere, resulting in larger cosmogenic nuclide production rates at greater elevations (Figure 4.2) (Balco et al., 2008).

Cosmic ray attenuation through the solid Earth is essentially identical to that of the atmosphere (Dunai, 2010). The key differences are: 1) the higher densities of rocks, and 2) alterations in mean atomic mass and charge per nucleus (Dunai, 2010).

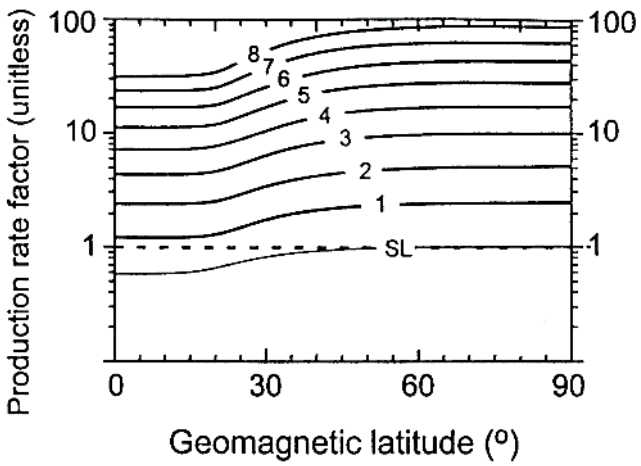

Figure 4.2 Variation of nuclide production rates with latitude and elevation above sea level. Elevation displayed as 1 Km contours. (Gosse and Phillips, 2001; Lal, 1991).

4.2 Cosmogenic nuclides

Cosmogenic nuclides are produced either in the atmosphere (meteoric nuclides) or *in situ* in rocks at the Earth's surface (*in situ* nuclides). Meteoric cosmogenic nuclides and secondary particles (such as muons and neutrons) are formed from the interactions of cosmic ray particles with the nuclei of atmospheric gases such as nitrogen and oxygen (Dunai, 2010). These secondary particles cascade towards the Earth's surface, and collide with the lithosphere, producing *in situ* cosmogenic nuclides (Dunai, 2010). *In situ* cosmogenic nuclides are used in this thesis and are discussed in more detail below.

4.2.1 In situ cosmogenic nuclides

In situ cosmogenic nuclide production decreases exponentially with depth below the Earth's surface according to the attenuation coefficient (Λ) (typically ~150 – 160 g cm^{-2}), and the density of the rock that the cosmic rays are travelling through; this is termed the absorption depth (Figure 4.3) (Dunai, 2010; Lal, 1991). In typical crustal rocks, where spallogenic reactions are the most common form of nuclide production, the spallogenic production rate decreases with depth substantially, such that the concentration of nuclides becomes negligible at ~2 – 3 m below the surface (Dunai, 2010; Lal, 1991).

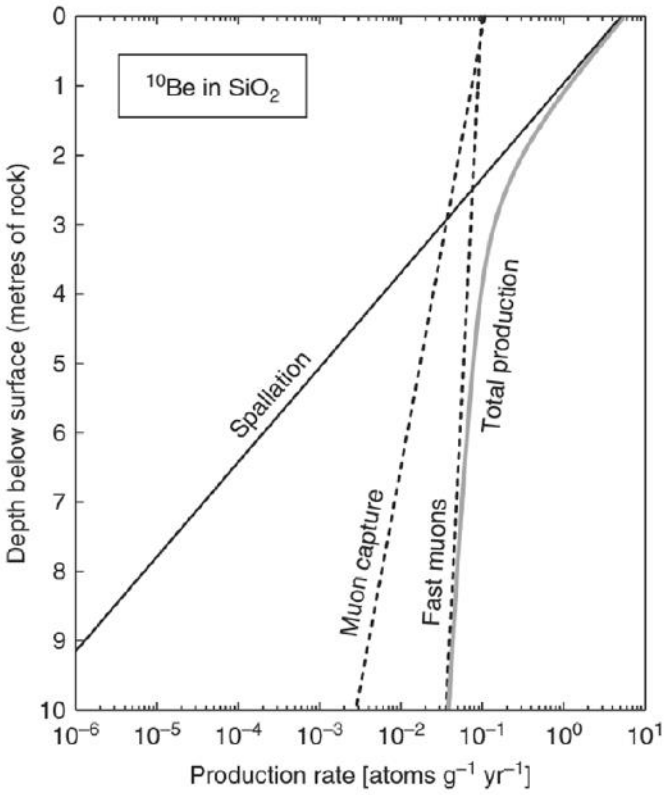

Figure 4.3 Production rate of ^{10}Be as a function of depth below the surface at high latitude and sea level using a rock density of 2.7 g cm^{-3} (Dunai, 2010).

A range of different cosmogenic nuclides are produced in the lithosphere, all of which have various rates of production. The type of nuclide produced is dependent on both the energy of the cosmic ray and the target element (Gosse and Phillips, 2001). Nuclides most commonly applied to earth sciences include: ^{3}He, ^{10}Be, ^{14}C, ^{26}Al and ^{36}Cl (Gosse and Phillips, 2001). Beryllium-10 (^{10}Be) is used in this study and thus is discussed in more detail below.

4.2.2 Beryllium-10

In situ ^{10}Be is created from O and Si within rocks, and is predominantly produced via spallation reactions (96.4%) and to a lesser extent (3.6%) via muon reactions (Gosse and Phillips, 2001). ^{10}Be is also produced in the atmosphere (meteoric ^{10}Be), where these meteoric nuclides attach themselves onto aerosols in the atmosphere and eventually reach the Earth's surface where they are absorbed onto material at the surface (Figure 4.4). (Dunai, 2010). The production rate for meteoric ^{10}Be is three orders of magnitude larger than it is for *in situ* ^{10}Be (Blard et al., 2008) and must be removed prior to measuring *in situ* ^{10}Be, as described below. ^{10}Be has a half-life of 1.387 ± 0.012 Ma (Chmeleff et al., 2010; Korschinek et al., 2010).

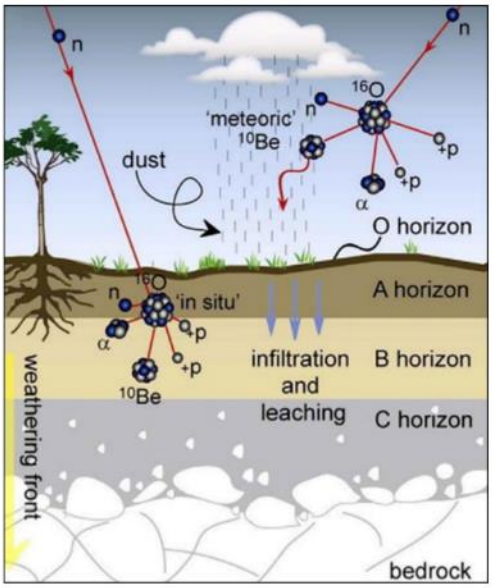

Figure 4.4 Schematic figure displaying ^{10}Be production meteoric in the atmosphere and in situ in the lithosphere. Meteoric ^{10}Be precipitates down and incorporates into rock and/or soil. (Willenbring and von Blanckenburg, 2010).

4.2.3 Exposure dating

Because cosmogenic nuclides are predominantly produced in the top few metres of the Earth's surface, they are useful in the quantification of Earth surface processes. ^{10}Be is commonly used in exposure age studies (e.g. Hidy et al., 2010; Putnam et al., 2010), erosion rate studies (e.g. Norton et al., 2008), and burial studies (e.g. Balco and Shuster, 2009).

Surface exposure dating is based on the principal that, through time, cosmogenic nuclides accumulate in rock that is exposed at the Earth's surface (Gosse and Phillips, 2001). An exposure age can be calculated from a measured nuclide concentration if the production rate is known (Gosse and Phillips, 2001). Other factors important in calculating an exposure age are shielding and inheritance.

When exposure dating with *in situ* ^{10}Be, the meteoric component must be removed as it would give an incorrect age (i.e. too old) for the surface (Dunai, 2010). The most common mineral used in ^{10}Be studies is quartz as it does not allow absorption of the meteoric component as much as other minerals (Dunai, 2010). Furthermore, quartz has a simple chemistry, and is abundant in many geological settings. Meteoric contamination from the outside of quartz grains is removed through a hydrofluoric acid leach (Kohl and Nishiizumi,

1992). The acid dissolves the outer edge of the quartz grain, leaving behind the *in situ* ^{10}Be within the crystal lattice of the quartz grain (Willenbring and von Blanckenburg, 2010).

The examination of *in situ* cosmogenic nuclide concentrations with depth are valuable for determining concurrently exposure ages, erosion rates, and inheritance values in range of geologic settings (Anderson et al., 1996; Hidy et al., 2010). Hidy et al. (2010) developed a Monte Carlo approach for modelling ^{10}Be exposure ages from vertical profiles; this program is run on Matlab™, and allows the input of site-specific geological knowledge that is then used to calculate values for exposure age, erosion rate, and inheritance while taking into account uncertainties.

Because ^{10}Be is produced from only high energy and neutron and muonic reactions (Hidy et al., 2010), the concentration C (atoms g^{-1}) for the nuclide ^{10}Be as a function of depth z (cm), exposure time t, and erosion rate ε (cm t^{-1}) can be expressed as:

$$C_{^{10}\mathrm{Be}}(z,t,\varepsilon) = \sum_i \frac{P(0)_{^{10}\mathrm{Be},i}}{\left(\frac{\varepsilon\rho_z}{\Lambda_i} + \lambda_{^{10}\mathrm{Be}}\right)} . \exp\left(-\frac{z\rho_z}{\Lambda_i}\right)$$

$$. \left[1 - \exp\left(-\mathrm{t}\left(\frac{\varepsilon\rho_z}{\Lambda_i} + \lambda_{^{10}\mathrm{Be}}\right)\right)\right] \qquad (4.1)$$

$$+ C_{inh,^{10}\mathrm{Be}} . \exp(-\lambda_{^{10}\mathrm{Be}} t)$$

Where i signifies the numerous production pathways for the nuclide ^{10}Be, $P(0)_{^{10}\mathrm{Be}}$ is production rate at the surface for nuclide m by means of the production pathway i (atoms g^{-1} a^{-1}), ρ_z is the cumulative bulk density at depth z (g cm^{-3}), $\lambda_{^{10}\mathrm{Be}}$ represents nuclide ^{10}Be's decay constant (a^{-1}), Λ_i (g cm^{-2}) is the attenuation length of the production pathway i, and $C_{inh,}$ is the inheritance of nuclide ^{10}Be (atoms g^{-1} a^{-1}) (Hidy et al., 2010). As theoretical muon production does not behave as a simple exponential with depth (Heisinger et al., 2002a; Heisinger et al., 2002b), five exponential terms are used within the profile simulator to estimate total muon production with depth (Hidy et al., 2010).

This model simulator uses a Monte Carlo approach to produce solutions to equation (4.1). The parameters available to constrain are: 1) surface production rate, 2) cumulative bulk density, 3) erosion rate and total amount of erosion, 4) exposure age, 5) inheritance, 6) neutron attenuation length, 7) muon penetration depth, and 8) shielding. Parameters 1, 2, 5, 6 and 7 can be measured or estimated, leaving parameters 3, 4 and 8 to be calculated.

The number of samples being analysed must exceed the number of parameters being calculated.

We use the method of (Hidy et al., 2010) described above to model a vertical profile of *in situ* ^{10}Be exposure ages in Mesozoic Torlesse greywacke.

4.3 Cosmogenic nuclide methods

4.3.1 Sample locality and sample collection

Seven samples were collected at the Mill Creek Wind Farm on the third ridge inland from the west coast of Wellington (Figure 4.5). The sample site is a road cut exposure on top of the K-Surface at approximately 299 m above sea level. This location was chosen as it was on one of the highest ridge tops in the surrounding area, appeared to be minimally eroded and had minimal soil/loess cover stratigraphically above the greywacke; thus allowing us to minimise the effects of shielding and weathering. A geological compass and a clinometer were used to make topographical measurements of the surrounding area relative to the sample site (Figure 4.6). Seven samples, each ~1.5-2 kg, were acquired at 50 cm intervals in 10 cm thicknesses from the top of the exposure with the use a rock hammer and a pick axe (Figure 4.7).

4.3.2 Lithology

The Wellington region is dominated by Mesozoic Torlesse greywacke of the Rakaia Terrane (Begg and Johnston, 2000). The samples for this study were collected from the Torlesse greywacke (MC15-5 – MC15-9), the Torlesse/loess interface (MC15-4) and from the soil (MC15-3). We know that loess and soil are at least partially derived from the bedrock due to the presence of Torlesse clasts in the units. Care was taken to avoid locations where the rock was extremely fine grained, as quartz grains >125 µm were required.

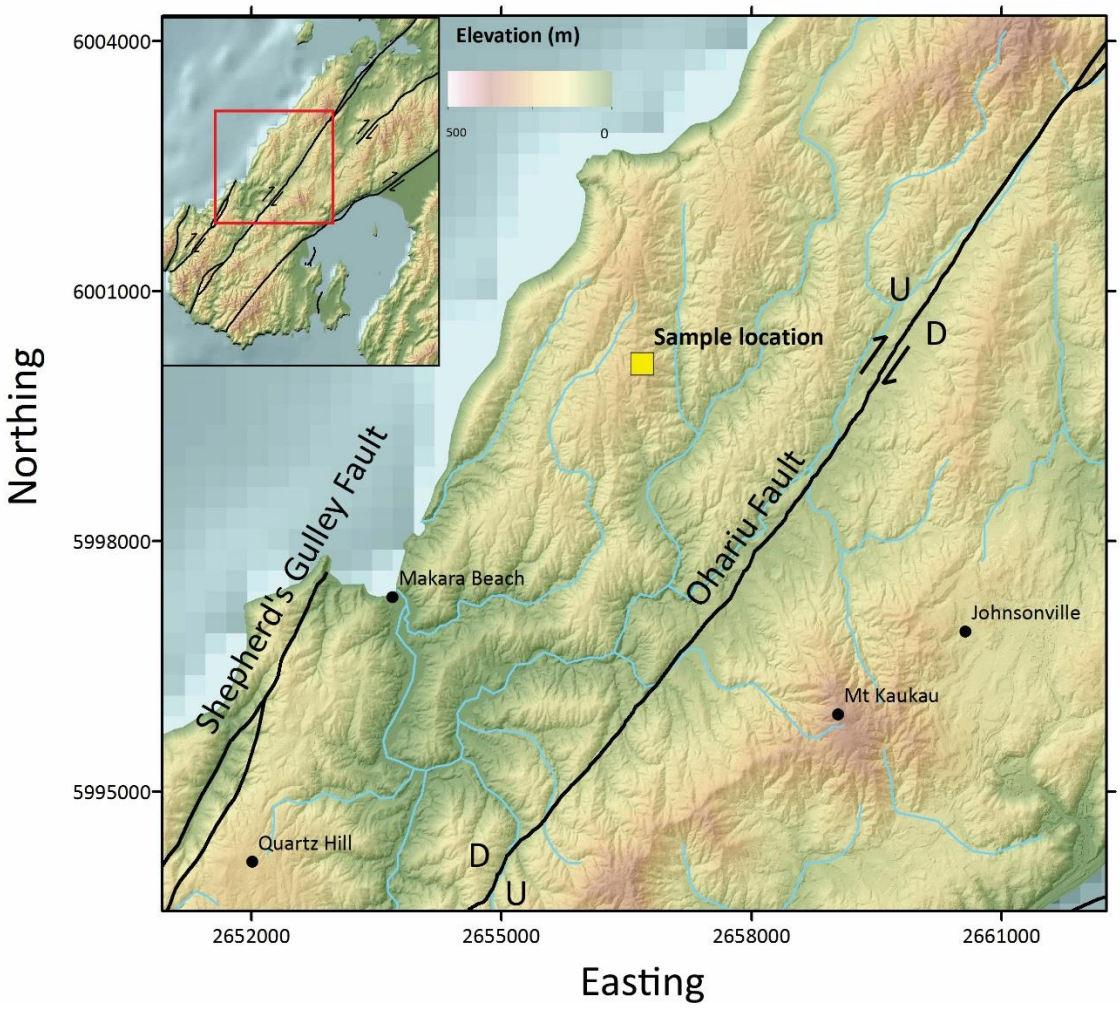

Figure 4.5 Location map for cosmogenic nuclide samples. DEM from VUW. Bathymetry from NIWA. Faults from GNS Active Faults Database.

Table 4.1 A summary of the most commonly utilised scaling schemes for production rates (Balco et al., 2008)

ID	References	Description
St	Lal (1991), Stone (2000)	Based on the latitude–altitude scaling factors of Lal (1991), as recast as functions of latitude and atmospheric pressure by Stone (2000). The scaling factor is a function of geographic latitude and atmospheric pressure. Does not take account of magnetic field variations—the nuclide production rate is constant over time
De	Desilets et al. (2006)	The scaling factor is a function of cutoff rigidity and atmospheric pressure. Production rates vary with time according to magnetic field changes
Du	Dunai (2001)	The scaling factor is a function of cutoff rigidity and atmospheric pressure. Production rates vary with time according to magnetic field changes
Li	Lifton et al. (2005)	The scaling factor is a function of cutoff rigidity, atmospheric pressure, and a solar modulation parameter. Production rates vary with time according to changes in solar output as well as changes in the Earth's magnetic field
Lm	Lal (1991), Stone (2000), Nishiizumi et al. (1989)	An adaptation of the Lal (1991) scaling scheme that accommodates paleomagnetic corrections. Production rates vary with time according to magnetic field changes. Based on the paleomagnetic correction described in Nishiizumi et al. (1989)

4.3.3 Production rates

The concentration of cosmogenic nuclides within a rock is determined by the amount of time it is exposed to cosmogenic rays, and the production rate of the nuclide within the target mineral (Cerling and Craig, 1994). Production rates of ^{10}Be in quartz range 3.9 – 5.4 atoms g^{-1} yr^{-1} at sea level high-latitude (SLHL) (Dunai, 2010). Production rate varies depending on what scaling scheme is applied (Table 4.1).

In situ cosmogenic nuclide production rates due to spallation must be standardised. This is achieved by measuring nuclide concentration at an independently dated geological calibration site that must be stable and have been constantly exposed (Balco et al., 2008). Dating techniques for the calibration site will vary depending on the type of landform being dated (e.g. wave cut surface, glacial feature etc.) (Gosse and Phillips, 2001). These local production rates are then standardised to sea level and high latitude. The production rate of ^{10}Be is well known globally. However, the majority of the calibration sites tested are located in the mid latitudes in the Northern hemisphere (e.g. Balco et al. (2008),

Putnam et al. (2010) established a production rate for ^{10}Be in quartz from an early Holocene debris flow deposit in the Southern Alps, New Zealand. The debris flow deposit was independently dated using ^{14}C in the vegetation and soils stratigraphically below the deposit (Putnam et al., 2010). Putnam et al. (2010) calculated a production rate between 3.74 and 4.15 atoms g^{-1} yr^{-1} (scaled to sea level and high latitude) depending on the scaling scheme used. This is approximately 13 % lower than production rates using the global calibration set by Balco et al. (2008), suggesting that production rates within New Zealand have in the past been overestimated. For this study we use the production rate derived by Putnam et al. (2010) using the scaling scheme 'St' (Table 4.1). This yields a sea level high latitude production rate of 3.84 g^{-1} yr^{-1}.

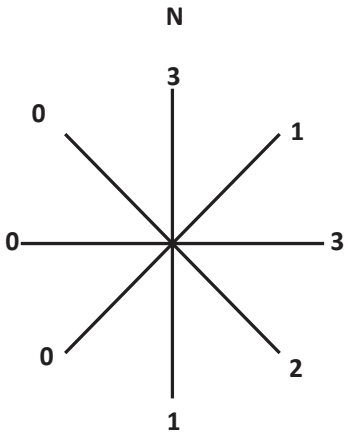

Figure 4.6 Diagram illustrating surrounding topography at Mill Creek sample site. Each number represents the angle (°) the sample site has in relation to the surrounding topography in 45° increments.

Figure 4.7 Sample localities. Samples MC15-3 and MC15-4 were obtained from the soil/loess layers. MC15-5 to MC15-9 were obtained from greywacke. Marked sample locations are approximate. (Photo by Cam Watson)

4.3.4 Laboratory procedures

Sample preparation

Each sample was put through the VUW Boyd jaw-crusher, then dry sieved at 125-500 µm in order to remove fine material less than 125 µm. Material larger than 500 µm was continuously crushed until all material was able to fit through the 500 µm sieve. Samples obtained from greywacke (MC15-5 – MC15-9), were then mixed with water in ~50 gram lots, put into the ultrasonic bath for 5-10 minutes, then wet sieved at 125 microns to get rid of the rest of the fine material stuck to the larger grains. Samples were dried overnight in the oven at 40°C. A Franz isodynamic magnetic separator was used to separate out any magnetic minerals from each sample. Each sample was put through with the machine titled at a 10 degree angle (inclination and pitch also at 10 °), with a current ranging from 0.8-1A.

Samples MC15-3 and MC15-4 were predominantly soil samples with some rock component and thus were prepared differently to the greywacke samples above. Samples MC15-3 and MC15-4 were each put into beakers in ~50 gram lots, mixed with reverse osmosis water, then decanted in order to remove light material such as organics. Next, hydrogen peroxide was added to each sample until fully submerged, then stirred every ten minutes for the first hour, then left overnight. This dissolved the organic material not removed through decanting. Once each sample was finished reacting, the centrifuge was used to separate liquid from solid. Each sample was centrifuged for 10 minutes at 4700 RPM three times, or until the liquid in each centrifuge bottle was translucent. Each sample was then dried overnight in the oven at 40°C. Sample MC15-3 was discarded as it was too fine grained.

Quartz separation and chemistry

Quartz separation and *in situ* ^{10}Be chemistry was done in the VUW cosmogenics lab following the method supplied in Appendix 5. Samples were sent to the National Isotope Centre (GNS) where they were measured using the 0.5 MeV XCAMS Accelerator Mass Spectrometer.

4.3.5 Sample concentrations

Details of samples and sample concentrations are displayed in Table 4.2. The long-term $^{10}Be/^{9}Be$ blank correction average was 5.179 ± 2.89 X 10^{-15} (1 σ). $^{10}Be/^{9}Be$ ratios were normalised with Nishiizumi et al. (2007)'s "01-5-4" standard at GNS Science.

4.4 Modelling

The method of (Hidy et al., 2010) described above in subsection 4.2.3 is used to model the vertical profile of *in situ* ^{10}Be exposure ages in Mesozoic Torlesse greywacke to determine a minimum age for the latest exposure of the greywacke above sea level, and hence, a minimum age for the K Surface.

Figure 4.8 displays a screenshot of the input model parameters for this study. The constraints we apply to the model (subsection 4.2.3) are explained in more detail below:

1) Site production rate:

   We use the SLHL production rate derived by Putnam et al. (2010) using the scaling scheme 'St' by Stone (2000), after Lal (1991) (Table 4.1). We take into account 2.5 % uncertainty as recommended by Putnam et al. (2010). This yields a site production rate of 4.79 ± 0.11 g^{-1} yr^{-1}.

2) Cumulative bulk density:

   The density of Torlesse greywacke is 2.67 g cm^{-3} (Hatherton and Leopard, 1964). However, this density probably an over estimation as the Torlesse greywacke sampled is heavily weathered and fractured. Therefore, we keep the density constant with depth, but allow it to vary randomly between 2.3 and 2.67 g cm^{-3}.

3) Erosion rate and total erosion:

   Erosion rate and total erosion values are unknown and thus were allowed to vary between 0 – 5 cm ka^{-1} and 10 m respectively.

4) Exposure age:

   The exposure age was allowed to vary anywhere between 5.3 and 0 Ma, as this is the current age constraint for the K Surface (Begg and Johnston, 2000; Cotton, 1957).

Table 4.2 Sample concentrations and locations, gathered from K Surface top (Figure 4.5).

Sample ID	Latitude	Longitude	Elevation (m asl)	Lab ID	Final quartz weight (g)	9Be carrier (mg)	10Be/9Be	Error (%)	10Be sample conc. (atoms/g)	10Be sample conc. error (atoms/g)	Shielding correction
MC15-4	-41.1941	174.7488	298.5	CW1	8.55	0.3653	2.81804E-14	9.4	65676.531	11182.274	0.99999
MC15-5	-41.1941	174.7488	298	CW2	58.33	0.3655	1.63915E-13	3.5	66458.467	2695.654	0.99999
MC15-6	-41.1941	174.7488	297.5	CW3	30.91	0.3661	5.90191E-14	5.6	42609.541	3474.502	0.99999
MC15-7	-41.1941	174.7488	297	CW4	58.10	0.3674	7.51695E-14	6.4	29576.327	2383.374	0.99999
MC15-8	-41.1941	174.7488	296.5	CW5	52.33	0.3665	6.08064E-14	5.7	26032.601	2108.962	0.99999
MC15-9	-41.1941	174.7488	296	CW6	52.38	0.3656	5.18452E-14	6.1	21766.280	1991.238	0.99999

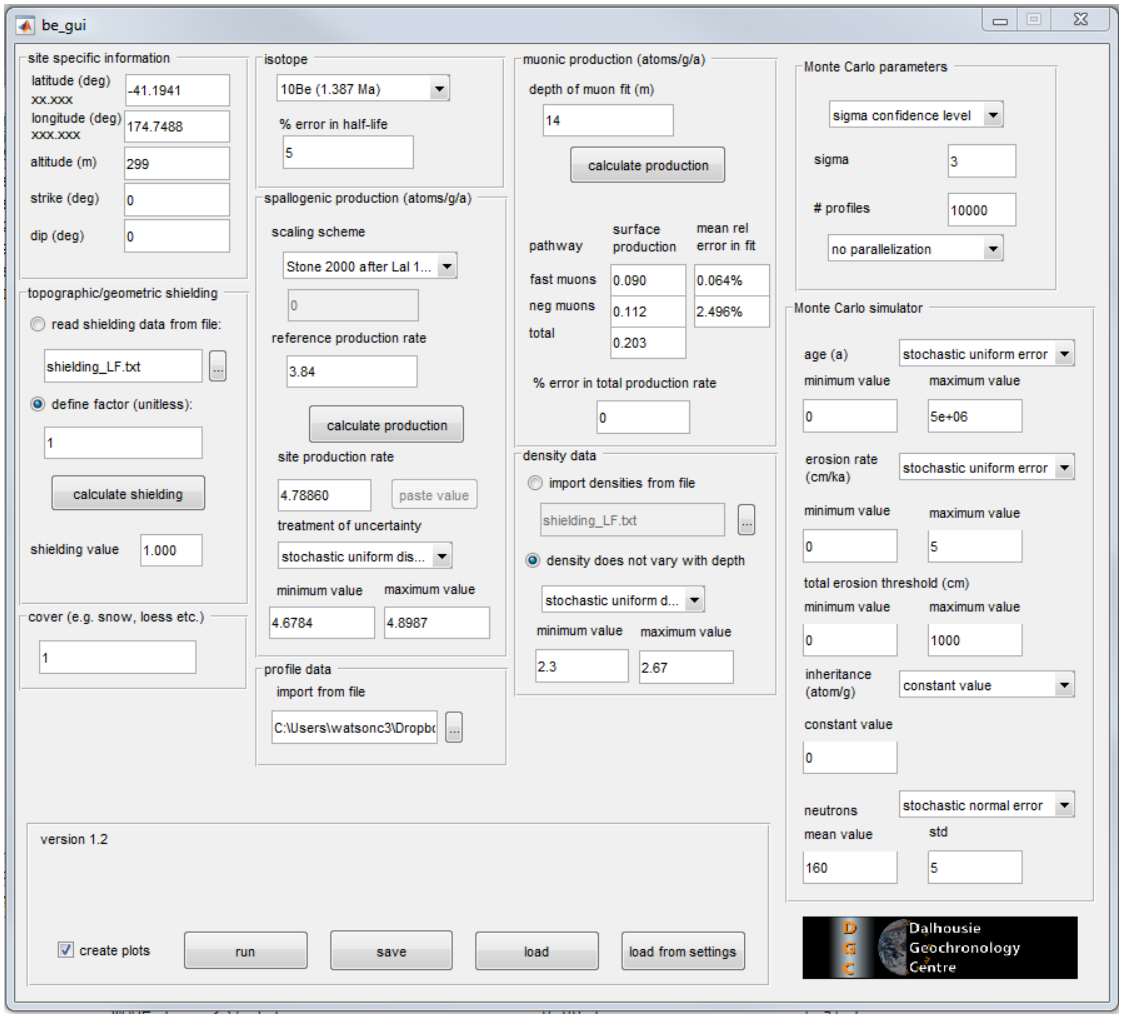

Figure 4.8 A screenshot of the input parameters for modelling

5) Inheritance:

Although the Torlesse greywacke is Mesozoic aged, we are dating the last time it (the K Surface) was exposed at Earth's surface; therefore, it is important to consider previous uplift/exposure events. Since the last uplift event occurred during the Late Miocene (Figure 1.6), and ^{10}Be has a half-life of 1.387 ± 0.012 Ma (Chmeleff et al., 2010; Korschinek et al., 2010), we set inheritance to zero.

6) Neutron attenuation length:

A normally distributed mean value of 160 g cm^{-2} with a 5 % standard error was used as the neutron attenuation length (Hidy et al., 2010; Lal, 1991).

7) Muogenic surface production:

   The depth range for muon production was set to 14 m as this is more than the sum of the total allowed threshold for erosion and the sample depth (Hidy et al., 2010). This yielded a local total muogenic surface production rate of 0.202 atoms g^{-1} a^{-1}.

8) Shielding:

   Shielding is considered negligible due to the sample site being high to the surrounding topography and a lack of coverbed stratigraphy on top of the greywacke (Figure 4.6).

4.5 Results

The ^{10}Be data for the five Torlesse greywacke samples and the one Torlesse/loess interface sample were modelled using the constraints described above in section 4.4. Ten thousand solutions were input into the Monte Carlo simulator. No solution existed for the 95% confidence interval window (2 σ), so this was increased to the 99.7 % confidence window (3 σ). This specifies that 99.7 % of the data are within three standard deviations of the mean. The measured concentrations for the vertical profile produce a theoretical exponential distribution with depth in accordance with equation 4.1 (Figure 4.9). The shallowest sample has greater error in its value, and the best fit line only just fits within error. An explanation for this could be due to this sample being collected from the Torlesse/loess interface; some of the sediment could have been transported after initial exposure, resulting in a lower concentration. Analysis of the six sample profile yields most probable values of $238.1^{+149.3}_{-141.7}$ ka and $1.79^{+0.59}_{-0.83}$ cm ka $^{-1}$ for age and erosion rate respectively (Figure 4.10). The maximum and minimum values represent confidence limits to 2 σ.

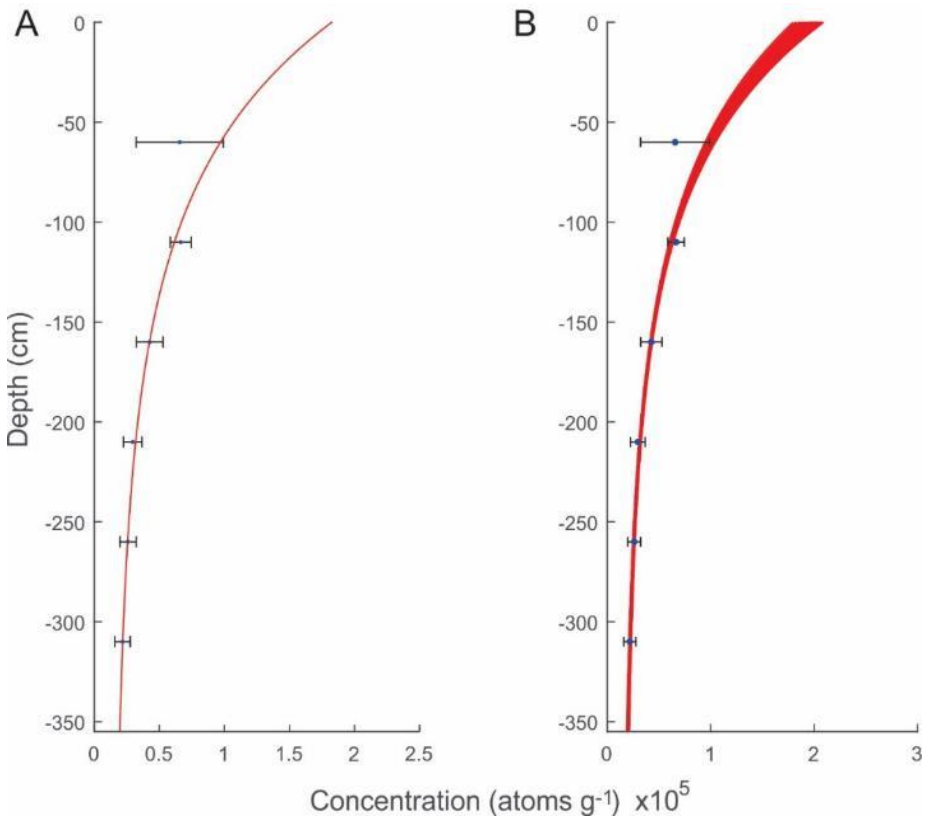

Figure 4.9 ^{10}Be concentration (atoms g^{-1}) x 10^5 vs. depth (cm) plots. A is the best fit line, and B displays the uncertainty to 3 σ for 10 000 iterations. Error bars represent 2 σ total measurement error.

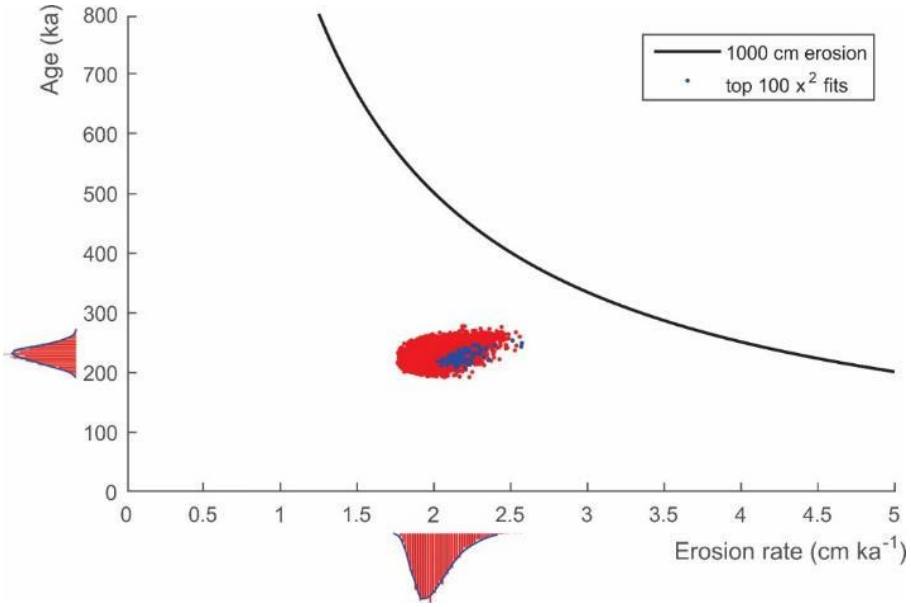

Figure 4.10 Erosion rate vs. age. The blue curves next to the X and Y axes display the normal distribution curves for erosion rates (cm ka $^{-1}$) and age (ka) respectively. The red bars are frequency.

5 Topographic analysis of the K Surface

This chapter describes the topographic analysis of the K Surface using spatial analysis techniques in Esri's ArcGIS ArcMap version 10.2 and a 1 m resolution DEM provided by the Wellington Regional Council and Landcare Research. The main objectives of this chapter are to 1) produce a map of K Surface remnants, and 2) interpolate a broad surface over K Surface remnants in preparation for flexural modelling, discussed in Chapter 7.

5.1 Working environment

New Zealand Transverse Mercator 2000 (NZTM) was used as the projection system. Layers with a different projection system were changed to NZTM either manually, or on the fly automatically through ArcMap. The default raster cell size was set to 5 m, as this was the resolution of the smoothed DEM used for analysis. This allowed us to later join raster layers together using the raster calculator tool, which requires identical cell size and projection system so the cells line up correctly when calculations are made.

5.2 The mapping and definition of the K Surface

Model thresholds:

Areas of the DEM to be defined as part of the K Surface must be within all of the following thresholds. Justification for these thresholds are explained below:

1) Slope of less than 25°

25° was chosen in order to pick out areas of the K Surface that have potentially been tilted by tectonic processes.

2) Profile curvature value between -5 and 5

A small window of curvature was chosen in order to help distinguish between areas of titled K Surface and regular hillslopes.

3) 120 m linear distance away from any river or stream

In order to avoid picking up fluvial terraces. Also, since the K Surface remnants are on hilltops, it makes sense to buffer streams and rivers.

4) 130 m or more above sea level

Marine terraces correlated to past interglacial highstands on the south coast of Wellington and profile heights of the K Surface constrain the height above sea level value (Begg et al., 2008; Begg and Johnston, 2000).

5) Remnants must have an area of at least 0.1 km^2

This values was chosen in order to remove areas left at the end of the process sequence that were located on hillslopes and/or too small to be considered a K Surface remnant. A threshold value of 0.1 km^2 was chosen as areas any smaller could represent something else (i.e. could not be definitively assigned to the K Surface).

Mapping:

The reader should refer to the processing flow chart in Appendix 6 when reading the following subsection.

We were unable to run analyses on the full DEM due to its sheer size. Therefore, it was divided up into overlapping segments. To reduce processing time, an automated processing workflow was built (using ModelBuilder) to satisfy the model thresholds 1 – 3. Once a "Ksurface_model" file was created for each segment, all segments were combined to create one raster file ("K_Surface_initial"). "K_Surface_initial" was then used to further analyse manually for thresholds 4 and 5.

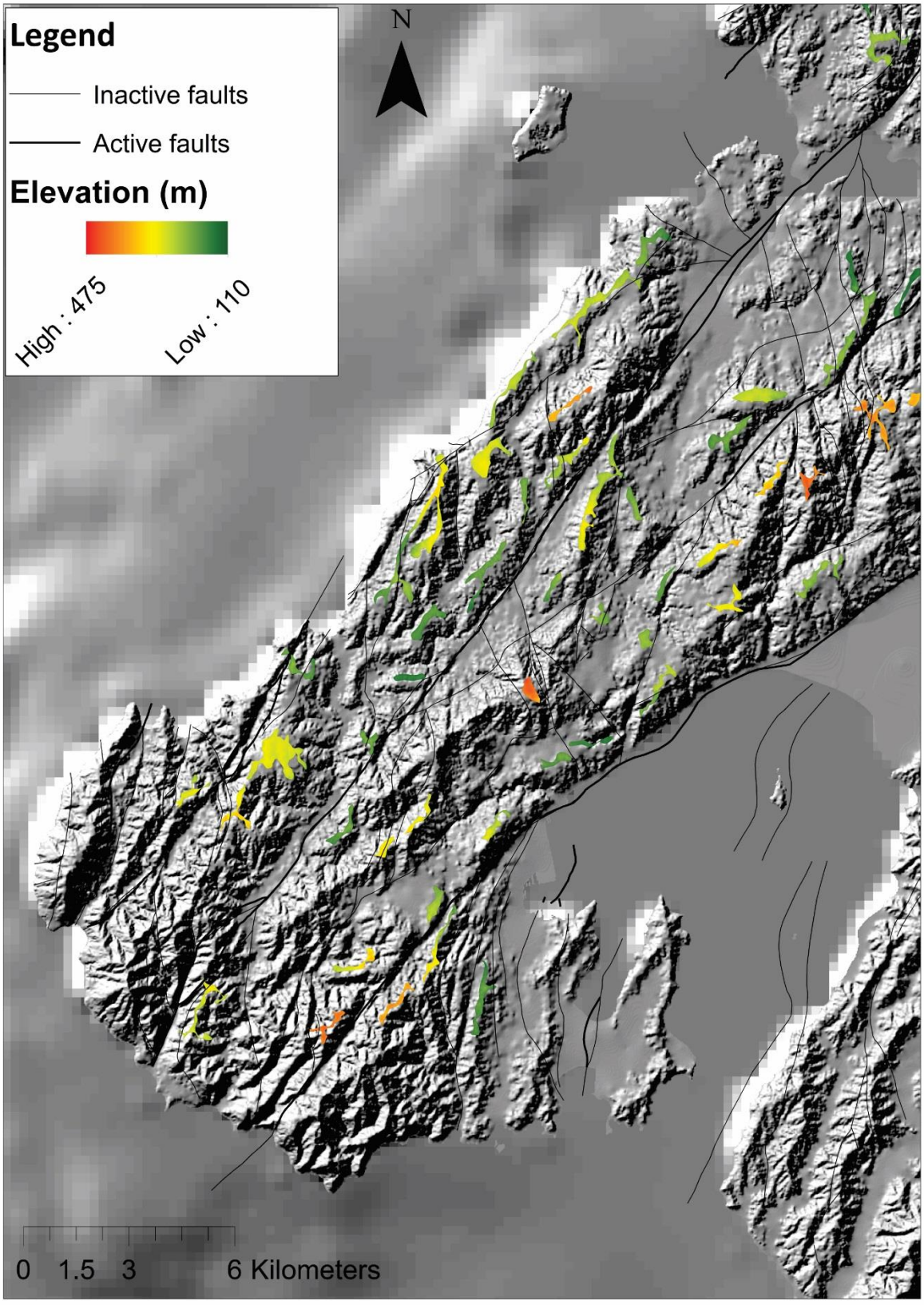

Figure 5.1 Calculated K Surface remnants displaying elevation distribution. DEM from VUW. Bathymetry from NIWA. Faults from GNS Active Faults Database.

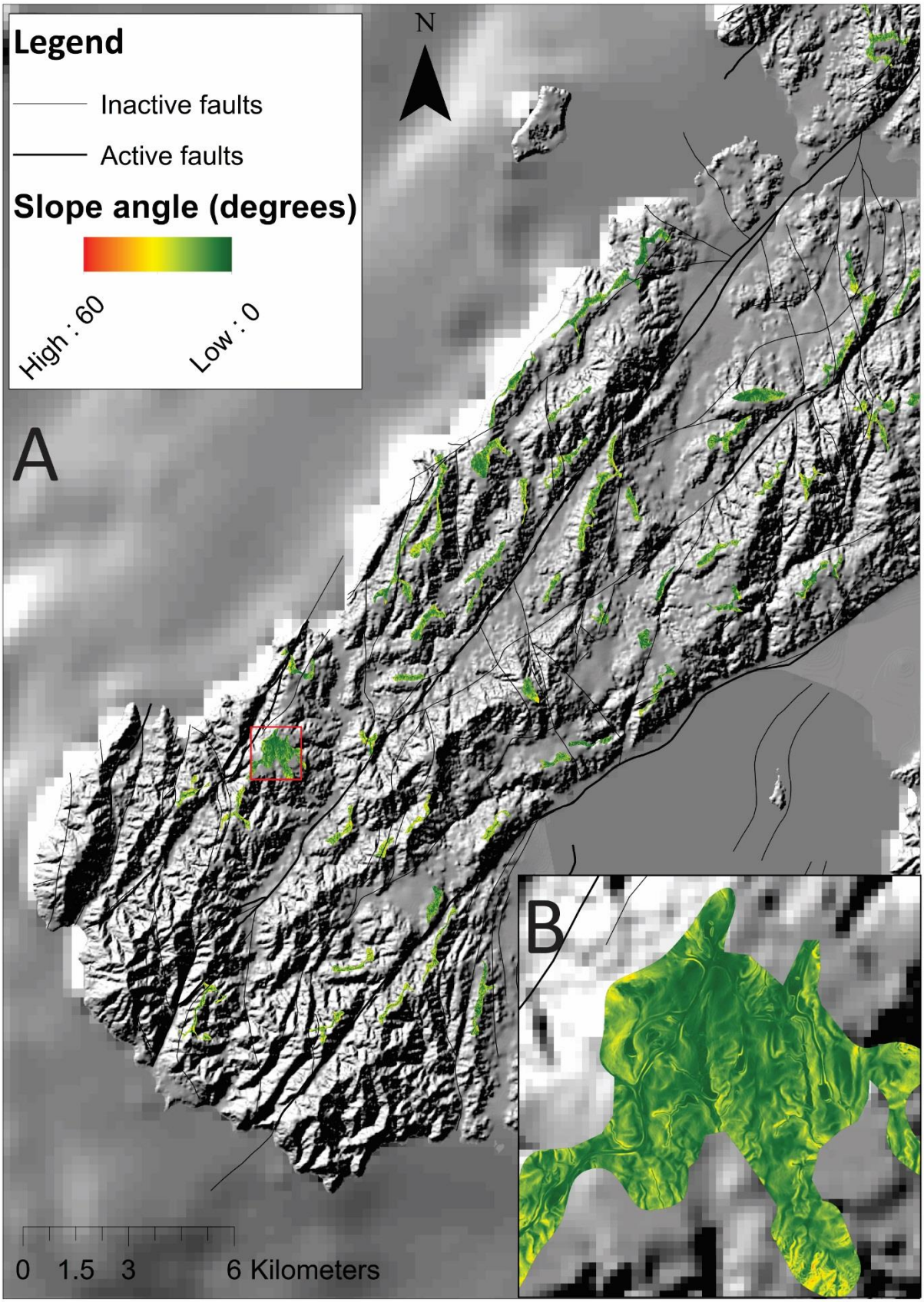

Figure 5.2 Slope (°) distribution for calculated K Surface remnants, (A) whole K Surface, (B) zoomed in on Quartz Hill. DEM from VUW. Bathymetry from NIWA. Faults from GNS Active Faults Database.

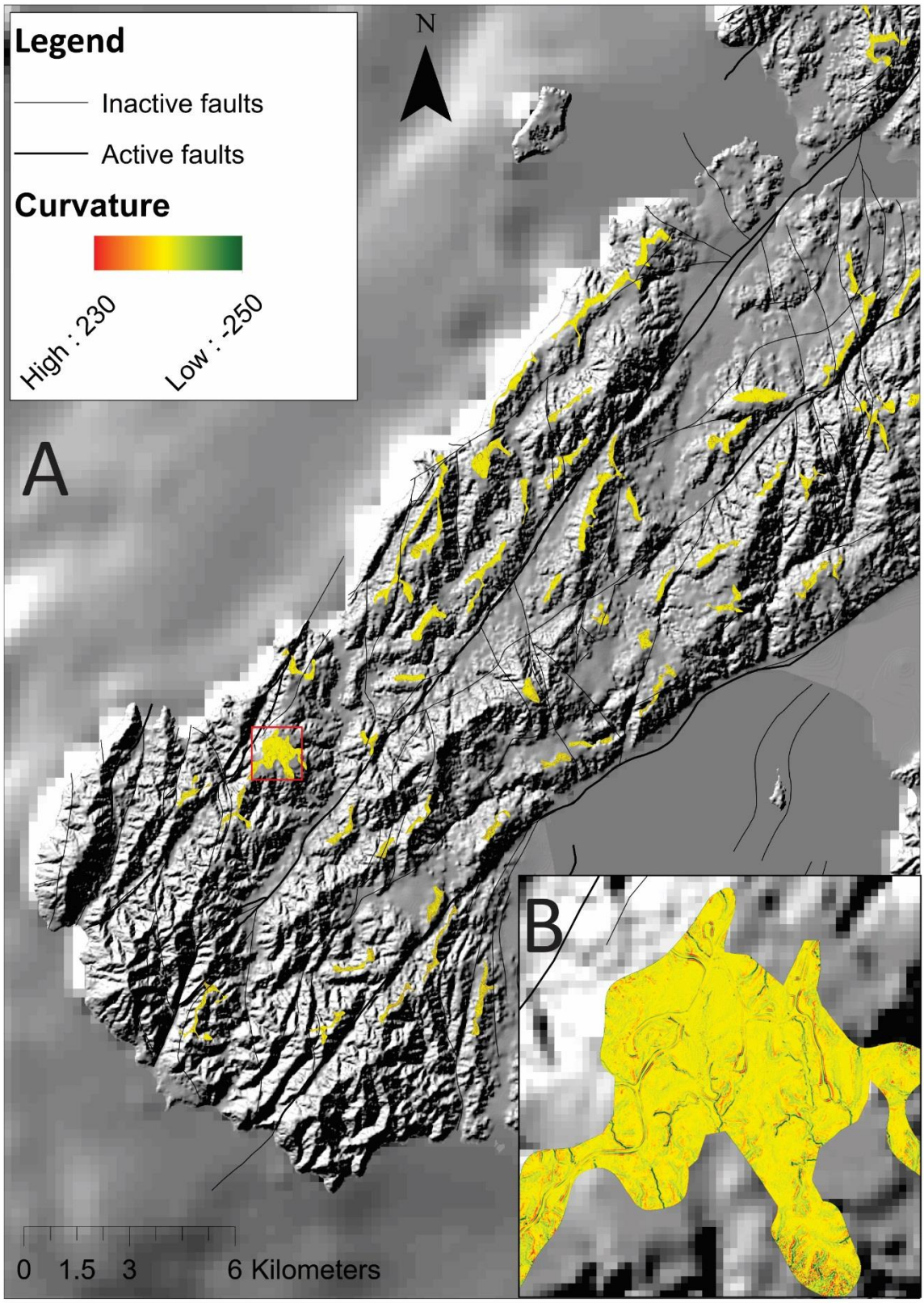

Figure 5.3 Curvature distribution for K Surface remnants, (A) whole K Surface, (B) zoomed in on Quartz Hill. DEM from VUW. Bathymetry from NIWA. Faults from GNS Active Faults Database.

Based on our thresholds, we ended up with seventy-seven remnants. Figure 5.1 displays modelled K Surface remnants and their associated elevation distribution. Figure 5.2 and Figure 5.3 display slope and curvature distribution, respectively. As we can see, the lower and upper values for slope and curvature do, in some places, exceed our original thresholds defined in the previous section (Figure 5.2B and Figure 5.3B). This is due to our final step being to aggregate points within 100 m of each other into polygons, which would have incorporated parts of the DEM where slope and curvature values are higher than our thresholds (Appendix 6). This is probably ok, because these above threshold values are sparse and generally are associated with small-scale features such as road cuttings (e.g. Figure 5.3B).

5.3 K Surface interpolation

Interpolation of the K Surface was done using the diffusion kernel (DK) interpolator, a module within the Geostatistical Wizard in ArcGIS. The diffusion interpolator is based on the fundamental solution of the heat equation, which describes how particles diffuse in a homogenous medium with time. The DK interpolator was used in favour of kriging, inverse distance weighted (IDW) or spline because: 1) it allows input of barriers, 2) it produces RMS error, 3) It allows values to gently flow around points (important as we want to model a broad surface). Two sets of models were produced, one with faults input as barriers, and one with no input barriers. A search bandwidth of 500 m was applied the interpolator. A 10 % subset of the K Surface point data ("Ksurface_points_130_subset") was input to interpolate each surface. The full K Surface point dataset ("Ksurface_points_value_130m") was then used to calculate the uncertainty between the measured and interpolated values.

Results for the interpolations with barriers and without barriers are displayed in Figure 5.4 and Figure 5.5 respectively. We can see that the average topographic elevation increases drastically towards the northern extent of each interpolated surface. This is because we are encroaching on the Tararua Ranges, which is an area subject to different tectonic mechanisms compared to western Wellington (i.e. sediment underplating) (Henrys et al., 2013; Walcott, 1987).

Uncertainty between interpolated values and measured values were attained automatically by the Geostatistical Wizard in ArcGIS (Appendix 7). Root Mean Square (RMS) error values for the "with barriers" and "without barriers" interpolations are 9.4 m and 14.1 m, respectively. These values are acceptable for our analysis, as they do not differ

hugely to the original elevation values. Furthermore, these values suggest that barriers (i.e. the faults), albeit nominally, improve the fit.

5.4 K Surface extent

K Surface extent is defined by the following:

1) The northern extent is defined by the beginning of the Tararua Ranges due to their distinctly different morphology, and therefore likely different uplift mechanism (sediment underplating) (Henrys et al., 2013; Walcott, 1987).
2) The eastern extent is characterised by the start of the Rimutaka Ranges due to their formation being a result of (partial) sediment underplating (Henrys et al., 2013; Walcott, 1987). Furthermore, the terrain lacks the broad, flat surfaces that characterise western Wellington.
3) The southern extent is defined by an increase in average elevation a few hundred metres south of Quartz Hill. This is seen in the final K Surface map where very few remnants are picked up by the model in the very southward extent Wellington (Figure 5.1).

5.5 Profile for flexural modelling

Using the thresholds described above in subsection 5.4, we model K Surface extent (Figure 5.6) with one profile perpendicular to the strike of the Hikurangi Margin. We use the no-barrier interpolated model (Figure 5.5) for flexural modelling because we aim to model broad surface uplift. Flexural modelling results are discussed in Chapter 7 and the methodology for the modelling is recorded in Appendix 8.

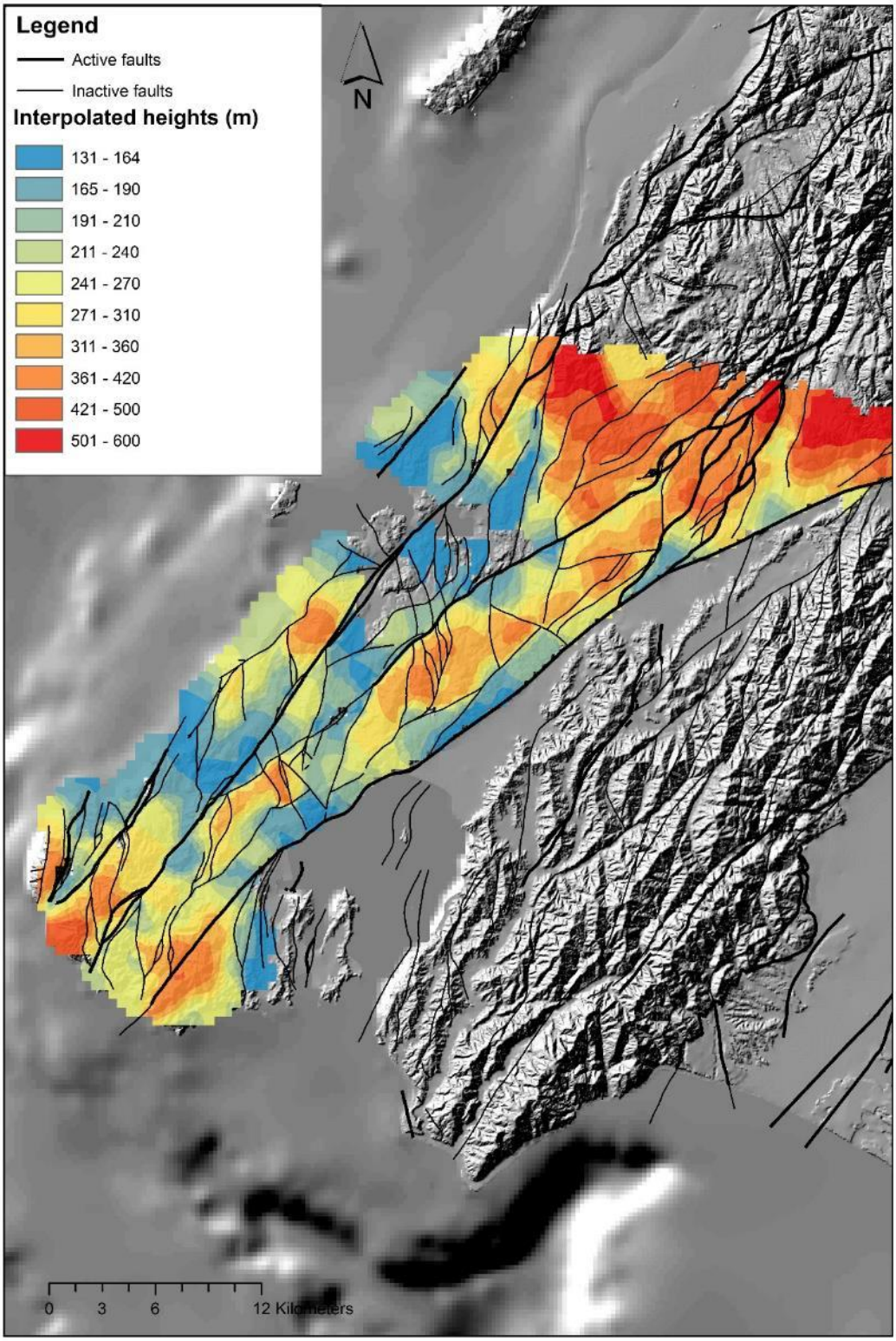

Figure 5.4 Interpolated K Surface heights with barriers. DEM from VUW. Bathymetry from NIWA. Faults from GNS Active Faults Database.

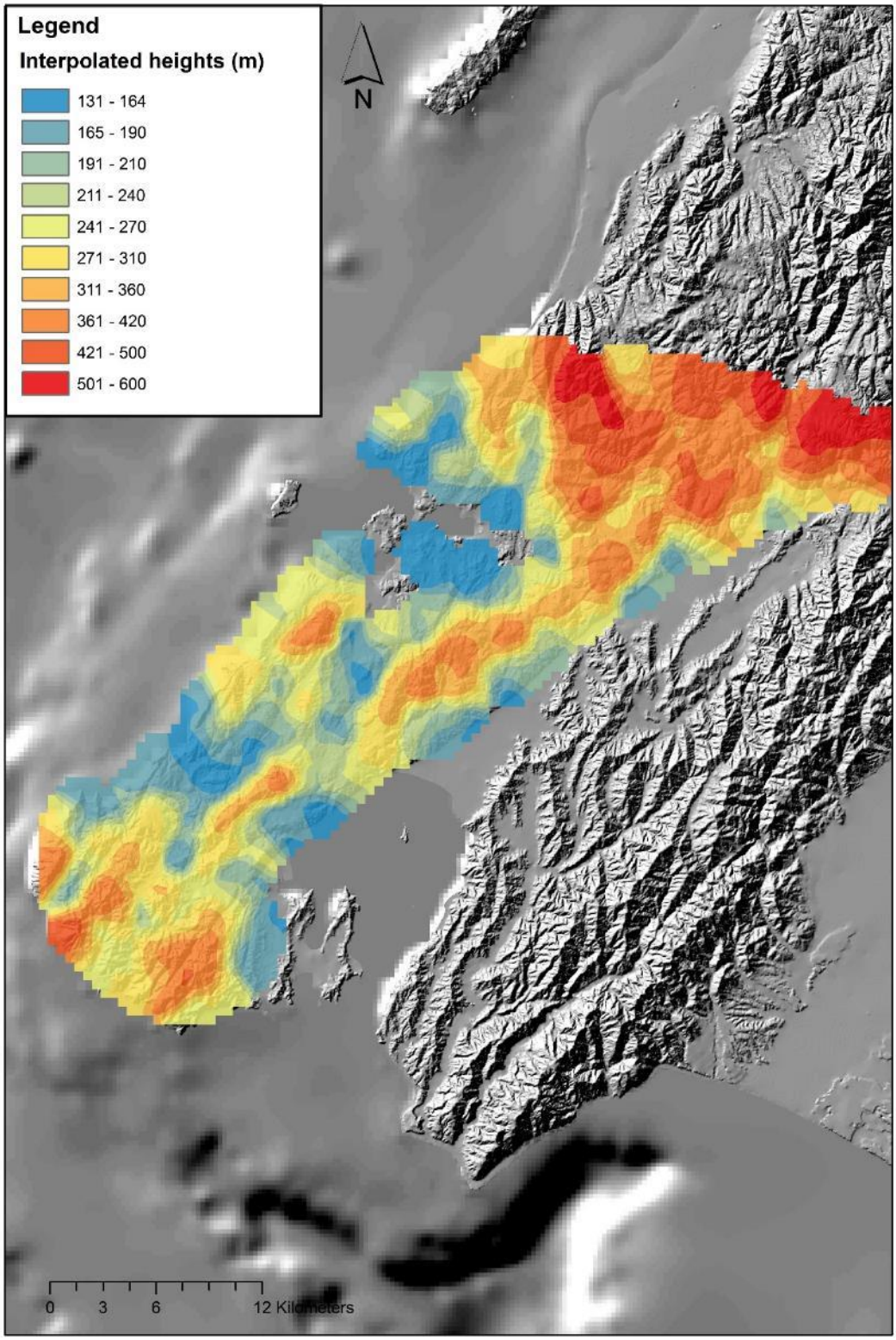

Figure 5.5 Interpolated K Surface heights without barriers. DEM from VUW. Bathymetry from NIWA.

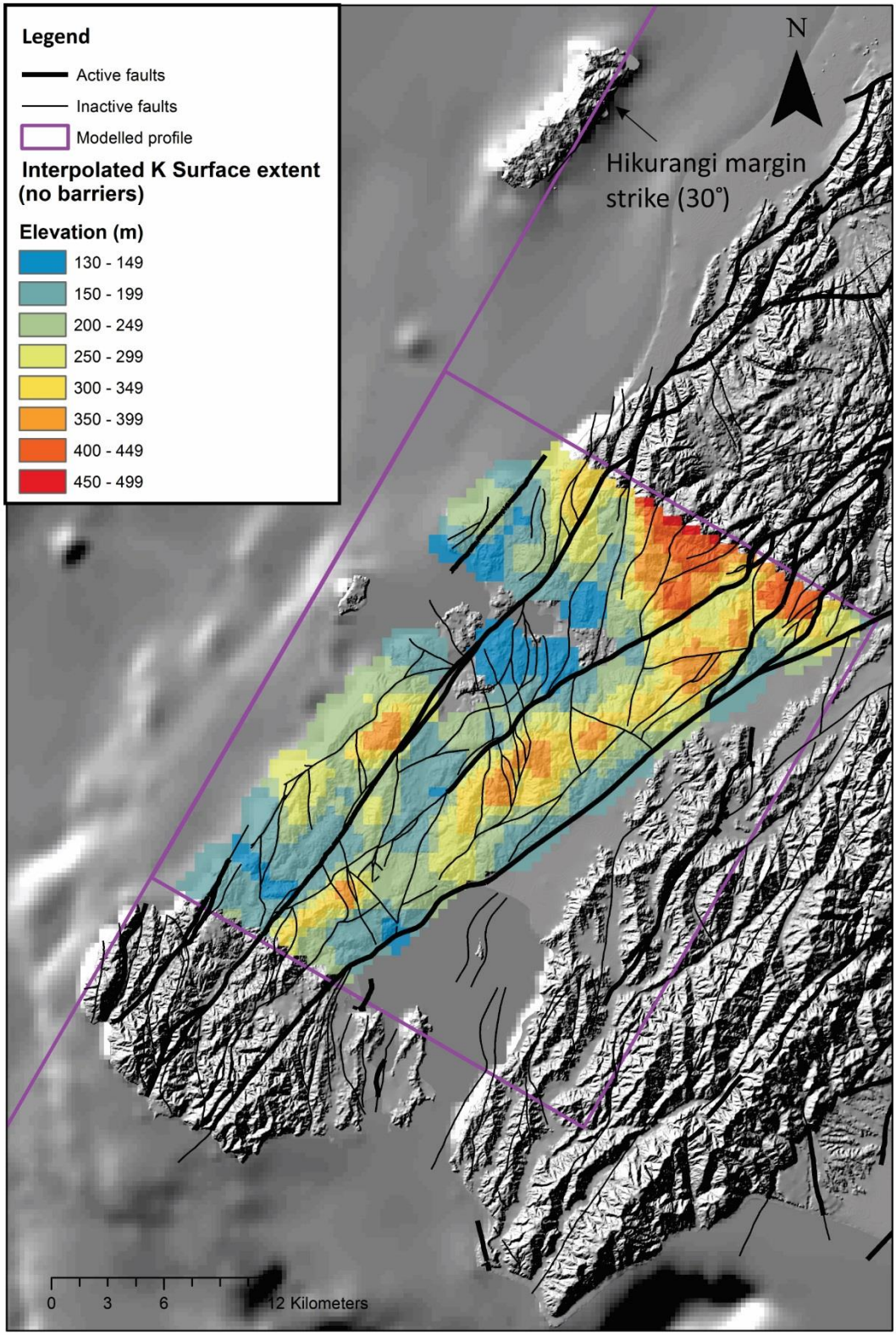

Figure 5.6 Profile used for flexural modelling. DEM from VUW. Bathymetry from NIWA. Faults from GNS Active Faults Database.

6 Rock uplift, surface uplift and exhumation of western Wellington

This chapter uses mudstone porosity as a proxy for exhumation to infer the amount of rock uplift that has occurred in western Wellington since the Pliocene.

6.1 Rock uplift definition

England and Molnar (1990) classify three different types of displacement to quantify vertical crustal movements of the Earth: rock uplift, exhumation, and surface uplift. The relationship between them is:

$$Rock\ uplift = exhumation + surface\ uplift \quad (6.1)$$

Where rock uplift is the upward vertical movement of an individual rock particle through the rock column with respect to the geoid. Surface uplift refers to vertical uplift of the land surface with respect to the geoid, and can be calculated by subtracting sea level from the geoid (England and Molnar, 1990). Surface uplift differs from rock uplift in the sense that it does not take into account erosion. Exhumation represents the amount of rock vertically eroded from a surface, and differs from erosion in the sense that it is a solely a vertical measure (Pulford and Stern, 2004). Elevations reported in this text are relative to the New Zealand Vertical Datum 2009 (NZVD), henceforth referred to as the reference geoid. For this study, the reference used for both rock uplift and exhumation is depth of maximum burial beneath sea level.

6.2 Past exhumation studies

Rock uplift and exhumation can be calculated using a number of methods, some of which are discussed below:

Marine terraces

Uplift rates for marine terraces represent average uplift rates and are only valid for when those terraces formed (Pulford, 2002). For example, on Wellington's south coast, the MIS 5e marine terrace at Tongue point has an uplift rate of ~0.6 mm yr^{-1} (Ota et al., 1981). There are other, higher marine terraces proximal to Tongue Point, potentially formed during MIS 7, but their ages are uncertain, therefore making their uplift rates uncertain (Ota et al., 1981).

Seismic reflection

Seismic reflection can be used to estimate exhumation; these calculations are based on the amount of sediment has removed from the seismic section and therefore requires knowledge of the original thickness of the sedimentary sequence (Pulford, 2002). For example, Stagpoole (1997) inferred up to 1.5 km of exhumation has occurred near the Taranaki Fault since the Miocene using this technique.

Porosity depth relations

Porosity depth relations in mudstone can be used to derive exhumation; in other words, porosity-depth relations can yield an estimate of the depth to which sediments have been buried and hence the amount of material that has since been removed through erosion (Armstrong et al., 1998; Pulford, 2002; Wells, 1989). This method is suited to North Island and indeed, the study area of this thesis, owing to the simple history of marine sediment accumulation and burial, followed by exhumation (Pulford, 2002). The method assumes that the examined lithologies have been unchanged since burial and thus have not been altered by factors such as cementation or heating.

Armstrong et al. (1998) carried out an extensive exhumation study on the Western Platform in the Taranaki Basin. They used porosity/depth trends from wells to calibrate to exhumed sections onshore. Armstrong et al. (1998)'s results ranged from 150 m of subsidence to 3000 m of exhumation since the Miocene from analysis of multiple wells in the Taranaki Basin. The results of this study are in good agreement with estimates of exhumation using vitrinite reflectance, apatite fission-track analysis (AFTA), and seismic stratigraphy (Armstrong et al., 1998; Pulford, 2002).

Pulford and Stern (2004) also used Armstrong et al. (1998)'s technique to successful effect, determining over 2 km of exhumation in central North Island since 5 Ma (subsection 1.2.2).

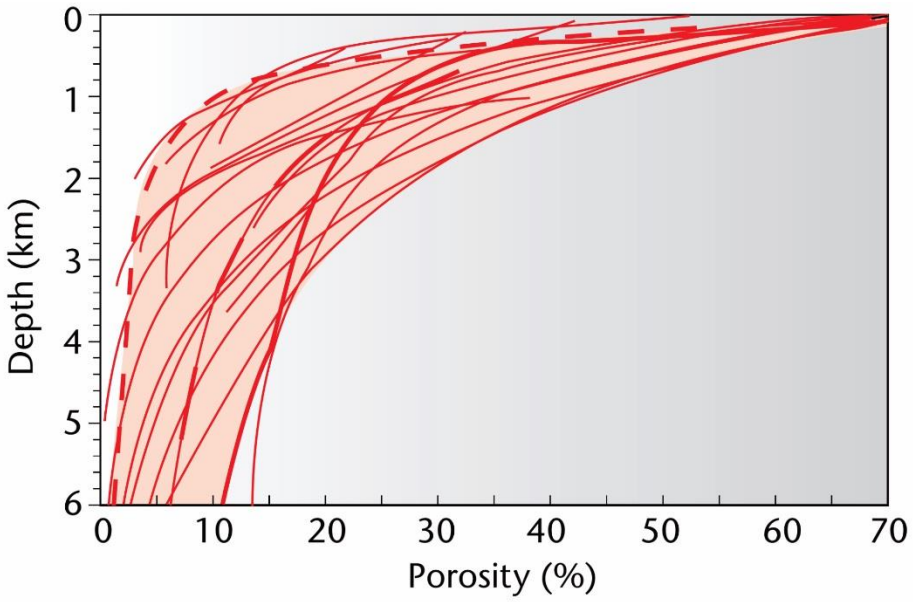

Figure 6.1 A compilation of porosity-depth curves for mudstones/shales. Data from Giles (1997). Figure from Allen and Allen (2013).

We use the method of Armstrong et al. (1998) in order to determine the amount of exhumation western Wellington has been subjected to since the Upper Opoitian (Figure 1.6). We use the same depth porosity parameters and trends for Wellington as Armstrong et al. (1998) did for the Taranaki Basin and Pulford and Stern (2004) did for western central North Island.

6.3 Sample location and data collection

Data used for this study come from silty mudstone samples from the Printers Flat core, drilled in Makara, 1988 (Figure 1.8). Elevation of the drill-hole location was measured off a 1 m resolution DEM. Core plugs were taken using a handheld drill with a 1" diamond core plug drill bit with ethanol as the drilling fluid. Ethanol was used as it does not break down clay material, unlike water, which when used, caused the sediment to disintegrate. Twenty-six samples were taken at approximately 1 m intervals. One metre intervals were not always possible due to the fractured nature of the core and presence of fossil material. The core plugs were then sent to Core Laboratories in Auckland to be analysed for porosity via helium analysis (Dorsch and Katsube, 1999).

Thirteen supplementary samples were obtained with a hacksaw. These samples were cut down to thin sections and impregnated with blue dye in preparation for point counting.

The blue dye was unable to penetrate pore space in most thin section samples. The exceptions were samples MTS 5 and 5a where there was partial blue dye penetration.

6.4 Porosity results

Collection details and porosity measurements for samples analysed via helium and point counting are recorded in Table 6.1 and Table 6.2, respectively.

Table 6.1 Sample details and results for helium porosity analysis.

Sample name	Core depth (m)	Elevation (m asl)	Measured porosity ϕ0' (%)	Exhumation Δz' (m)
MCP06	-4.1	32.9	25.9	-1489
MCP07	-4.8	32.2	24.2	-1644
MCP08	-6.5	30.5	26.4	-1444
MCP10	-8.7	28.3	23.5	-1711
MCP10A	-8.7	28.3	22.7	-1792
MCP11	-9.7	27.3	24.3	-1630
MCP12	-11.3	25.7	25.6	-1518
MCP13	-12.3	24.7	27.0	-1397
MCP14	-13.2	23.8	23.4	-1718
MCP15	-14.4	22.6	25.7	-1505
MCP16	-16.2	20.8	23.4	-1717
MCP16A	-16.2	20.8	23.1	-1749
MCP17	-18	19	25.1	-1564
MCP18	-19.2	17.8	23.3	-1729
MCP19	-20.3	16.7	26.4	-1445
MCP19A	-20.3	16.7	26.0	-1485
MCP22A	-24.2	12.8	25.8	-1498
MCP23	-25.7	11.3	23.8	-1686
MCP24	-27.5	9.5	24.9	-1581
MCP24A	-27.5	9.5	25.5	-1521
MCP26	-31.3	5.7	23.7	-1687
		Average:	24.8	-1596

Table 6.2 Sample details and results for point-counting porosity analysis

Sample name	Sample depth (m)	Porosity (100 point counts) (%)
MTS01	2.5	N/A
MTS02	56	N/A
MTS03	41.1	N/A
MTS04	29.5	N/A
MTS05	27.3	18
MTS05A	27.3	21
MTS06	16.8	N/A
MTS07	17.3	N/A
MTS08	3.6	N/A
MTS09	4.3	N/A
MTS10	132	N/A
MTS11	109.8	N/A
MTS11A	109.8	N/A

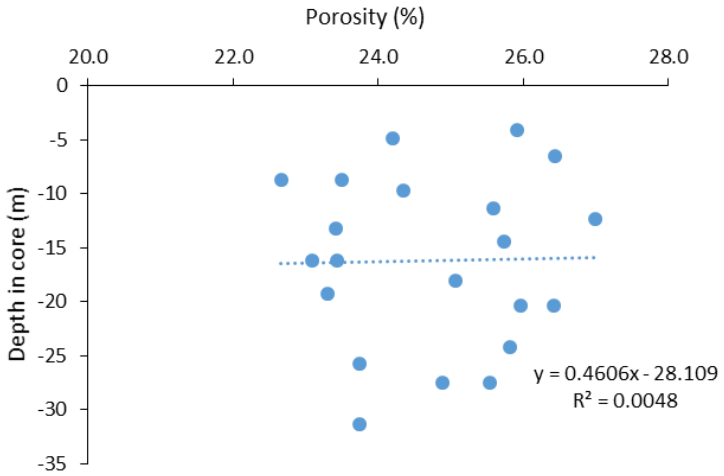

Figure 6.2 Porosity (%) results with depth from helium analysis

Helium porosity results were variable, with no clear correlation between porosity and depth. Therefore, core plugs were analysed by eye and rejected if they were deemed to have a large amount of micro-fractures or fossil material present. The resulting porosity vs. depth relationship was just as inconclusive, and variable with depth (22.7 % – 27.0 %) (Figure 6.2) (Table 6.1). This is likely to be due to sampling over a depth of approximately thirty metres, as opposed to hundreds of metres as was the case for Armstrong et al. (1998)'s study. Nevertheless, the overall range of measured porosities are still low and potentially suggestive of large amount of overlying sediment in the past. Indeed, based

solely on a compilation of porosity depth curves (Giles, 1997), this sediment has been buried between approximately 800 – 2800 m (Figure 6.1).

Porosity measurements made via point counting were done on samples MTS 5 and 5a (27.3 m core depth). One hundred point counts were done on each thin section yielding porosity values of 18 and 21 % for MTS 5 and 5a respectively (Table 6.2).

The porosity values obtained via point counting were lower than the average helium porosity value (24.8 %). This is not surprising as porosity measurements are commonly lower than those measured via helium. The helium porosity values were used for exhumation calculations.

6.5 Exhumation

The relationship between porosity (φ) and depth (z) is given by the equation (Athy, 1930):

$$\varphi(z) = \varphi_0 e^{-z/D} \qquad (6.2)$$

Where φ_0 is the surface porosity and D represents an exponential decay constant that is a function of lithology. This relationship has the same form for sequences that have been exhumed since deepest burial (equation 6.3):

$$\varphi(z') = \varphi'_0 e^{-z'/D} \qquad (6.3)$$

Where z' is the current depth of the sample, and φ'_0 is the current porosity. In this case, φ'_0 is the measured core plug porosity, and z' is the sample depth from the surface for that core plug porosity. Exhumation ($\Delta z'$) is calculated by taking the difference between the estimated porosity formation depth (z) and the average present depth of the samples (z'):

$$\Delta z' = z - z' = [\ln(\varphi_0) - \ln(\varphi'_0)]/(\frac{1}{D}) \qquad (6.4)$$

Due to the range of exhumation values calculated over the 30 m of sampled core, the average value of $\Delta z'$ (-1596 m) was taken as the measured exhumation (Table 6.1). Uncertainty in exhumation was then calculated using the standard deviation of the data as shown by Armstrong et al. (1998):

$$\sigma(\Delta z') = \Delta z' \sqrt{\frac{\sigma(\ln(\varphi_0))^2 + (\sigma(\ln(\varphi'_0)))^2}{(\ln(\varphi_0) - \ln(\varphi'_0))^2} + \frac{\sigma(\frac{1}{D})^2}{(\frac{1}{D})^2}} \quad (6.5)$$

Values obtained from Armstrong et al. (1998)'s analysis of the tectonically stable Western Platform were used in calculations: φ_0 = 50 (from a standard mudstone porosity curve), D = 2265 m, $\sigma(\ln(\varphi_0))$ = ±0.05 and $\sigma(\frac{1}{D})$ = ± 0.00005 m $^{-1}$.

Results suggest that mudstones at Makara have been subject to 1596 ± 256 m of exhumation, since the Pliocene.

6.6 Surface uplift

Surface uplift is defined by averaging the topographic elevation of the K Surface above sea level. The process is described in section 5.3 (Figure 5.5). This suggests an average K Surface height of 320 ± 20 m.

6.7 Rock uplift

Rock uplift is then calculated using equation 6.1. This yields a rock uplift of 1896 ± 276 m which we round to 1.9 ± 0.3 km, since the Late Opoitian.

7 Discussion and conclusions

This chapter integrates and discusses the results from Chapters 2 – 7. Inferences regarding K Surface deformation and uplift mechanisms are related to previous studies. Specifically, (1) the geologic structure of Makara Village is discussed; (2) Seismic and porosity data are integrated and discussed in relation to past exhumation in western Wellington; and (3) K Surface extent, origin, and uplift mechanisms are discussed.

7.1 Geologic structure of Makara Village

Using the gravity and seismic refraction data obtained during this study, along with information from the Makara drill-core log and past studies done in the area (e.g. Begg and Johnston, 2000; Grant-Taylor and Hornibrook, 1964; McKay, 1877; Reay et al., 1988), inferences regarding the geological structure of Makara and the extent of the Pliocene marine sediment underlying the village are made.

7.1.1 Validity of gravity models

In Chapter 2, two 2D gravity profiles obtained at Makara Village were modelled to estimate the depth of the Pliocene marine sediment underlying the village (Figure 7.2). A constraint on depth to Torlesse greywacke bedrock was provided by a drill-hole (163 m TD) (Reay et al., 1988) located approximately 120 and 730 m SW of Profiles 1 and 2, respectively (Figure 7.2). Density was defined to be between 2150 and 2350 g cm^{-3} for the marine sediment (Section 2.5.1). We determined that the models that fit our constraints the best were Figures 2.8 and 2.10 for Profiles 1 and 2, respectively. Model interpretation lead us to suggest that the marine sediment is thickest in the south end of the valley, proximal to the drill-hole, and thins out to the north, eventually pinching out the valley north of the location of gravity Profile 2 and seismic Line 1 (Figure 7.2).

It is difficult to match up and make the two gravity profiles (Figures 2.8B and 2.10) agree with each other. This is because, unlike Profile 1, Profile 2 implies a 10 – 20 m thick body of marine sediment on the upthrown side of the Ohariu Fault, even though there were no observed exposures of marine sediment in the creeks perpendicular to the fault (rather, greywacke was observed). Furthermore, although a body of marine sediment can be fit in

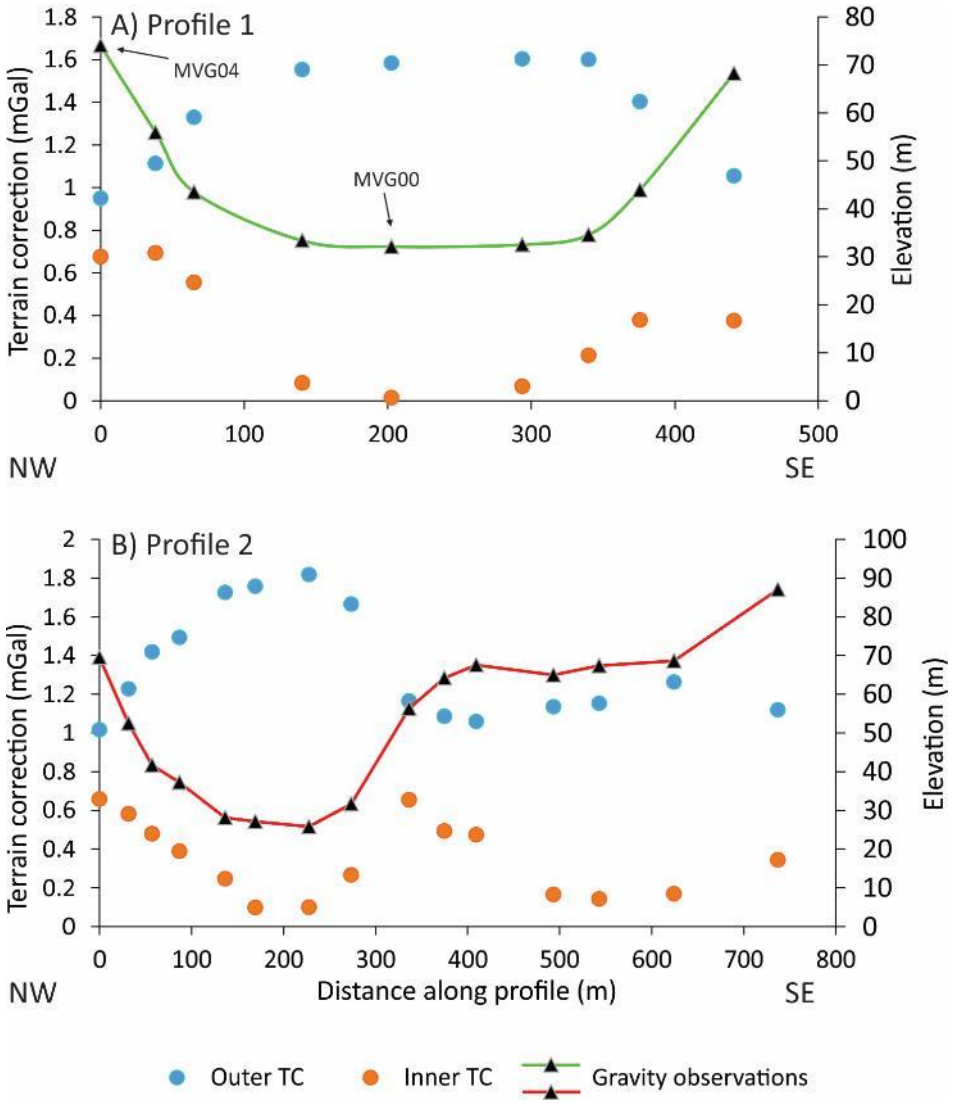

Figure 7.1 Terrain correction (mGal) vs. distance (m) for Profile 1 (A) and Profile 2 (B). Outer terrain corrections (TC) are in blue, inner terrain corrections are in orange. Each black triangle represents a gravity station, and the grey line represents elevation. NB: Each gravity station has both an inner terrain value and an outer terrain value, either above or below the gravity station.

the valley of Profile 2 within error, the error bars are so large that one could almost fit a straight line through the data. This indicates that there is an unresolved issue.

There is an inverse correlation between inner and outer terrain corrections for both profiles (Figure 7.1). This is suggestive of an issue with either the inner or outer terrain correction. Based on the rugged terrain in-between gravity stations, the small size of the survey and the method of inner terrain correction calculation (Hammer zone graticule), it is most likely the inner terrain correction that is causing the issue. Indeed, an inner terrain correction uncertainty of 0.15 mGal was already inferred due to differing outputs depending on

Hammer chart orientation (subsection 2.5.2). However, we propose that there may be additional error due to the way in which the inner terrain correction is calculated (i.e. averaged over block areas). If this is the case, then the uncertainties in the inner terrain correction would probably be greater than maximum anomaly amplitude. Therefore, a benchmarking of inner terrain corrections using numerical methods for micro-gravity surveys is required to resolve this issue.

Based on the above discussion, Profile 2 is discarded as it is uninterpretable. In the case of Profile 1, we can only make the residual anomaly agree with the drill-core data by modelling a faulted, SE thickening marine sediment body (Figure 2.8B). The reduction of Profile 1 would have been subject to the same issues as described previously for Profile 2 (I.e. rugged terrain resulting in additional error in the inner terrain correction), and therefore should be treated with caution. Nevertheless, we make use of Profile 1 (Figure 2.8B) when interpreting the underlying structure of the village (Subsection 7.1.2), as we are able to correlate the modelled result with the drill-hole.

7.1.1 Marine sediment extent

Because we have discarded gravity Profile 2, we must confirm the presence of the marine sediment at the north end of the valley, as it has implications for our seismic data (i.e. determine what lithology is being imaged) (Chapter 3).

Seismic P wave velocities derived for V_2 using the plus-minus method were 2.6 and 2.7 km s^{-1} for Lines 1 and 2, respectively (Figure 7.2). Using the WHB inversion, we determined a maximum P wave velocity of 3.2 km s^{-1} at 18 m below the V_1/V_2 refractor. This is consistent with the velocities obtained via the plus-minus method as the long offset shot used for the WHB inversion (shot 2038) imaged deeper than the smaller offset shots used for the plus-minus method. Thus, our V_2 layer has a velocity of 2.6 – 3.2 km s^{-1}. The range is due to velocity increases with depth as a result of compaction effects.

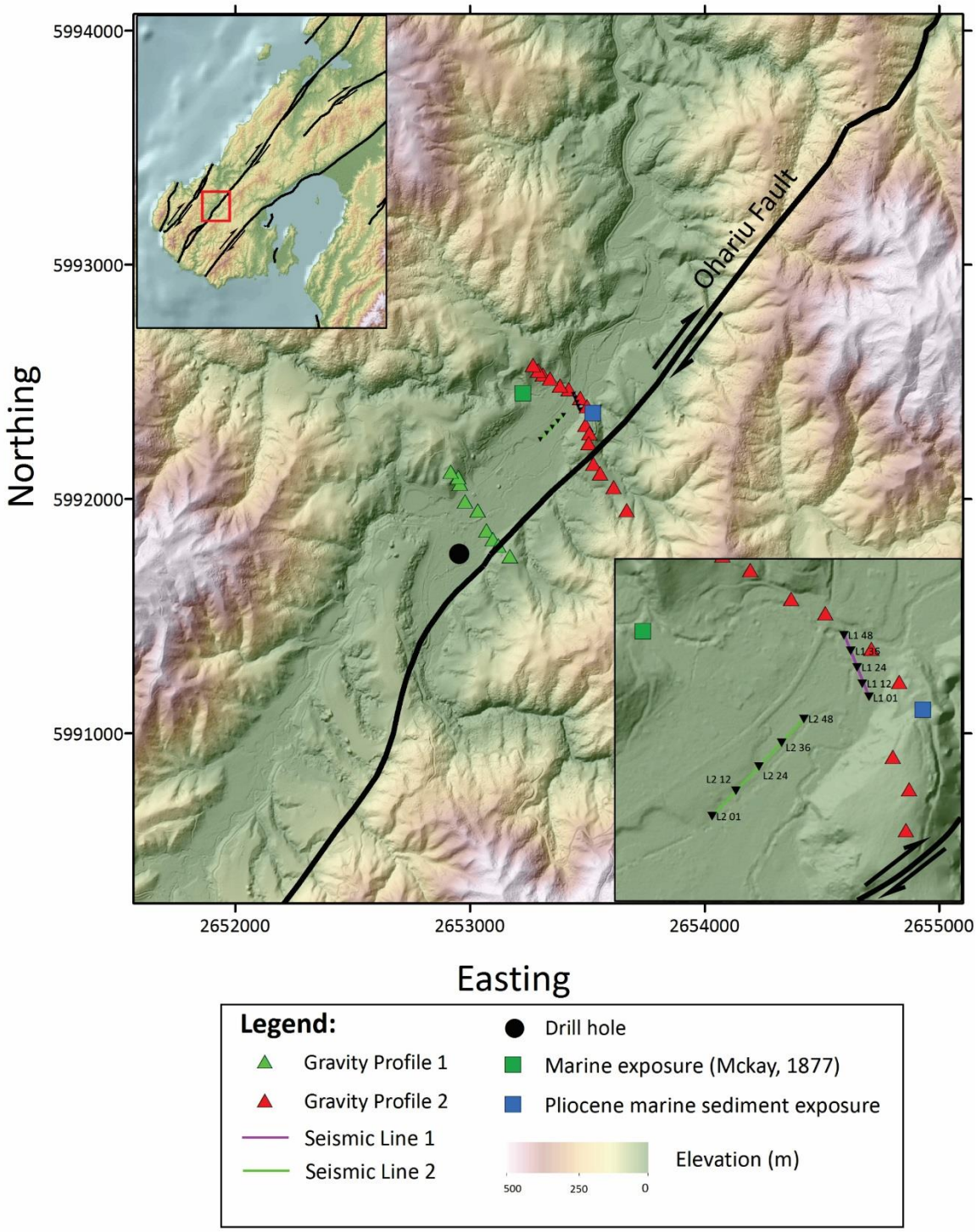

Figure 7.2 Map showing relationship between seismic and gravity survey locations. DEM in zoomed out figure from VUW. DEM in zoomed in figures from Landcare Research. Bathymetry from NIWA. Faults from GNS Active Faults Database.

Table 7.1 Torlesse greywacke P wave velocities throughout New Zealand

P wave velocity (km s^{-1})	Locality	Reference
4.9 – 5.4	Ruapehu, 1700 m deep	Sissons and Dibble (1981)
4.6 – 5	Northern Hauraki Gulf, < 2.4 km deep	Ferguson et al. (1980)
3.2 – 5.15	Southern Alps	Garrick et al. (1973)
4.3 – 4.8	Broadlands geothermal field, Waikato	Hochstein and Hunt (1970)
3.4 – 5.1	Wellington Harbour and Seaview	Hochstein and Davey (1974)
4.2 – 5.2	SAHKE I and II, southern North Island	Henrys et al. (2013), Tozer (2013)

Based on past P wave measurements in Torlesse greywacke displayed in Table 7.1, our P wave velocities on their own seem too low to be basement Torlesse. Our maximum velocity is close to the minimum velocities of Hochstein and Davey (1974), and Garrick et al. (1973). However due to the shallow imaging depth (i.e. ~3 – ~20 m), it is possible that these low velocities are representative of fractured, less dense Torlesse greywacke.

Due to ambiguity in using solely P wave velocities to estimate lithology, V_p/V_s and Poisson's ratios were calculated for multiple shots from seismic Lines 1 and 2 (Table 3.2). Results suggest an average V_p/V_s ratio of 3.5, which corresponds to an average Poisson's ratio of 0.46.

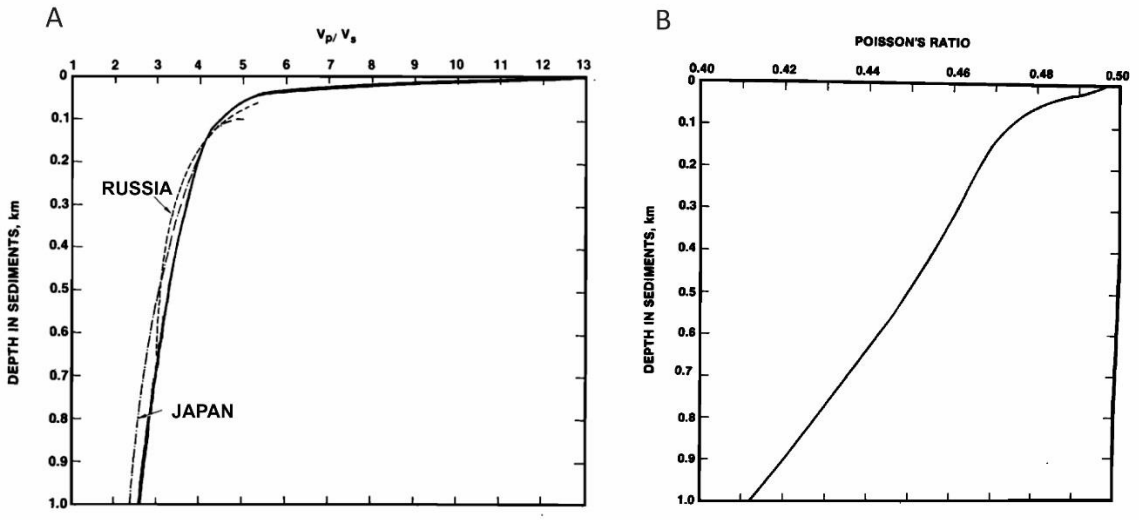

Figure 7.3 A) V_p/V_s ratios vs. depth for marine terrigenous sediments (mainly silt clays, turbidites, mudstones and shales). Data from deep boreholes in Russia (Vassil'ev and Gurevich, 1962) and Japan are also shown for comparison. B) Poisson's ratio vs. depth in terrigenous marine sediments (mainly marine silt clays, turbidites, marine mudstones and shale). Figures adapted from Hamilton (1979).

Christensen and Okaya (2007) measured compressional and shear wave velocities in the Rakaia terrane of Torlesse greywackes in South Island New Zealand. At 20 MPa pressure, they inferred that the V_p/V_s ratio in greywackes was 1.69, with a Poisson's ratio of 0.214 (averaged out over 5 wells). Interestingly, the change in V_p/V_s ratio from 20 MPa to 1000 MPa pressure was not substantial. The V_p/V_s ratio averaged 1.71 with an average Poisson's ratio of 0.242. Hamilton (1979) modelled V_p/V_s and Poisson's ratios with depth for marine rocks (Figure 7.3). Hamilton (1979)'s data indicates that V_p/V_s ratios range from approximately 13 at the sea floor to 2.6 at 1000 m depth (Figure 7.3A). Poisson's ratios range from 0.5 at the sea floor to 0.41 at 1000 m depth (Figure 7.3B).

V_p/V_s ratios and Poisson's ratios measured in Torlesse greywacke by Christensen and Okaya (2007) are much lower than those calculated at Makara. Conversely, the modelled marine rock V_p/V_s ratios and Poisson's ratios by Hamilton (1979), agree with the data obtained at Makara. Therefore, based on V_p/V_s and Poisson's ratios, and exposures in the northern end of the valley reported by McKay (1877) and Grant-Taylor and Hornibrook (1964) (Figure 7.2), we infer that the rock underlying Makara at the north-eastern end of the valley is the Pliocene marine sediment.

7.1.2 Structure

It is difficult to determine the subsurface structure of Makara Village due to the domination of bedrock, and lack of previous data. Nevertheless, evidence from the drill-core shows two granule/grit layers between approximately 92 – 100 and 132 – 138 m TD (Figure 1.8). There is also occasional bedding present, with dips ranging 5 – 25 °, with a representative average dip of 15 °. The dip direction is unknown as these measurements were made once the sediment was cored (Reay et al., 1988). Interestingly, in the marine sediment exposure a few hundred metres north of the drill-core location, on the scarp of the Ohariu Fault (Figure 7.2), its physical characteristics match those of the course granule layers from the core. Both the core location and the exposure location are located on the same side of the main trace of the Ohariu Fault. The elevations of the exposure and the lowest granule layer within the core are approximately 66 and -100 m respectively. This geometrical relationship suggests that the marine sediment dips roughly towards the SW. Figure 7.4 displays a schematic fault parallel cross-section that goes through the drilling location and the exposure. If we extrapolate the most representative bedding dip from the core (15 °) and project it from the exposure location, it comes within roughly 60 m of the lowest granule layer. Error in this estimate could be due to, but not limited to, bedding dip error and/or deformation due to faulting. Furthermore, this schematic is also consistent with the modelled marine sediment depth for gravity Profile 1 (Figure 2.8B). Indeed, this is arguably the most likely geometrical explanation for matching up these granule layers.

An important aspect to consider is whether the inferred dip of the marine sediment bias the seismic velocities at depth. The long offset shot used for the WHB inversion in Chapter 3 shoots towards the SW, which is the same as the inferred down dip direction for the marine sediment. If anything, this would bias the P wave velocity to lower values. These implications in section 7.2.

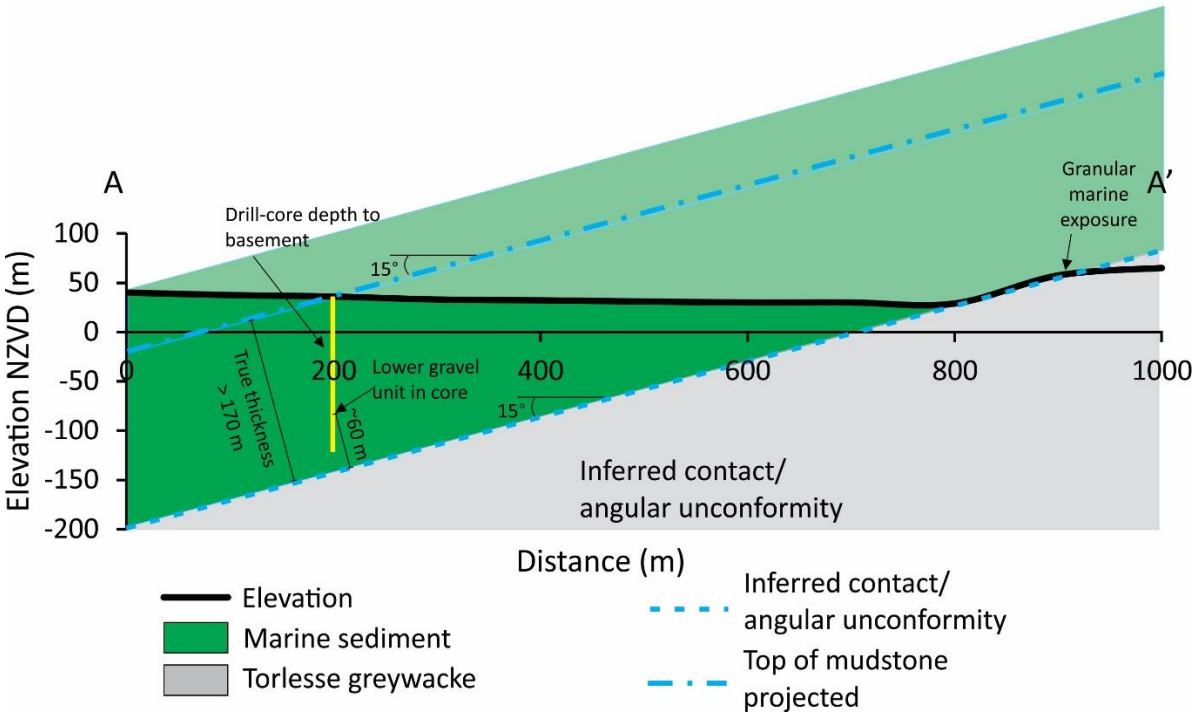

Figure 7.4 Schematic fault parallel cross-section for the subsurface structure of the Pliocene marine outlier. Cross-section location A – A' is plotted on Figure 7.6.

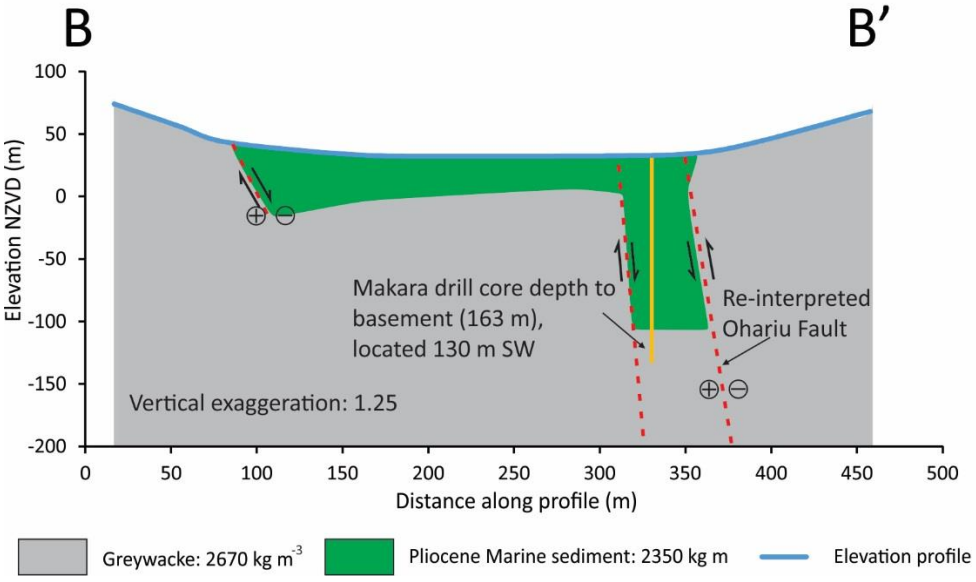

Figure 7.5 Schematic cross-section of the subsurface structure for gravity Profile 1. Cross-section location B – B' is plotted on Figure 7.6.

The interpretation of Gravity Profile 1 (Figure 2.8B) can potentially be explained by an eastward dipping Ohariu Fault with two splays to the west that drop down the marine sediment, as shown schematically in Figure 7.5. This interpretation satisfies the residual anomalies for Profile 1 and the drill-hole data. Furthermore, an eastward dip on the Ohariu Fault suggests a reverse sense of vertical displacement, which is consistent with a possible reverse component reported from the drill-core data (Reay et al., 1988; Litchfield et al., 2010). Figure 7.6 displays the map view of the geological interpretation for Makara Village.

The way in which the marine outlier came to be preserved in a miniature basin is an interesting question. The two simplest possibilities are: 1) Basin formation due to strike-slip motion, 2) Basin formation due to dip-slip motion. It seems unlikely that basin formation was due to strike-slip motion as the bend in the fault trace south of the valley is compressional, and not substantial in size (Figure 7.6). Therefore, the more likely scenario is that the Pliocene marine sediment has been down faulted, and thus preserved, via dip-slip motion, forming a pull-apart basin as previously suggested by Begg and Mazengarb (1996).

7.2 Integration of seismic and porosity data

In Chapter 6, we determined that the marine sediments preserved on the downthrown side of the Ohariu Fault have been exhumed approximately 1596 ± 256 m, (rounded to 1600 ± 300 m) since their deposition during the Pliocene. This corresponds to 1900 ± 300 m of rock uplift when taking into account the surface uplift of the K Surface (section 6.6). Since exhumation represents the amount of rock vertically eroded from a surface, we can state that the marine sediment was buried to a depth of 1580 ± 300 m (taking into account the elevation of the marine sediment) before uplift. P wave velocity can be used as a proxy for burial depth. Indeed, Stagpoole (1997) developed velocity-depth curves for rocks from multiple basins throughout New Zealand. Stagpoole (1997) divided the velocity data into broad areas on the basis of Neogene tectonic history:

- Back-arc regions: Northland, Taranaki, and the West Coast
- Fore-arc region: East Coast

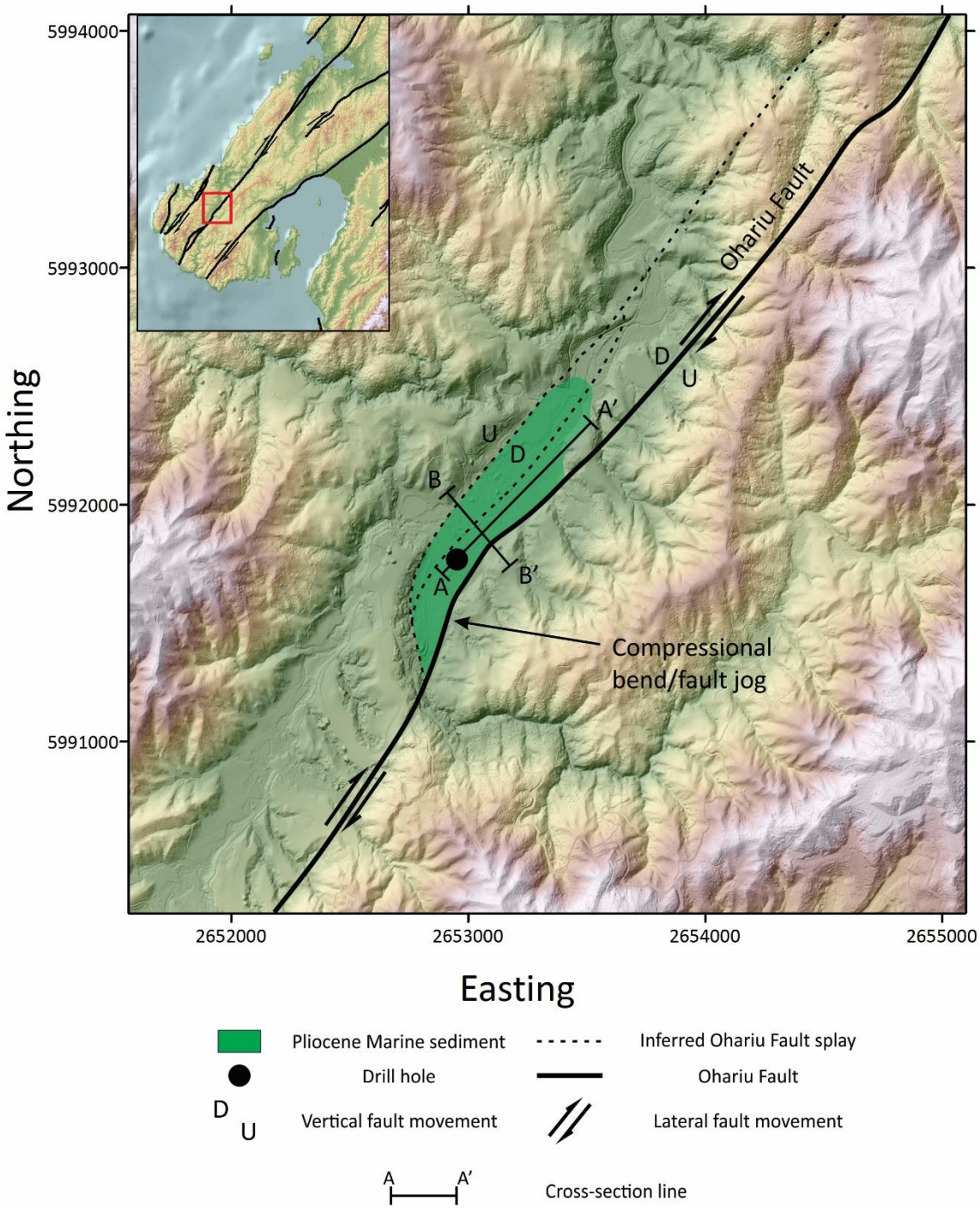

Figure 7.6 Map view of Makara Village showing interpretation of fault traces. A-A' cross-section in displayed in Figure 7.4; B-B' cross-section is displayed in Figure 7.5 and represents Gravity Profile 2. Cross section locations are approximate. Faults from Active Fault Database, DEM from Landcare Research, bathymetry from NIWA.

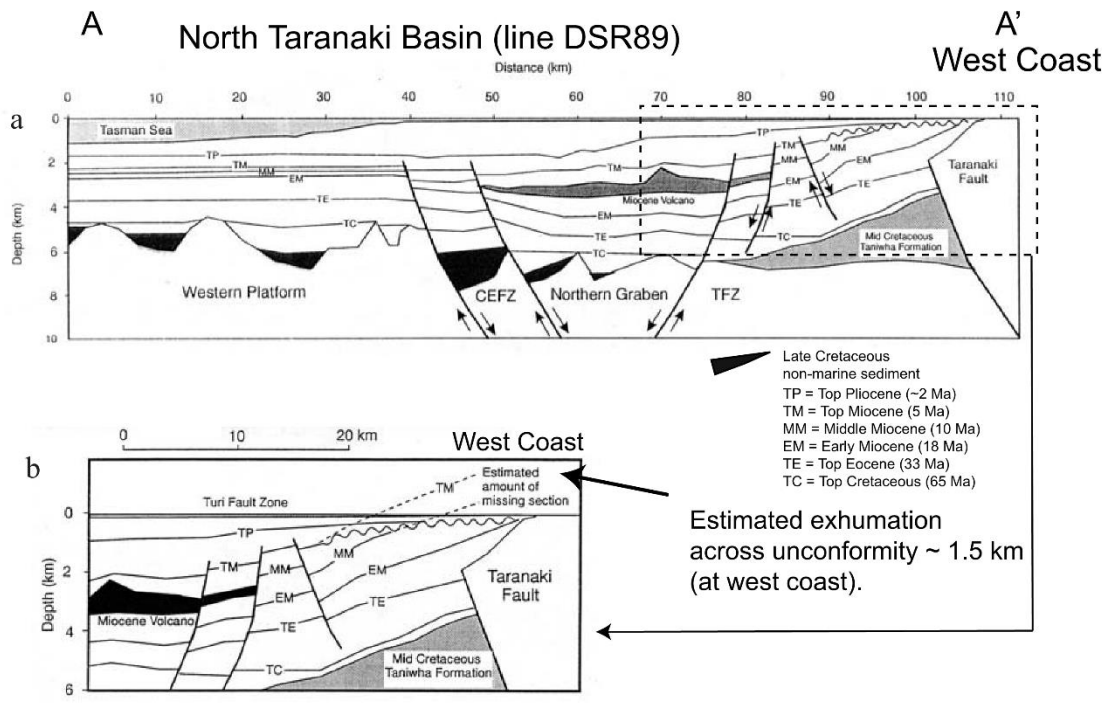

Figure 7.7 (a) Cross-section of seismic line DSR89 (C-C' on Figure 7.9).The unconformity on the top of the Miocene surface (5 Ma) is marked by the undulating line and is interpreted to mark uplift initiation of central North Island. CEFZ is Cape Egmont Fault Zone, (b) Zoomed in version of (a). After Stagpoole (1997) (Stern et al., 2006).

The marine sediment at Makara is from the (southern) Whanganui Basin, which is considered to be a proto-back-arc basin, with its northern extent located on the southern termination of the extensional back-arc area of the CVR. The basin has been considered part of the back-arc region in the past (e.g. Davey and Stern, 1990); however, the basin differs from classic back-arc basin definition due to the lack of arc volcanism and the presence of compressive tectonics that act on the western and eastern edges of the basin. The Whanganui Basin is also not a fore-arc basin. Therefore, due to the Whanganui Basin being neither a traditional back-arc, nor fore-arc basin, there is ambiguity in terms of what velocity-depth curve is most appropriate for the Makara sediments.

Using seismic reflection data, Stagpoole (1997) identified an unconformity in the Taranaki Basin at the Miocene-Pliocene boundary that dips westward, away from central North Island (Figure 7.7). The Pliocene strata above the unconformity dip in the same direction, with the dips gradually increasing with age (Stagpoole, 1997; Stern et al., 2006).

Stern et al. (2006) interpret this pattern to be a result of progressive uplift throughout the Pliocene, related to the rapid uplift in central North Island proposed by Pulford and Stern (2004).

Stratigraphic reconstructions by Stagpoole (1997) indicate that 1 – 1.5 km of rock was removed from above the unconformity at the North Taranaki coast during Pliocene uplift (Figure 7.7). This magnitude of rock removal agrees with rock uplift amounts calculated by Pulford and Stern (2004).

The wells from the Taranaki Basin Stagpoole (1997) used for velocity-depth relations are predominantly within the same area where the Miocene-Pliocene unconformity is present, and thus, also proximal to the area subject to rapid uplift during the Pliocene. This Pliocene uplift is proposed to be due to the viscous removal of mantle lithosphere into the underlying asthenosphere (Stern et al., 2013). This uplift event explains the stark difference between the Miocene and Pliocene velocity-depth curves derived from Taranaki, Northland and West Coast wells. The Whanganui Basin, and indeed, Wellington, were not exposed to this uplift event. Thus, velocity-depth relations derived from the Taranaki Basin are not suitable for the marine sediments at Makara. The velocity-depth curves for the East Coast Basin, on the other hand, are nearly identical for Pliocene and Miocene aged sediments. Hence, we use the velocity-depth relations from Stagpoole (1997) for the East Coast Basin to compare with our porosity dataset.

P wave velocity measurements in the marine sediment at Makara range between 2.6 – 3.2 km s^{-1}. Based on Stagpoole (1997)'s velocity-depth curve for the East Coast Basin, the Makara marine sediments are predicted to have been buried to a depth of 1800 ± 500 m before being uplifted to where they are today. This estimate is larger than the exhumation amount of 1600 ± 300 m calculated using porosity-depth relations; however, the exhumation amounts agree within uncertainty. Indeed, from this result it seems the inferred SW bedding dip of the Pliocene marine sediment (subsection 7.1.2) does not bias the P wave measurements. One possible reason for the larger burial depth using the velocity-depth method is that the higher velocities (i.e. 3.2 km s^{-1}) we measured are most

likely from a deeper (older) part of the marine sediment compared to the part where porosity samples were taken (subsection 7.1.2).

An important aspect to consider is whether the inferred dip of the marine sediment bias the seismic velocities at depth. The long offset shot used for the WHB inversion in Chapter 3 shoots towards the SW, which is the same as the inferred down dip direction for the marine sediment. If anything, this would bias the P wave velocity to lower values

Based on the soft, "putty" like texture of the Makara marine sediment, previous authors (e.g. Begg and Johnston, 2000; Reay et al., 1988) have postulated little (i.e. < 500 m) younger sedimentary to ever cover the marine sediment. Results from seismic refraction and porosity-depth relations suggest otherwise and are in good agreement within uncertainty. Therefore, we can say with confidence that there has been 1700 ± 500 m of exhumation in western Wellington since the Pliocene. Including surface uplift (i.e. 220 m mean K Surface elevation), equates to 1900 ± 500 m rock uplift in western Wellington since the Pliocene. If we assume a constant rate of exhumation in western Wellington since the Pliocene (~1700 m in ~3 Ma), this corresponds to an exhumation rate of approximately 0.57 mm yr^{-1}.

7.2.1 Comparison with past studies

In the Wairarapa, Tozer (2013) modelled Miocene – Pleistocene sedimentary basin depths adjacent to the Wairarapa, Martinborough, and Huangarua Faults to be 2.16, 1.24, and 2.70 km, respectively (Figure 7.8A). In Whanganui Basin, Pliocene-Pleistocene sediments were modelled by Tozer (2013) to have a maximum burial depth of ~4 km (Figure 7.8B). These burial depths are comparable to those calculated for during this study for Pliocene aged sediments (1800 ± 500 m). The sediments in Whanganui Basin have been subject to subsidence throughout the Pliocene, whereas the Wairarapa has been subject to progressive uplift since the Middle Pliocene (Lee et al., 2002). Thus, we would expect Whanganui Basin Pliocene sediments to be buried deeper. The sediments at Makara were once part of the southern Whanganui Basin, but have since been uplifted and eroded.

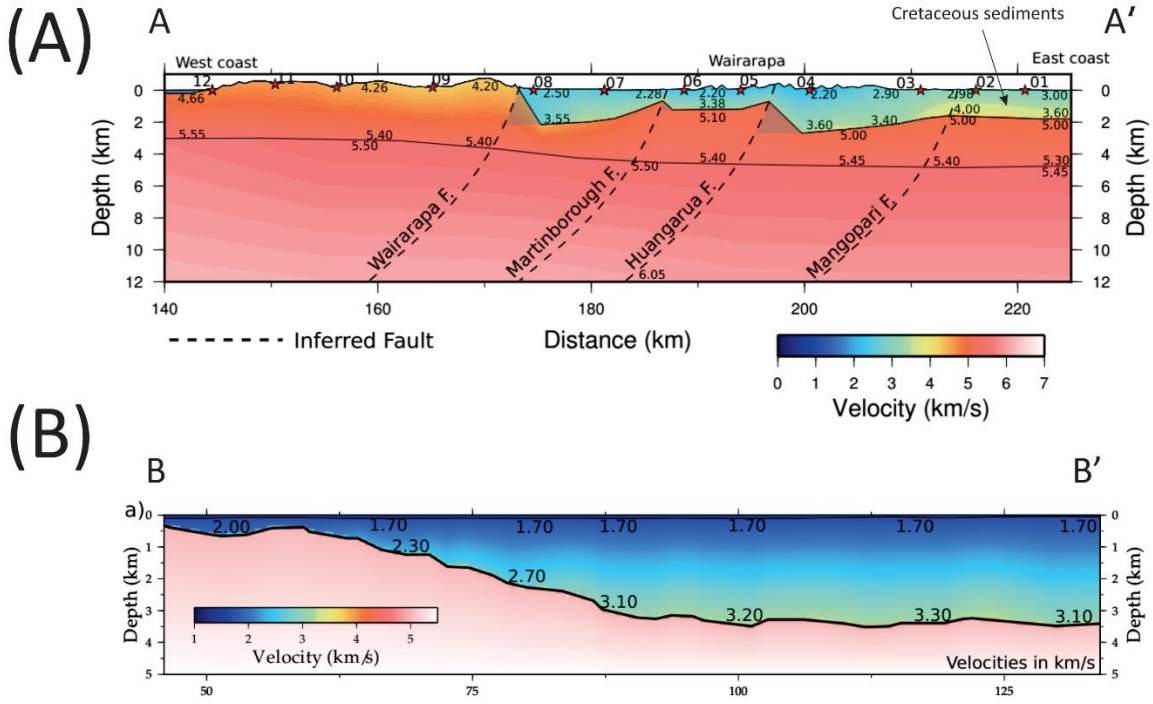

Figure 7.8 (A) Velocity model along line A – A' (Figure 7.9). Miocene to Pleistocene sediments east of the Wairarapa Fault are modelled as 2.5 km s^{-1} at the surface, increasing to 3.6 km s^{-1} at a maximum depth of 2.70 km east of the Huangarua Fault. The velocities east of the Mangopari Fault are Cretaceous aged. The higher velocities displayed in red represent Torlesse bedrock The red stars indicate shot locations. (B) Velocity model along B – B' (Figure 7.9). Figures adapted from (Tozer, 2013).

.

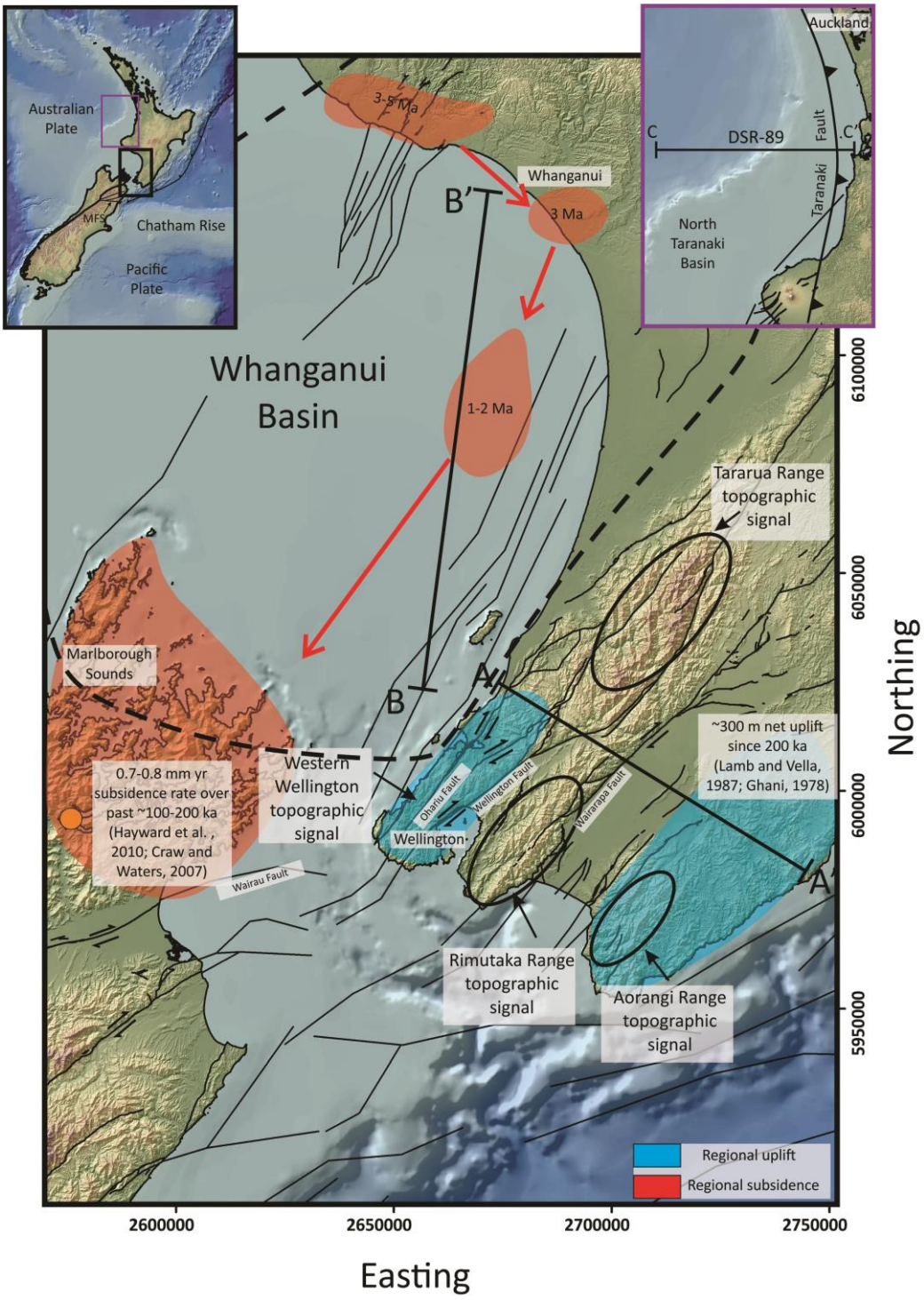

Figure 7.9 Map of the regional study area. Areas of uplift and subsidence (through time), are shown by the blue and red translucent blobs, respectively. Note the southward migration of subsidence represented by the southward migration of the Whanganui Basin depo centre since the Pliocene (Anderton, 1981). A-A' and B-B' are the Locations of SAHKE seismic lines analysed by Tozer (2013) and Henrys et al. (2013) (Figure 7.8). C-C' is the location of seismic line DSR-89 (Figure 7.7). Note the rugged, pointy hilltops that represent the Tararua, Rimutaka and Aorangi Ranges topographic signatures compared to the low relief, elevated K Surface topographic signature. Bathymetry data from NIWA, DEM from Victoria University, onshore faults from GNS active fault database, offshore faults from Litchfield et al. (2014).

7.3 K Surface extent, origin, and uplift mechanisms

7.3.1 K Surface extent

The K Surface is defined by low relief, elevated surfaces, whereas the Tararua, Rimutaka and Aorangi Ranges are characterised by steep, rugged terrain with higher elevation (Figure 7.9).

We map the southern termination of the K Surface as a margin perpendicular line across western Wellington a few hundred metres south of Quartz Hill (Figure 5.6). The southern extent of the K Surface is defined by an increase in average elevation and a decrease in ridge width, which results with few areas picked up by the modelling parameters (Figure 5.1). This differing morphology may be due to activity on the Wairau Fault, which extends into the Cook Straight (Barnes and de Lépinay, 1997), and thus may be a player in the uplift of southern-most Wellington. Alternatively, it could also be due to some other, unknown uplift mechanism.

7.3.2 K Surface age and origin

Previous authors have suggested multiple mechanisms for K Surface formation, such as peneplanation (Cotton, 1912b), pediplanation (Cotton, 1957), and formation as a regional marine platform (Cotton, 1957; Ota et al., 1981; Stevens et al., 1974). The current thinking is that the K Surface was a regional erosion surface (Figure 7.10), cut during Quaternary uplift (Ota et al., 1981). Specifically, Ota et al. (1981) suggest that a low relief erosion surface had already been formed during Pliocene time, with the Pliocene sea covering most of the Wellington region. This resulted in initial planation and hence, further deposition (Ota et al., 1981). Quaternary uplift resulted in the erosion of the Pliocene sediment, and thus re-exposure, and planation of the bedrock, excluding the down-faulted outlier in Makara Valley (Ota et al., 1981).

Based on research done for this thesis, we present and test two end-member arguments in regards to K Surface origin:

(1) The K Surface was cut as a singular regional erosion surface (e.g. Begg and Johnston, 2000; Cotton, 1957; Ota et al., 1981) which was then subsequently uplifted and deformed (Figure 7.10A).

(2) The "K Surface" was not formed as a sole regional surface, rather, it is composed of multiple time transgressive marine platforms, cut at different times due to differential uplift (Figure 7.10B).

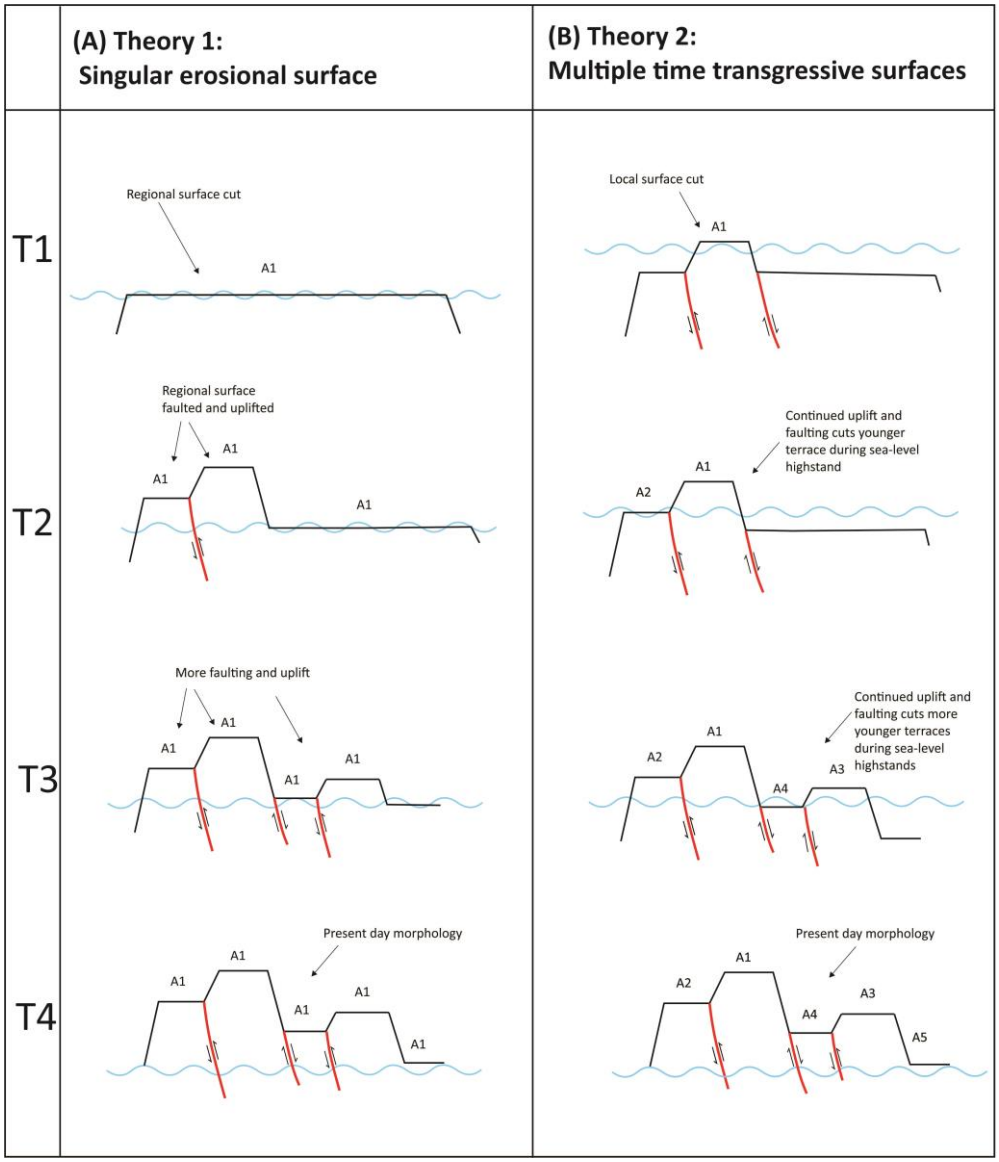

Figure 7.10 Schematic figure illustrating the two theories for K Surface formation, as discussed in the text. (A) Theory 1: K Surface formation as a singular, regional erosion surface, (B) Theory 2: K Surface formation via multiple, stepped, time transgressive surfaces. T1-T4 represent unit-less time-steps from K Surface formation (T1) through to the present day K Surface morphology (T2). A1 – A5 represent different aged surfaces where A1 is the youngest and A5 is the oldest.

Figure 7.10 illustrates the two theories described above schematically in a series of time-steps from K Surface formation (T1) through to present day morphology (T4). A1 – A5 represent relative terrace age where A5 is the youngest.

The depth profile of cosmogenic ^{10}Be (Figure 4.9) indicates that the K Surface at this locality was eroded and exposed at the Earth's surface $238.1^{+149.3}_{-141.7}$ ka (2σ) (Figure 4.5). This age is similar to the timing of the MIS 7 (243 ka) interglacial when sea-levels were > 1 m greater than today (Lisiecki and Raymo, 2005). At first glance, this contradicts older deposits reported in the Wellington area (e.g. the 345 ± 12 ka Rangitawa tephra and the c. 1.2 – 0.4 Ma Kaitoke Gravel). However, neither the Rangitawa Tephra, nor the Kaitoke Gravel (c. 1.2 – 0.4 Ma) are reported at the sampled location. We do not consider the 1.09 ± 0.12 Ma TVZ silicic tephra an age constraint for the K Surface, as it is only exposed at Transmission Gully, proximal to the southern extent of the Tararuas, which, as explained in Chapter 1.1, has been exposed to greater erosion and uplift. Therefore, the simplest explanation is that this dated remnant of the K Surface was cut as a marine platform during MIS 7 (Figure 7.11). This suggests an uplift rate of $1.26^{+1.85}_{-0.48}$ mm yr^{-1} (corresponding to minimum and maximum uplift rates of 0.79 mm yr^{-1} and 3.36 mm yr^{-1} respectively). An important aspect to note however, is that the dated K Surface remnant age agrees with the Rangitawa Tephra age within uncertainty. Thus, it is possible that the dated remnant was cut shortly before the tephra deposition at a different interglacial within the dated uncertainty.

If the K Surface was cut as a regional marine platform, it would mean that all other K Surface remnants (e.g. Mt Kaukau) are also ~240 ka. Based on the presence of older deposits dispersed in patches around the Wellington landscape (e.g. the 345 ± 12 ka Rangitawa Tephra at Johnsonville), it seems more likely that the K Surface was cut, at this time, as multiple localised marine platforms.

The erosion rate for the dated K Surface remnant was calculated to be $1.79^{+0.59}_{-0.83}$ cm ka^{-1} (2σ), corresponding $4.3^{+2.5}_{-2.7}$ m of erosion since exposure at $238.1^{+149.3}_{-141.7}$ ka (Figure 7.11). If the "K Surface" is actually a sequence of marine terraces that have been translated and uplifted by different amounts, then it makes sense that the higher the remnant, the older

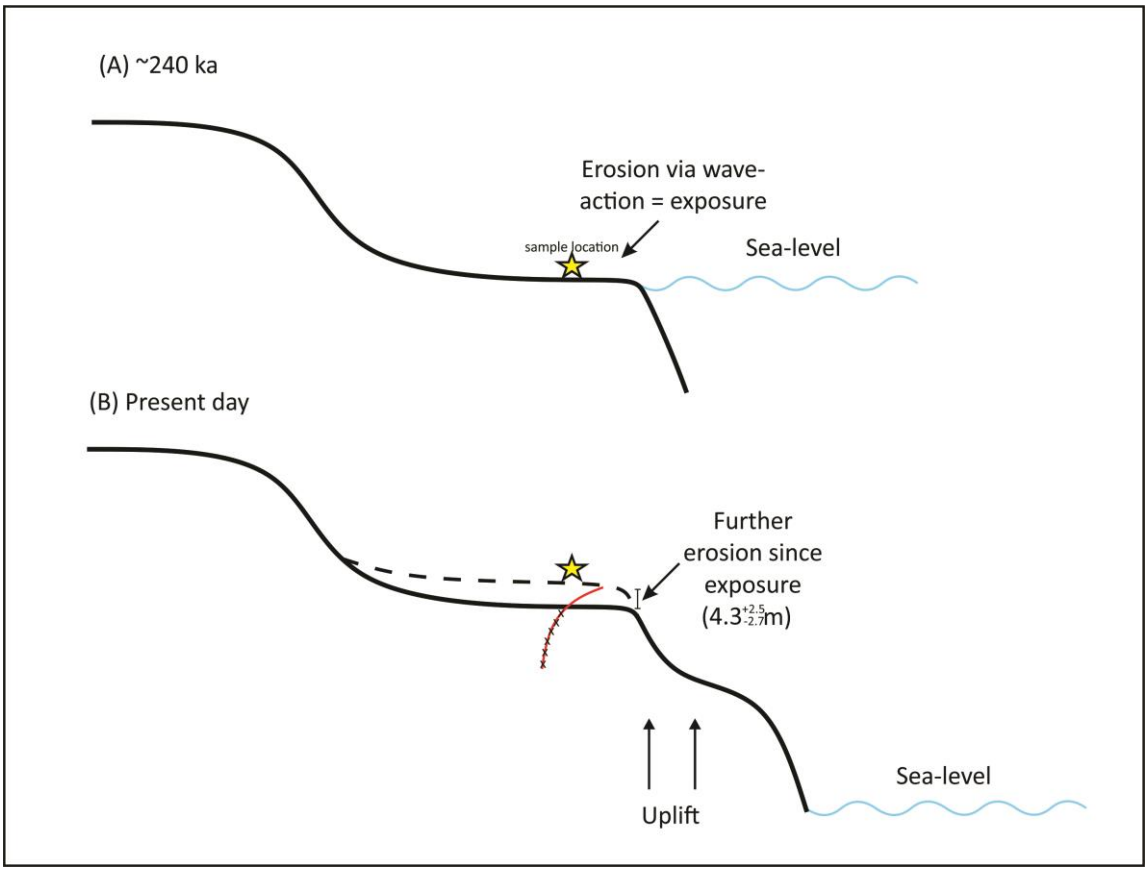

Figure 7.11 Schematic diagram illustrating a possible explanation for the exposure age result from the cosmogenic nuclide study. (A) shows the inferred sample location at 240 ka, exposed due to erosion via wave-action, and (B) displays present day sample location, after uplift and further erosion. The red exponential curve represents ^{10}Be concentration with depth. The "x"s on the red exponential curve represent the samples analysed during this study.

it is, and the larger amount of total erosion it has been subjected to (i.e. the higher segments should look less planar). Interestingly, this is certainly the case for Mt Kaukau.

We know that the sampled area was last eroded and exposed at the Earth's surface ~240 ka. The concentrations on some of the deeper samples (Figure 4.9) are so low, that the surface cannot be any older than the recorded age. Indeed, based on isotopic evidence, at least some of the K Surface remnants are not part of the previously suggested 4 or 0.4 Ma surface. That is not to say that other areas, such as Mount Kaukau are not. Further study is required to find out this information, and is touched on in the conclusions.

One aspect to note is the assumption of no inheritance when modelling K Surface age. In reality, the dated K Surface remnant could have been previously exposed, and therefore, technically there could be an issue of inheritance. However, if this were the case, then the

true exposure age would be even younger than 240 ka, which does not seem likely, as this would require an even higher uplift rate than already inferred.

Based on Wellington Fault total lateral offset (5 – 8 km) of the Mesozoic aged Esk Head Mélange (Begg and Mazengarb, 1996; Nicol et al., 2007) in the lower North Island and Quaternary lateral offset slip rates (~6 – 7.6 mm yr^{-1}) (Langridge et al., 2005; Little et al., 2010), the Wellington Fault has been active for approximately 1 Ma. This means that Wellington Fault activity was up and running well before the dated part of the K Surface was cut at ~240 ka. Considering that the total lateral offset on the Wellington Fault is up to 8 km, and based on the vertical to horizontal slip ratio for the active faults that cut through Wellington (10:1) (e.g. Heron et al., 1998; Langridge et al., 2005), the total accrued vertical slip on the Wellington Fault is up to 800 m. Further, if we assume constant slip rates since Wellington Fault initiation, the Wellington Fault would have slipped up to 6 km horizontally and up to 600 m vertically prior to K Surface exposure at ~240 ka. Because the Wellington Fault has been active for ~1 Ma, it seems sensible that we can assume a similar onset age for the Ohariu Fault. The active faults that cut through Wellington have different slip rates (e.g. Wellington 6 – 7.6 mm yr^{-1}, Ohariu ~1 – 2 mm yr^{-1}) (Heron et al., 1998; Langridge et al., 2005). We can see from the above discussion that, during the time of K Surface formation both the Wellington and Ohariu Faults were active and due to their differential slip rates, it seems unlikely that the K Surface was cut as one large marine platform.

At Makara Village, exposed on the scarp of the Ohariu Fault is a greywacke wave-cut platform overlain by Pliocene marine sediment (Grant-Taylor and Hornibrook, 1964). Due to the age of the overlying sediment, this wave-cut platform must be preserved from a previous uplift event, perhaps during the Late Miocene when the Wellington area was exposed to 4 km of exhumation (Kamp, 2000). In regards to the argument for one singular K Surface being cut at sea level, this geological evidence suggests otherwise.

Based on the discussion above, we can state with reasonable confidence that the K Surface was probably not cut as a singular, regional platform; rather the flat parts are more likely remnants of multiple marine platforms that have been cut and uplifted differentially. Figure

7.10 (A) and (B) demonstrates schematically how this alternative K Surface origin can result in the same morphology observed in the present-day landscape.

There remains however, an ambiguity for the mechanism(s), which have elevated western Wellington. Is this uplift due solely to differential movement on faults that cut through the region (Figure 7.10B), or is this faulting secondary to uplift due to flexure of the Pacific plate as it subducts, shown by the broad warping of the western Wellington hills? This question is now addressed in a regional context.

7.3.3 K Surface uplift mechanisms in a regional context

Regional vertical tectonic movements west of lower North Island are characterised by subsidence as evidenced by the southward migration of the Whanganui Basin depo-centre since the Pliocene (Figure 7.9) (e.g. Anderton, 1981; Hayward et al., 2010; Stern et al., 1992); this subsidence encroached the Marlborough Sounds at approximately 100 – 200 ka (Craw and Waters, 2007). The Wellington and Wairarapa regions on the other hand, have been subject to uplift since the Middle – Late Pliocene (Figure 1.6) (e.g. Lamb and Vella, 1987; Lee et al., 2002). Using geological evidence, Ghani (1978) described an increase in uplift rates (to 1.5 mm yr^{-1}) in the Wairarapa region at ~200 ka, corresponding to 300 m of broad net uplift (Figure 7.9) (Lamb and Vella, 1987). Due to a negative correlation between uplift pattern and inferred crustal and geodetic shortening rates, Lamb and Vella (1987) inferred that this late uplift was not fault controlled, nor due to underplating. Interestingly, the timing of initiation and rate of uplift for the Wairarapa broadly agrees with the exposure of the dated K Surface remnant ($238.1^{+149.3}_{-141.7}$ ka) and its associated uplift rate ($1.79\ ^{+0.59}_{-0.83}$) (Chapter 4).

Therefore, a suitable uplift mechanism for the K Surface must produce coeval subsidence and uplift at wavelengths of 70 – 80 km.

We present and test a simple geodynamic model of lithospheric plate flexure as an explanation for these coeval vertical movements of different sign (Figure 7.9) and hence, a mechanism for uplift of the K Surface. The method involves the modelling of a thin, semi-infinite elastic sheet with a free edge (representing the lithosphere) that overlies a weak,

inviscid substratum (that represents the asthenosphere). Specifically, we model the deflection of the thin, semi-infinite elastic plate with a free edge (a) subject to a line load, and (b) subject to a line load and horizontal in-plane stress (Figure 7.14) (e.g. Watts and Talwani, 1974). The methodology and constraints behind this modelling is recorded in Appendix 8. Figure 7.14 displays the results for the modelling and Figure 7.12 displays location and extent of the modelled area. The blue model represents normal subduction and the red model represents the addition of a barrier (Figure 7.14). The imposition of this barrier (represented in the model as a horizontal in-plane stress), results in a steepening trench and a more pronounced outer high. Note that the red model has the free edge of the plate flexing down to 4 km, which is consistent with total subsidence magnitude in the Whanganui Basin (Anderton, 1981). The average topographic profile, and thus, the broad wavelength of the K Surface is consistent with the wavelength produced by a flexed plate.

Horizontal in-plane stress is modelled as 2.5×10^{12} N m^{-1}, which is equivalent to a bending moment (Watts, 2001) of 5×10^{16} N, applied to the end of the plate. This value is consistent with the total ridge push of an old oceanic plate (Bott, 1993). We apply it in the situation where the freely subducting plate interacts with a barrier that effectively provides a net horizontal load on the end of the plate. This barrier is proposed to be the mantle lithosphere of the overriding Australian plate that rapidly thickened throughout the Pliocene – Pleistocene as evidenced by the southward migration of basin depo-centres of the western North Island (Stern et al., 2013). The addition of this barrier is postulated to have caused flexure of the Pacific Plate and subsequently, the broad uplift of the K Surface and the Wairarapa.

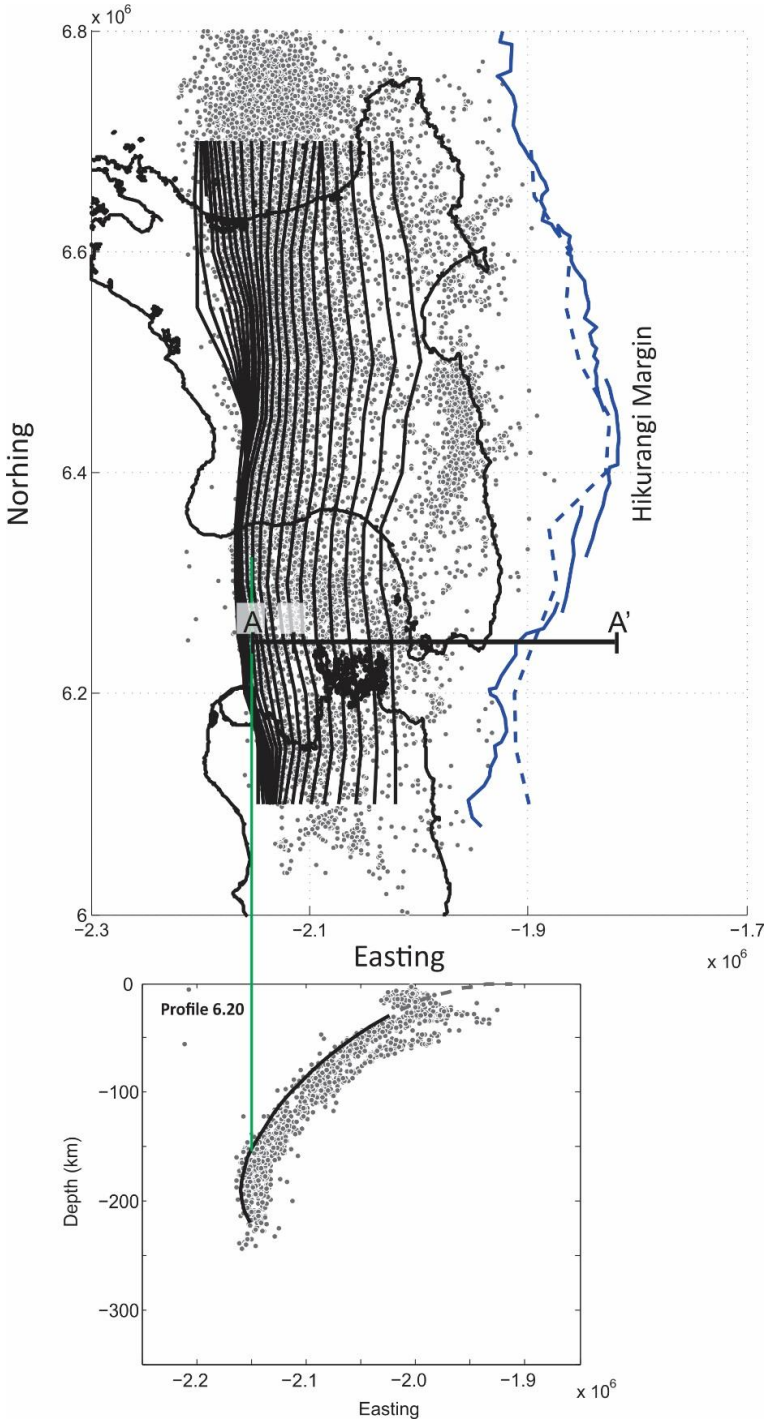

Figure 7.12 Regional figure (top) oriented to margin strike. A-A' pertains to the location of the geodynamic model (Figure 7.14). The cross-section below the top figure displays the plate interface at northing 6.2 X10^6, obtained from the last decade of micro-seismicity (from geonet catalogue). The green vertical line represents the inferred location of the free edge of the plate used for modelling. A is a plate edge 136 km away from western Wellington. Data from Euan Smith, personal communication 2016.

Because K Surface remnants were used as a main constraint for the flexural modelling, we assumed that the K Surface was formed as a regional erosion surface, subsequently deformed post formation. In subsection 7.3.2, however, we proposed that the "K Surface" composes of remnants of multiple time transgressive platforms, formed via differential uplift. Nevertheless, flexure as the principal uplift mechanism can still be reasoned. The overall "domed" characteristic of the K Surface (Figure 7.13) allows Mt Kaukau to emerge before our sample location near the west coast. This doming is overprinted by differential uplift and translocation due to faulting (Figure 7.14). This idea allows Mt Kaukau to be older, and thus would provide a more reasonable uplift rate. Furthermore, total erosion at our sample site since exposure is insignificant (~4 m over ~240 ka), meaning that modelling regional scale flexure is unaffected. This idea is portrayed schematically in Figure 7.13. Moreover, the idea that uplift is due to flexure of the oceanic lithosphere, as well as faulting, provides an explanation for the discrepancy in uplift rates between the MIS 5e terrace at Tongue Point (0.6 mm yr^{-1}) and for our sample location ($1.26\ ^{+1.85}_{-0.48}$ mm yr^{-1}), which we correlate to MIS 7.

Based on the above discussion, we propose that uplift of western Wellington is predominantly due to flexure of the Pacific Plate. Faulting plays a role in the time-transgressive formation of marine platforms; however, overall this movement is small and may be an effect of the ongoing flexure or some other large scale tectonic mechanism. Although Fault slip rates indicate faulting could be solely responsible for uplift, lack of reverse faults and a clear doming of topography that fits simple plate flexure models suggest otherwise. The spatial and temporal relationship between subsidence west of Wellington, and uplift in Wellington and Wairarapa with a broad wavelength of 70 – 80 km provide further evidence. A combination of flexure and faulting still allows the K Surface to be composed of multiple time transgressive marine platforms, due to the warped nature of the topography and the smaller scale crustal fault movements.

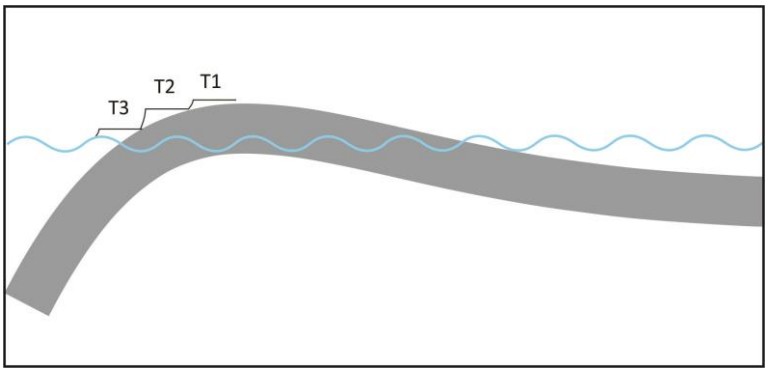

Figure 7.13 Schematic showing how doming due to flexure could result in the formation of multiple, time transgressive marine platforms.Mount Kaukau (T1) forms before our sample location on the west coast (T3).

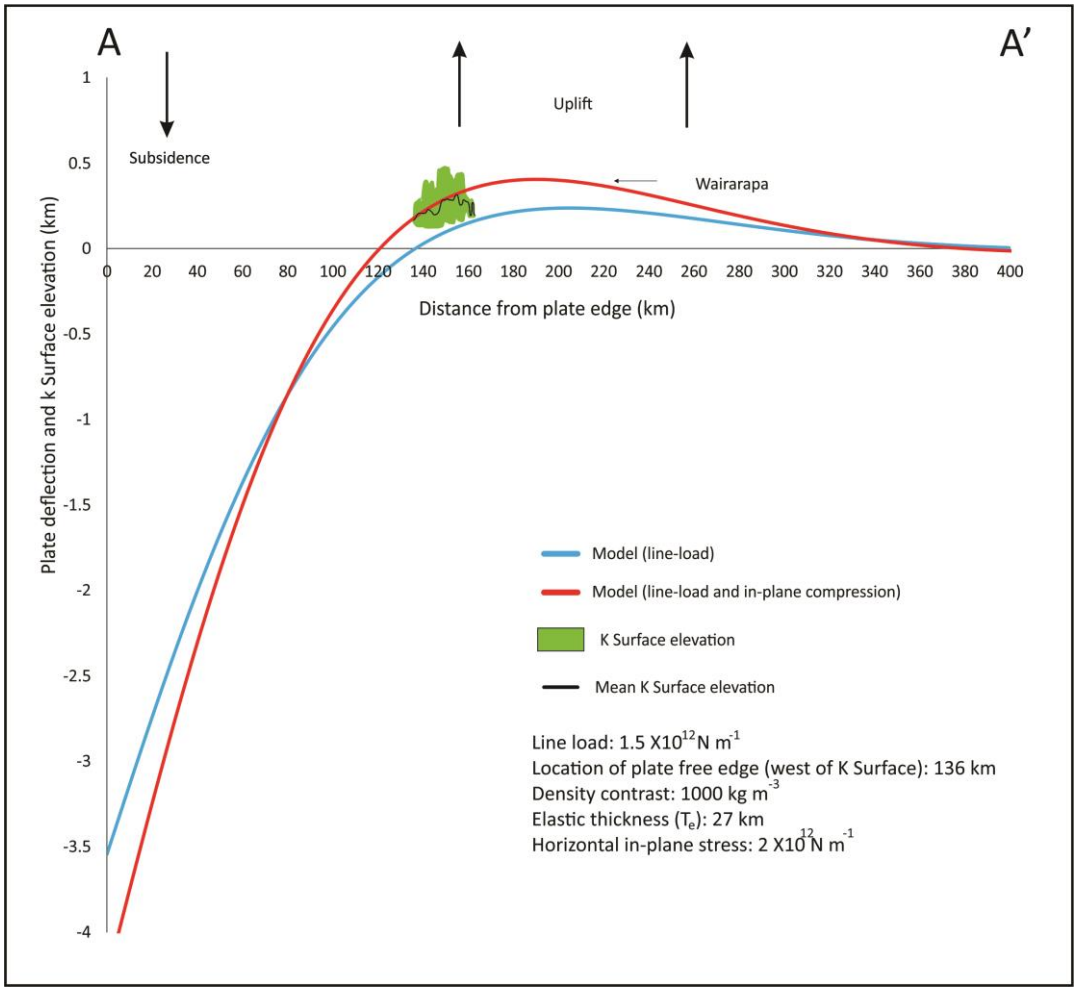

Figure 7.14 Simple models of flexure for the Pacific (oceanic) plate subduction at Wellington. The oceanic plate and underlying asthenosphere are modelled as an elastic solid overlying a weak fluid. Blue model = normal subduction, red model = addition of barrier. The green represents K Surface elevations with the upper and lower extents relating to maximum and minimum values, respectively. The black line is mean K Surface elevation. A-A' represents location of flexure profile displayed in Figure 7.12..

7.4 Synthesis

The key findings of this study are:

- The Pliocene marine outlier underlying Makara Village has a true thickness of > 170 m and dips to the SE. It is at its thickest extent in the south of the valley, thinning to the north before pinching out.
- Integration of P wave seismic velocities and porosity-relations in Pliocene mudstone/siltstone at Makara Village suggest that western Wellington has been subject to approximately 1700 ± 500 m of exhumation. This translates to 1900 ± 500 m rock uplift.
- Isotopic and geologic evidence suggests that the "K Surface" is not a singular regional erosion surface as previously thought; rather it is composed multiple time transgressive marine platforms that have been differentially uplifted due to a combination of flexure and faulting.
- Evidence for the timing of regional subsidence and uplift events in the lower North Island from this, and past studies, indicate that flexure of the Pacific plate is a viable driver for the uplift of the Wellington and Wairarapa regions since > 250 ka.
- Future research would involve acquiring more isotopic data from other hilltops, on different sides of the faults from around the region (e.g. Quartz Hill, Mt Kaukau, Mana Island). This would provide further constraints on "K Surface" age and formation.
- The flexural modelling completed in this thesis was first-order. More detailed modelling, e.g. using variable densities, would provide more accurate, in-depth results.

8 References

Allen, P. A., and Allen, J. R., 2013, Basin analysis: Principles and application to petroleum play assessment, John Wiley & Sons.

Anderson, R. S., Repka, J. L., and Dick, G. S., 1996, Explicit treatment of inheritance in dating depositional surfaces using in situ 10Be and 26Al: Geology, v. 24, no. 1, p. 47-51.

Anderton, P. W., 1981, Structure and evolution of the south Wanganui Basin, New Zealand: New Zealand journal of geology and geophysics, v. 24, no. 1, p. 39-63.

Armstrong, P. A., Allis, R. G., Funnell, R. H., and Chapman, D. S., 1998, Late Neogene exhumation patterns in Taranaki Basin (New Zealand): Evidence from offset porosity-depth trends: Journal of Geophysical Research, v. 103, no. B12, p. 30269.

Athy, L. F., 1930, Density, porosity, and compaction of sedimentary rocks: AAPG Bulletin, v. 14, no. 1, p. 1-24.

Balco, G., and Shuster, D. L., 2009, 26Al–10Be–21Ne burial dating: Earth and Planetary Science Letters, v. 286, no. 3-4, p. 570-575.

Balco, G., Stone, J. O., Lifton, N. A., and Dunai, T. J., 2008, A complete and easily accessible means of calculating surface exposure ages or erosion rates from 10 Be and 26 Al measurements: Quaternary geochronology, v. 3, no. 3, p. 174-195.

Barnes, P. M., and de Lépinay, B. M., 1997, Rates and mechanics of rapid frontal accretion along the very obliquely convergent southern Hikurangi margin, New Zealand: Journal of Geophysical Research: Solid Earth, v. 102, no. B11, p. 24931-24952.

Beanland, S., 1995, The North Island Dextral Fault Belt, Hikurangi Subduction Margin, New Zealand: A Thesis Submitted for the Degree of Doctor of Philosophy [in Geology], Victoria University of Wellington: Victoria University of Wellington.

Beavan, J., Tregoning, P., Bevis, M., Kato, T., and Meertens, C., 2002, Motion and rigidity of the Pacific Plate and implications for plate boundary deformation: Journal of Geophysical Research: Solid Earth, v. 107, no. B10.

Begg, J., Langridge, R., Van Dissen, R., and Little, T., Field Trip 1–Wellington Fault: neotectonics and earthquake geology of the Wellington-Hutt Valley segment. Geological Society of New Zealand Miscellaneous Publication 124B, *in* Proceedings Geosciences' 08-Geological Society of New Zealand, New Zealand Geophysical

Society, New Zealand Geochemical & Mineralogical Society joint annual conference field trip guide, 23 Nov2008, p. 5-67.

Begg, J. G., and Johnston, M. R. c., 2000, Geology of the Wellington Area, Lower Hutt, New Zealand, GNS, Institute of Geological & Nuclear Sciences 1:250000 geological map 10.

Begg, J. G., and Mazengarb, C., 1996, Geology of the Wellington area, scale 1:50 000, Lower Hutt, New Zealand., Institute of Geological and Nuclear Sciences, geological map 22.

Begg, J. G., Van Dissen, R. J., Rhoades, D., Lukovic, B., Heron, D., Darby, D., and Brown, L., 2003, Coseismic subsidence in the Lower Hutt valley resulting from rupture of the Wellington Fault. GNS Client Report 2003/140. Institute of Geological and Nuclear Sciences Ltd. EQC Research Report 2003/140.

Berryman, K. R., van Dissen, R., and Mouslopoulou, V., 2002, Recent rupture of the Tararua section of the Wellington Fault and relationships to other faults section and rupture segments: GNS Science.

Blard, P.-H., Bourles, D., Pik, R., and Lavé, J., 2008, In situ cosmogenic 10 Be in olivines and pyroxenes: Quaternary Geochronology, v. 3, no. 3, p. 196-205.

Bolt, B. A., 1982, Inside the earth: evidence from earthquakes, San Francisco, Freeman.

Bott, M., 1993, Modelling the plate-driving mechanism: Journal of the Geological Society, v. 150, no. 5, p. 941-951.

Bradshaw, J., Andrews, P., and Adams, C., 1981, Carboniferous to Cretaceous on the Pacific margin of Gondwana: the Rangitata phase of New Zealand: Gondwana five, p. 217-221.

Cande, S. C., and Stock, J. M., 2004, Pacific—Antarctic—Australia motion and the formation of the Macquarie Plate: Geophysical Journal International, v. 157, no. 1, p. 399-414.

Cerling, T., and Craig, H., 1994, Geomorphology and in-situ cosmogenic isotopes: Annual Review of Earth and Planetary Sciences, v. 22, p. 273-317.

Chmeleff, J., von Blanckenburg, F., Kossert, K., and Jakob, D., 2010, Determination of the 10 Be half-life by multicollector ICP-MS and liquid scintillation counting: Nuclear Instruments and Methods in Physics Research Section B: Beam Interactions with Materials and Atoms, v. 268, no. 2, p. 192-199.

Chorley, R. J., Beckinsale, R. P., and Dunn, A. J., 1973, The History of the Study of Landforms Or The Development of Geomorphology: The Life and Work of William Morris Davis, Psychology Press.

Christensen, N. I., and Okaya, D. A., 2007, Compressional and shear wave velocities in South Island, New Zealand rocks and their application to the interpretation of seismological models of the New Zealand crust: A Continental Plate Boundary: Tectonics at South Island, New Zealand, p. 123-155.

Cotton, C. A., 1912a, Recent and sub-recent movements of uplift and of subsidence near Wellington, New Zealand: The Scottish Geographical Magazine, v. 28, no. 6, p. 306-312.

Cotton, C. A., 1912b, Notes on Wellington Physiography: Transactions of the New Zealand Institute, v. 44, p. 245-265.

Cotton, C. A., 1953, Tectonic Relief Features in and Around Wellington.

Cotton, C. A., 1957, Tectonic Features in a Coastal Setting at Wellington: Transactions of the Royal Society of New Zealand, v. 84, no. Part 4, p. 761-790.

Craw, D., and Waters, J., 2007, Geological and biological evidence for regional drainage reversal during lateral tectonic transport, Marlborough, New Zealand: Journal of the Geological Society, v. 164, no. 4, p. 785-793.

Darvill, C. M., 2013, Cosmogenic nuclide analysis: British Society for Geomorphology, p. 1-25.

Davey, F., and Stern, T., 1990, Crystal Seismic observations across the convergent plate boundary, North Island, New Zealand: Tectonophysics, v. 173, no. 1, p. 283-296.

Davy, R., 2012, Glaciotectonic processes associated with the central Alpine Fault: a gravity study of the central West Coast, South Island, New Zealand [Unpublished Masters thesis: Victoria University of Wellington.

Dorsch, J., and Katsube, T. J., 1999, Porosity characteristics of Cambrian mudrocks (Oak Ridge, East Tennessee, USA) and their implications for contaminant transport: Geological Society, London, Special Publications, v. 158, no. 1, p. 157-173.

Dunai, T. J., 2010, Cosmogenic Nuclides: Principles, Concepts and Applications in the Earth Surface Sciences, University of Edinburgh, Cambridge University Press.

England, P., and Molnar, P., 1990, Surface uplift, uplift of rocks, and exhumation of rocks: Geology, v. 18, no. 12, p. 1173-1177.

Ferguson, S., Hochstein, M., and Kibblewhite, A., 1980, Seismic refraction studies in the northern Hauraki Gulf, New Zealand: New Zealand journal of geology and geophysics, v. 23, no. 1, p. 17-25.

Garrick, R., Hatherton, T., and Waiters, W., 1973, Seismic Velocity Studies in the Southern Alps, New Zealand: Petrographic Notes on Thin Sections: New Zealand journal of geology and geophysics, v. 16, no. 4, p. 973-995.

Gerkens, J. C. A., 1989, Foundation of exploration geophysics, Amsterdam, Elsevier Science Publishers B.V.

Ghani, M., 1978, Late Cenozoic vertical crustal movements in the southern North Island, New Zealand: New Zealand journal of geology and geophysics, v. 21, no. 1, p. 117-125.

Giles, M. R., 1997, Diagenesis: A quantitative perspective: Implications for basin modelling and rock property prediction, Kluwer Academic Pub.

Gosse, J. C., and Phillips, F. M., 2001, Terrestrial in situ cosmogenic nuclides: theory and application: Quaternary Science Reviews, v. 20, no. 14, p. 1475-1560.

Grant-Taylor, T. L., 1965, Geology of Wellington: A Tour Guide: New Zealand Geological Survey Handbook, New Zealand Department of Scientific and Industrial Research.

Grant-Taylor, T. L., 1967, Fault movements and deformation on the Wellington Fault in the Wellington region, New Zealand Geological Survey.

Grant-Taylor, T. L., and Hornibrook, N. d. B., 1964, The Makara faulted outlier and the age of Cook Strait: New Zealand Journal of Geology and Geophysics, v. 7, no. 2, p. 299-311.

Grant, F. S., and West, G. F., 1965, Interpretation theory in applied geophysics, McGraw-Hill Book.

Grapes, R. H., 2008, Sir Charles Cotton (1885-1970); international geomorphologist: History of geomorphology and Quaternary geology, v. Geological Society Special Publications, no. 301, p. 295-313.

Gross, R., Green, A. G., Horstmeyer, H., and Begg, J. H., 2004, Location and geometry of the Wellington fault (New Zealand) defined by detailed three-dimensional georadar data: Journal of Geophysical Research: Solid Earth (1978–2012), v. 109, no. B5.

Hagedoorn, J., 1959, The Plus-Minus Method of Interpreting Seismic Refraction Sections: Geophysical prospecting, v. 7, no. 2, p. 158-182.

Hamilton, E. L., 1979, Vp/Vs and Poisson's ratios in marine sediments and rocks: The Journal of the Acoustical Society of America, v. 66, no. 4, p. 1093-1101.

Hatherton, T., and Leopard, A., 1964, The densities of New Zealand rocks: New Zealand journal of geology and geophysics, v. 7, no. 3, p. 605-625.

Hayward, B. W., Grenfell, H. R., Sabaa, A. T., Kay, J., Daymond-King, R., and Cochran, U., 2010, Holocene subsidence at the transition between strike-slip and subduction on the Pacific-Australian plate boundary, Marlborough Sounds, New Zealand: Quaternary Science Reviews, v. 29, no. 5, p. 648-661.

Heisinger, B., Lal, D., Jull, A., Kubik, P., Ivy-Ochs, S., Knie, K., and Nolte, E., 2002a, Production of selected cosmogenic radionuclides by muons: 2. Capture of negative muons: Earth and Planetary Science Letters, v. 200, no. 3, p. 357-369.

Heisinger, B., Lal, D., Jull, A., Kubik, P., Ivy-Ochs, S., Neumaier, S., Knie, K., Lazarev, V., and Nolte, E., 2002b, Production of selected cosmogenic radionuclides by muons: 1. Fast muons: Earth and Planetary Science Letters, v. 200, no. 3, p. 345-355.

Henrys, S., Wech, A., Sutherland, R., Stern, T., Savage, M., Sato, H., Mochizuki, K., Iwasaki, T., Okaya, D., and Seward, A., 2013, SAHKE geophysical transect reveals crustal and subduction zone structure at the southern Hikurangi margin, New Zealand: Geochemistry, Geophysics, Geosystems, v. 14, no. 7, p. 2063-2083.

Heron, D., van Dissen, R., and Sawa, M., 1998, Late Quaternary movement on the Ohariu Fault, Tongue Point to MacKays Crossing, North Island, New Zealand: New Zealand Journal of Geology and Geophysics, v. 41, no. 4, p. 419-439.

Hicks, S., and Woodward, D., 1978, Gravity models of the Wairarapa region, New Zealand: New Zealand journal of geology and geophysics, v. 21, no. 5, p. 539-544.

Hidy, A. J., Gosse, J. C., Pederson, J. L., Mattern, J. P., and Finkel, R. C., 2010, A geologically constrained Monte Carlo approach to modeling exposure ages from profiles of

cosmogenic nuclides: An example from Lees Ferry, Arizona: Geochemistry, Geophysics, Geosystems, v. 11, no. 9.

Hinze, W. J., 2003, Bouguer reduction density, why 2.67?: Geophysics, v. 68, no. 5, p. 1559-1560.

Hinze, W. J., Carlos Aiken, John Brozena, Bernard Coakley, David Dater, Guy Flanagan, Rene Forsberg, Thomas Hildenbrand, G. Randy Keller, James Kellogg, Robert Kucks, Xiong Li, Andre Mainville, Robert Morin, Mark Pilkington, Donald Plouff, Dhananjay Ravat, Daniel Roman, Jamie Urrutia-Fucugauchi, Marc Veronneau, Webring, M., and Winester, D., 2005, New standards for reducing gravity data; the North American gravity database: Geophysics, v. 70, no. 4, p. J25-J32.

Hochstein, M., and Davey, F. J., 1974, Seismic measurements in Wellington harbour: Journal of the Royal Society of New Zealand, v. 4, no. 2, p. 123-140.

Hochstein, M., and Hunt, T., 1970, Seismic, gravity and magnetic studies, Broadlands geothermal field, New Zealand: Geothermics, v. 2, p. 333-346.

Houseman, G. A., and Molnar, P., 1997, Gravitational (Rayleigh–Taylor) instability of a layer with non-linear viscosity and convective thinning of continental lithosphere: Geophysical Journal International, v. 128, no. 1, p. 125-150.

Hunt, T. M., 1969, Gravity survey of the lower Awatere district, Marlborough, New Zealand: New Zealand journal of geology and geophysics, v. 12, no. 4, p. 633-642.

Hunt, T. M., 1980, Basement structure of the Wanganui Basin, onshore, interpreted from gravity data: New Zealand journal of geology and geophysics, v. 23, no. 1, p. 1-16.

Jiao, R., 2015, Thermo-tectonic studies of Mesozoic basement rocks, North Island, New Zealand [Unpublished PhD thesis: Victoria University of Wellington.

Jiao, R., Seward, D., Little, T. A., and Kohn, B. P., 2015, Unroofing of fore-arc ranges along the Hikurangi Margin, New Zealand: Constraints from low-temperature thermochronology: Tectonophysics, v. 656, p. 39-51.

Johnston, M. R., 1980, Geology of the Tinui-Awatoitoi district, New Zealand Department of Scientific and Industrial Research.

Kamp, P. J. J., 2000, Thermochronology of the Torlesse accretionary complex, Wellington region, New Zealand: Journal of Geophysical Research, v. 105, no. B8, p. 19253.

Kearey, P., Brooks, M., and Hill, I., 2002, An Introduction to Geophysical Exploration, Wiley.

King, P. R., 2000, Tectonic reconstructions of New Zealand: 40 Ma to the present: New Zealand Journal of Geology and Geophysics, v. 43, no. 4, p. 611-638.

Kohl, C., and Nishiizumi, K., 1992, Chemical isolation of quartz for measurement of in-situ-produced cosmogenic nuclides: Geochimica et Cosmochimica Acta, v. 56, no. 9, p. 3583-3587.

Korschinek, G., Bergmaier, A., Faestermann, T., Gerstmann, U. C., Knie, K., Rugel, G., Wallner, A., Dillmann, I., Dollinger, G., von Gostomski, C. L., Kossert, K., Maiti, M., Poutivtsev, M., and Remmert, A., 2010, A new value for the half-life of 10Be by Heavy-Ion Elastic Recoil Detection and liquid scintillation counting: Nuclear Instruments and Methods in Physics Research Section B: Beam Interactions with Materials and Atoms, v. 268, no. 2, p. 187-191.

Lal, D., 1991, Cosmic ray labeling of erosion surfaces: in situ nuclide production rates and erosion models: Earth and Planetary Science Letters, v. 104, no. 2, p. 424-439.

Lamarche, G., Proust, J. N., and Nodder, S. D., 2005, Long-term slip rates and fault interactions under low contractional strain, Wanganui Basin, New Zealand: Tectonics, v. 24, no. 4.

Lamb, S., 2011, Cenozoic tectonic evolution of the New Zealand plate-boundary zone: A paleomagnetic perspective: Tectonophysics, v. 509, no. 3, p. 135-164.

Lamb, S., and Bibby, H., 1989, The last 25 Ma of rotational deformation in part of the New Zealand plate-boundary zone: Journal of structural geology, v. 11, no. 4, p. 473-492.

Lamb, S., and Vella, P., 1987, The last million years of deformation in part of the New Zealand plate-boundary zone: Journal of structural geology, v. 9, no. 7, p. 877-891.

Landis, C. A., Campbell, H. J., Begg, J. G., Mildenhall, D. C., Paterson, A. M., and Trewick, S. A., 2008, The Waipounamu Erosion Surface: questioning the antiquity of the New Zealand land surface and terrestrial fauna and flora: Geological Magazine, v. 145, no. 02.

Langridge, R., Berryman, K., and Van Dissen, R., 2005, Defining the geometric segmentation and Holocene slip rate of the Wellington Fault, New Zealand: the Pahiatua section: New Zealand Journal of Geology and Geophysics, v. 48, no. 4, p. 591-607.

Lay, T., and Wallace, T. C., 1995, Modern global seismology, Academic press.

Lee, J. M., Begg, J., and Forsyth, P., 2002, Geology of the Wairarapa area, Institute of Geological & Nuclear Sciences.

Lisiecki, L. E., and Raymo, M. E., 2005, A Pliocene-Pleistocene stack of 57 globally distributed benthic δ18O records: Paleoceanography, v. 20, no. 1.

Litchfield, N., van Dissen, R., Hemphill-Haley, M., Townsend, D., and Heron, D., 2010, Post c. 300 year rupture of the Ohariu fault in Ohariu Valley, New Zealand: New Zealand Journal of Geology and Geophysics, v. 53, no. 1, p. 43-56.

Litchfield, N., Van Dissen, R., Sutherland, R., Barnes, P., Cox, S., Norris, R., Beavan, R., Langridge, R., Villamor, P., and Berryman, K., 2014, A model of active faulting in New Zealand: New Zealand Journal of Geology and Geophysics, v. 57, no. 1, p. 32-56.

Little, T., Van Dissen, R., Schermer, E., and Carne, R., 2009, Late Holocene surface ruptures on the southern Wairarapa fault, New Zealand: Link between earthquakes and the uplifting of beach ridges on a rocky coast: Lithosphere, v. 1, no. 1, p. 4-28.

Little, T. A., Van Dissen, R., Rieser, U., Smith, E. G., and Langridge, R. M., 2010, Coseismic strike slip at a point during the last four earthquakes on the Wellington fault near Wellington, New Zealand: Journal of Geophysical Research: Solid Earth, v. 115, no. B5.

Málek, J., Janský, J., Novotný, O., and Rössler, D., 2004, Vertically inhomogeneous models of the upper crustal structure in the West-Bohemian seismoactive region inferred from the CELEBRATION 2000 refraction data: Studia Geophysica et Geodaetica, v. 48, no. 4, p. 709-730.

Masarik, J., and Beer, J., 1999, Simulation of particle fluxes and cosmogenic nuclide production in the Earth's atmosphere: Journal of Geophysical Research, v. 104, no. D10, p. 12,099-112.

Masarik, J., and Reedy, R. C., 1995, Terrestrial cosmogenic-nuclide production systematics calculated from numerical simulations: Earth and Planetary Science Letters, v. 136, no. 3, p. 381-395.

McCubbine, J., Stagpoole, V. M., Smith, E. G. C., and Tontini, F., 2014, G-solve, A computer program to reduce relative gravity measurements to absolute gravity values: GNS Science.

McKay, A., 1877, Report on the Tertiary rocks at Makara: New Zealand Geological Survey Report of Geological Explorations 1874, v. 6, no. 9, p. 54.

Michel, R., Leya, I., and Borges, L., 1996, Production of cosmogenic nuclides in meteoroids: accelerator experiments and model calculations to decipher the cosmic ray record in extraterrestrial matter: Nuclear Instruments and Methods in Physics Research Section B: Beam Interactions with Materials and Atoms, v. 113, no. 1, p. 434-444.

Mildenhall, D. C., and Alloway, B. V. 2008, A widespread ca. 1.1 Ma TVZ silicic tephra preserved near Wellington, New Zealand: implications for regional reconstruction of mid-Pleistocene vegetation. Quaternary International, 178(1), 167-182.

Milsom, J., 2000, The Geological Field Guide Series, Baffins Lane, Chichester, West Sussex PO19 1UD, England, Wiley, Field Geophysics

Moritz, H., 1980, Geodetic reference system 1980: Journal of Geodesy, v. 54, no. 3, p. 395-405.

Mortimer, N., 1994, Origin of the Torlesse terrane and coeval rocks, North Island, New Zealand: International geology review, v. 36, no. 10, p. 891-910.

Nettleton, L. L., 1976, Gravity and magnetics in oil prospecting, New York, McGraw-Hill.

Nicol, A., and Campbell, J. K., 1990, Late Cenozoic thrust tectonics, Picton, New Zealand: New Zealand Journal of Geology and Geophysics, v. 33, no. 3, p. 485-494.

Nicol, A., Mazengarb, C., Chanier, F., Rait, G., Uruski, C., and Wallace, L., 2007, Tectonic evolution of the active Hikurangi subduction margin, New Zealand, since the Oligocene: Tectonics, v. 26, no. 4, p. TC4002.

Nishiizumi, K., Imamura, M., Caffee, M. W., Southon, J. R., Finkel, R. C., and McAninch, J., 2007, Absolute calibration of 10 Be AMS standards: Nuclear Instruments and Methods in Physics Research Section B: Beam Interactions with Materials and Atoms, v. 258, no. 2, p. 403-413.

Norton, K. P., von Blanckenburg, F., Schlunegger, F., Schwab, M., and Kubik, P. W., 2008, Cosmogenic nuclide-based investigation of spatial erosion and hillslope channel coupling in the transient foreland of the Swiss Alps: Geomorphology, v. 95, no. 3, p. 474-486.

Novotný, O., Janský, J., and Málek, J., 2004, Some aspects of the application of the Wiechert-Herglotz method to refraction data from Western Bohemia: Acta Geodyn. Geomater, v. 1, no. 2, p. 134.

Nowack, R. L., 1990, Tomography and the Herglotz-Wiechert inverse formulation: pure and applied geophysics, v. 133, no. 2, p. 305-315.

Ota, Y., Williams, D. N., and Berryman, K. R., 1981, Parts sheets Q27, R27 & R28 - Wellington (1st ed). Late Quaternary tectonic map of New Zealand with notes: Department of Scientific and Industrial Research, scale 1:50 000.

Pillans, B., Kohn, B. P., Berger, G., Froggatt, P., Duller, G., Alloway, B., & Hesse, P. 1996, Multi-method dating comparison for mid-Pleistocene Rangitawa tephra, New Zealand. Quaternary Science Reviews, 15(7), 641-653.

Proust, J.-N., Lamarche, G., Nodder, S., and Kamp, P. J., 2005, Sedimentary architecture of a Plio-Pleistocene proto-back-arc basin: Wanganui Basin, New Zealand: Sedimentary Geology, v. 181, no. 3, p. 107-145.

Pulford, A., 2002, Crustal Structure and Lithospheric Doming: Aspects of Deformation Along an Obliquely Convergent Plate Margin, New Zealand [Unpublished PhD thesis: Victoria University of Wellington.

Pulford, A., and Stern, T., 2004, Pliocene exhumation and landscape evolution of central North Island, New Zealand: the role of the upper mantle: Journal of Geophysical Research: Earth Surface, v. 109, no. F1.

Putnam, A. E., Schaefer, J. M., Barrell, D. J. A., Vandergoes, M., Denton, G. H., Kaplan, M. R., Finkel, R. C., Schwartz, R., Goehring, B. M., and Kelley, S. E., 2010, In situ cosmogenic 10Be production-rate calibration from the Southern Alps, New Zealand: Quaternary Geochronology, v. 5, no. 4, p. 392-409.

Rait, G., Chanier, F., and Waters, D. W., 1991, Landward-and seaward-directed thrusting accompanying the onset of subduction beneath New Zealand: Geology, v. 19, no. 3, p. 230-233.

Reay, M., Heron, D., and Francis, D., 1988, Printers Flat Drilling Project: The Geophysics Division, part of the Department of Scientific and Industrial Research.

Reyners, M., 2013, The central role of the Hikurangi Plateau in the Cenozoic tectonics of New Zealand and the Southwest Pacific: Earth and Planetary Science Letters, v. 361, p. 460-468.

Reyners, M., Eberhart-Phillips, D., and Bannister, S., 2011, Tracking repeated subduction of the Hikurangi Plateau beneath New Zealand: Earth and Planetary Science Letters, v. 311, no. 1, p. 165-171.

Salmon, M., Stern, T., and Savage, M. K., 2011, A major step in the continental Moho and its geodynamic consequences: the Taranaki-Ruapehu line, New Zealand: Geophysical Journal International, v. 186, no. 1, p. 32-44.

Schellart, W., Lister, G., and Toy, V., 2006, A Late Cretaceous and Cenozoic reconstruction of the Southwest Pacific region: tectonics controlled by subduction and slab rollback processes: Earth-Science Reviews, v. 76, no. 3, p. 191-233.

Schermer, E. R., Little, T. A., and Rieser, U., 2009, Quaternary deformation along the Wharekauhau fault system, North Island, New Zealand: Implications for an unstable linkage between active strike-slip and thrust faults: Tectonics, v. 28, no. 6.

Sissons, B., and Dibble, R., 1981, A seismic refraction experiment southeast of Ruapehu volcano: New Zealand journal of geology and geophysics, v. 24, no. 1, p. 31-38.

Smith, E. G., 1981, Calculation of poles of instantaneous rotation from poles of finite rotation: Geophysical Journal International, v. 65, no. 1, p. 223-227.

Stagpoole, V. M., 1997, A Geophysical Study of the Northern Taranaki Basin, New Zealand: A Thesis Submitted [to] Victoria University of Wellington for the Degree of Doctor of Philosophy [in Geology]: Victoria University of Wellington.

Stern, T., 1985, A back-arc basin formed within continental lithosphere: the Central Volcanic Region of New Zealand: Tectonophysics, v. 112, no. 1, p. 385-409.

Stern, T., Houseman, G., Salmon, M., and Evans, L., 2013, Instability of a lithospheric step beneath western North Island, New Zealand: Geology, v. 41, no. 4, p. 423-426.

Stern, T., Quinlan, G., and Holt, W., 1992, Basin formation behind an active subduction zone: three-dimensional flexural modelling of Wanganui Basin, New Zealand: Basin research, v. 4, no. 3-4, p. 197-214.

Stern, T., Stratford, W., and Salmon, M., 2006, Subduction evolution and mantle dynamics at a continental margin: Central North Island, New Zealand: Reviews of Geophysics, v. 44, no. 4.

Stern, T., Stratford, W., Seward, A., Henderson, M., Savage, M., Smith, E., Benson, A., Greve, S., and Salmon, M., 2010, Crust–mantle structure of the central North Island, New Zealand, based on seismological observations: Journal of Volcanology and Geothermal Research, v. 190, no. 1, p. 58-74.

Stevens, G. R., New Zealand Consolidated Press, W., and Printing, K., 1974, Rugged landscape: the geology of central New Zealand, incl. Wellington, Wairarapa, Manawatu and the Marlbrough Sounds, AH & AW Reed.

Stock, J., and Molnar, P., 1982, Uncertainties in the relative positions of the Australia, Antarctica, Lord Howe, and Pacific plates since the Late Cretaceous: Journal of Geophysical Research: Solid Earth, v. 87, no. B6, p. 4697-4714.

Stone, J. O., 2000, Air pressure and cosmogenic isotope production: Journal of Geophysical Research: Solid Earth (1978–2012), v. 105, no. B10, p. 23753-23759.

Stratford, W., and Stern, T., 2006, Crust and upper mantle structure of a continental backarc: central North Island, New Zealand: Geophysical Journal International, v. 166, no. 1, p. 469-484.

Sutherland, R., 1995, The Australia-Pacific boundary and Cenozoic plate motions in the SW Pacific: Some constraints from Geosat data: Tectonics, v. 14, no. 4, p. 819-831.

Sutherland, R., Davey, F., and Beavan, J., 2000, Plate boundary deformation in South Island, New Zealand, is related to inherited lithospheric structure: Earth and Planetary Science Letters, v. 177, no. 3, p. 141-151.

Te Punga, M. T. 1984a, A note on the Kaitoke Gravel Formation. New Zealand Geological Survey, Department of Scientific and Industrial Research.

Te Punga, M. T. 1984b, Age, Distribution and Clay Mineralogy of the Mangaroa Ash Wellington. New Zealand Geological Survey, Department of Scientific and Industrial Research.

Telford, W. M., Geldart, L. P., and Sheriff, R. E., 1990, Applied Geophysics: Cambridge University Press, Cambridge, Second edition.

Tozer, B., 2013, Crustal Structure of Wanganui Basin: Implications for Back-Arc Basin Formation [Unpublished MSc Thesis: Victoria University of Wellington.

Van Dissen, R. J., and Berryman, K. R., 1996, Surface rupture earthquakes over the last∼ 1000 years in the Wellington region, New Zealand, and implications for ground shaking hazard: Journal of Geophysical Research: Solid Earth (1978–2012), v. 101, no. B3, p. 5999-6019.

Vassil'ev, Y., and Gurevich, G., 1962, On the ratio between attenuation decrements and propagation velocities of longitudinal and transverse waves; English translation: Bull, Acad. Sci., USSR, Geophys. Ser, no. 12, p. 1061-1074.

Walcott, R. I., 1978, Geodetic strains and large earthquakes in the axial tectonic belt of North Island, New Zealand: Journal of Geophysical Research: Solid Earth, v. 83, no. B9, p. 4419-4429.

Walcott, R. I., 1984a, The kinematics of the plate boundary zone through New Zealand: a comparison of short- and long-term deformations: Geophysical Journal International, v. 79, no. 2, p. 613-633.

Walcott, R. I., 1984b, Reconstructions for the New Zealand Region for the Neogene: Paleogeography, Paleoclimatology, Paleoecology, v. 46, p. 217-231.

Walcott, R. I., 1987, Geodetic strain and the deformational history of the North Island of New Zealand during the late Cainozoic: Philosophical Transactions of the Royal Society of London A: Mathematical, Physical and Engineering Sciences, v. 321, no. 1557, p. 163-181.

Walcott, R. I., 1998, Modes of oblique compression: Late Cenozoic tectonics of the South Island of New Zealand: Reviews of geophysics, v. 36, no. 1, p. 1-26.

Wallace, L., Barnes, P., Beavan, J., Van Dissen, R., Litchfield, N., Mountjoy, J., Langridge, R., Lamarche, G., and Pondard, N., 2012, The kinematics of a transition from subduction to strike-slip: An example from the central New Zealand plate boundary: Journal of Geophysical Research: Solid Earth (1978–2012), v. 117, no. B2.

Wallace, L. M., Beavan, J., McCaffrey, R., and Darby, D., 2004, Subduction zone coupling and tectonic block rotations in the North Island, New Zealand: Journal of Geophysical Research: Solid Earth, v. 109, no. B12, p. n/a-n/a.

Watson, C. D. S., and Norton, K. P., Following in Cotton's footsteps (tire tracks): Origin and evolution of the Wellington K Surface by mountain bike, *in* Proceedings New Zealand GeoSciences 2015, Wellington, 2015, Field Trip Guides.

Watts, A. B. 2001, Isostasy and Flexure of the Lithosphere. Cambridge University Press.

Watts, A. B., and Talwani, M., 1974, Gravity anomalies seaward of deep-sea trenches and their tectonic implications: Geophysical Journal International, v. 36, no. 1, p. 57-90.

Weissel, J. K., Hayes, D. E., and Herron, E. M., 1977, Plate tectonics synthesis: the displacements between Australia, New Zealand, and Antarctica since the Late Cretaceous: Marine geology, v. 25, no. 1, p. 231-277.

Wells, P., 1989, Burial history of late Neogene sedimentary basins on part of the New Zealand convergent plate margin: Basin research, v. 2, no. 3, p. 145-160.

Willenbring, J. K., and von Blanckenburg, F., 2010, Long-term stability of global erosion rates and weathering during late-Cenozoic cooling: Nature, v. 465, no. 7295, p. 211-214.

Wilson, C. K., Jones, C. H., Molnar, P., Sheehan, A. F., and Boyd, O. S., 2004, Distributed deformation in the lower crust and upper mantle beneath a continental strike-slip fault zone: Marlborough fault system, South Island, New Zealand: Geology, v. 32, no. 10, p. 837-840.

Wright, I., 1993, Pre-spread rifting and heterogeneous volcanism in the southern Havre Trough back-arc basin: Marine geology, v. 113, no. 3, p. 179-200.

Wright, I. C., 1994, Nature and tectonic setting of the southern Kermadec submarine arc volcanoes: An overview: Marine Geology, v. 118, no. 3, p. 217-236.

9 Appendices

All appendices are loaded on the CD located at the back page of the thesis. Titles of appendices are listed below:

- Appendix 1: Gravity reductions
- Appendix 2: Seismic survey geometry
- Appendix 3: WHB integral
- Appendix 4: Seismic shot gathers
- Appendix 5: Quartz preparation and separation of cosmogenic Be
- Appendix 6: K Surface topographic analysis process diagram
- Appendix 7: K Surface interpolation cross-validation tables
- Appendix 8: Flexure methodology